Origin of IceCube's Astrophysical Neutrinos: Autocorrelation, Multi-Point-Source and Time-Structured Searches

Dissertation

Anna Bernhard

Technische Universität München
Physik-Department
Experimental Physics with Cosmic Particles

Origin of IceCube's Astrophysical Neutrinos: Autocorrelation, Multi-Point-Source and Time-Structured Searches

Anna Bernhard

Vollständiger Abdruck der von der Fakultät für Physik der Technischen Universität München zur Erlangung des akademischen Grades eines

Doktors der Naturwissenschaften (Dr. rer. nat.)

genehmigten Dissertation.

Vorsitzender:	Univ.-Prof. Dr. Björn Garbrecht
Prüfer der Dissertation:	1. Univ.-Prof. Dr. Elisa Resconi
	2. Univ.-Prof. Dr. Lothar Oberauer

Die Dissertation wurde am 02.12.2014 bei der Technischen Universität München eingereicht und durch die Fakultät für Physik am 22.01.2015 angenommen.

Abstract

The IceCube neutrino observatory build in the Antarctic ice offers unique opportunities in studying high energy neutrino emission from galactic and extragalactic sources. Detecting such neutrino emission could give invaluable information about the origin of cosmic rays. In 2013, the first positive detection of astrophysical neutrinos in the PeV range was found with IceCube. The origin of these neutrinos is not yet clear, but advanced analysis methods are being developed in order to improve the sensitivity to point sources. An energy-dependent likelihood scan was performed on IceCube data. A complementary way to get insight into the cosmic ray production is the study of an event clustering at small scales for high-energy neutrinos.

In this work three analyses for such a small-scale clustering of neutrino events are presented. They are all based on a two-point correlation function and target a different scenario in searching not only for one strong point source, but several weaker sources, which can not be detected by the baseline likelihood point source search. The first search presented is the analysis of the full sky using a two-point correlation function and was initially applied in this configuration on IceCube data. The second search uses a method called multi point source analysis, which targets the Cygnus region and is updating a previous result. The third search opens a complete new analysis technique in using IceCube's own events for triggering. Additionally, it includes not only a search for spatial, but also temporal clustering.

In all searches no significant clustering of neutrinos was found and the results are compatible with background. For the full sky upper limits were calculated for the northern and southern hemisphere and are in the same range or better compared to other IceCube analysis. For the Cygnus region IceCube's currently best upper limits have been calculated and the sensitivity of the search has been further improved with respect to the previous analyses. The third analysis explores a new method in applying a self-triggered search on IceCube data, which opens new opportunities in the search for clustering events and might help to reveal the first hint of neutrino point sources.

Zusammenfassung

Das IceCube Neutrino Observatorium im antarktischen Eis bietet einzigartige Möglichkeiten für die Erforschung von Neutrino Emissionen aus galaktischen und extragalaktischen Quellen. Die Entdeckung solcher Neutrinos könnte wertvolle Informationen über den Ursprung der kosmischen Strahlung geben. Im Jahr 2013 konnten die ersten astrophysikalischen Neutrinos mit PeV Energien entdeckt werden. Der Ursprung dieser Neutrinos ist noch nicht erforscht, aber fortgeschrittene Analysetechiken werden entwickelt um die Sensitivität für Punktquellen zu erhöhen. Eine energieabhängige Likelihood-Analyse wurde mit IceCube Daten bereits durchgeführt. Ein koplementärer Ansatz für das bessere Verständnis der Produktion von kosmischer Strahlung ist die Analyse der Korrelation von Ereignissen auf kleinen Skalen bei hochenergetischen Neutrinos.

In dieser Arbeit werden drei Analysen für eine klein-skalige Korrelation dargestellt, die auf einer Zwei-Punkt Korrelationsfunktion basieren. Sie beschäftigen sich mit einem Szenario, in dem nicht nur nach einer einzigen starken Quelle, sondern nach mehreren schwachen Quellen gesucht wird, welche nicht von einer Likelihood-Analyse entdeckt werden können. Die erste Analyse untersucht den vollen Himmel mit Hilfe der Zwei-Punkt Korrelationsfunktion und wurde das erste Mal auf IceCube Daten angewendet. Die zweite Analyse benutzt die sogenannte Multi-Point Source Methode in der Cygnus Region und stellt die Aktualisierung einer früheren Analyse dar. Die dritte Analyse benutzt eine komplett neue Analysetechnik, indem IceCube's eigene Ereignisse als Trigger benutzt werden. Zusätzlich wird nicht nur eine Analyse nach räumlicher, sondern auch nach zeitlicher Korrelation durchgeführt.

In allen drei Analysen konnte keine signifikante Korrelation festgestellt werden und die Ergebnisse sind vereinbar mit Fluktuationen im Hintergrund. Für die erste Analyse wurden obere Grenzen für die nördliche und südliche Hemisphäre berechnet, welche in dem gleichen Bereich oder besser im Vergleich zu anderen IceCube Analysen liegen. Für die Cygnus Region wurden IceCube's derzeit beste obere Grenzen berechnet und die Sensitivität der Analyse konnte im Vergleich zu vorherigen Analysen weiter verbessert werden. Die dritte Analyse untersucht eine neue Methode, indem eine selbst-induzierte Suche auf IceCube Daten angewendet wird. Diese Technik eröffnet neue Möglichkeiten in der Suche nach korrelierten Ereignissen und könnte dazu beitragen die ersten Hinweise auf Neutrino Punktquellen zu entdecken.

Contents

1

Introduction

The measurement of the Higgs boson with the Large Hadron Collider (LHC) in 2013 [1, 2] was one of the major findings in physics in the last years. As a former LHC member, I followed very closely this exiting results achieved after more than 20 years of planning and construction. The Higgs boson is an essential component to the standard model, which has demonstrated huge and continuous success in describing the dynamics of subatomic particles in the last decades. However, the standard model does leave some questions unexplained: What is the dark matter? What are the neutrino masses?

Also in astrophysics a huge progress was made within the last decades. Gamma ray astronomy with now more than 100 detected sources, has pushed forward our understanding of the Universe and contributed to a range of astrophysical questions. Still, the question of the origin and the acceleration of cosmic rays remains one of the biggest challenges in high-energy astrophysics. More than 100 years after the discovery of cosmic rays by Victor Hess [3], we are still not able to understand the fundamental processes leading to the highest energies observed in the Universe.

It became clear, that the observation of the largest structures in our Universe depends strongly on the measurements obtained in particle physics. One natural step is therefore the combination of both fields, emerging in the field of astroparticle physics. With the rise of satellites and the growth of ground-based detectors, a wide range of cosmic particles including neutrinos, gamma rays and cosmic rays at the highest energies can be measured. Especially the neutrino plays a main role in cosmic ray physics, as it is the unambiguous tracer of cosmic ray production.

In hadronic interactions of cosmic rays with surrounding matter, high-energy neutrinos are produced in the direct environment of cosmic ray sources. Possible candidates for such sources are, for example, Gamma Ray Bursts (GRBs) [4, 5] or Active Galactic Nuclei (AGNs) [6, 7], see an overview of candidate sources in Sec. 2. Since neutrinos do not experience deflections or scattering, they are ideal messengers for observing and tracing the hadronic interactions of cosmic rays. However, neutrinos are not only expected from cosmic rays, but also in coincidence with high-energy gamma rays. Thus, the measurement of thousands of gamma-ray sources, like AGNs [8, 9], provides a large number of potential neutrino sources. The detection of such high-energy neutrinos of cosmic origin gives important insights for identifying the sources of cosmic rays [10, 11]. The main difficulty in measuring astrophysical neutrinos are the low cross-sections and the discrimination from the atmospheric background induced by atmospheric neutrinos and muons from cosmic ray interactions at Earth. For this reason, deeply buried detectors with a large detection volume are needed.

The IceCube neutrino observatory, with its large field-of-view, offers a unique opportunity to study the production and interaction of high-energy cosmic rays using neutrinos. The detector, which is located at the geographical South Pole, has a detection volume of $\sim 1\,\mathrm{km}^3$ deep in the Antarctic glacier and an additional $\sim 1\,\mathrm{km}^2$ surface air shower detector, called IceTop. The IceCube detector consists of digital optical modules (DOMs) [12], placed on strings deployed vertically at depths between 1450 m and 2450 m. The strings hold 60 DOMs each equipped with a photomultiplier tube and digitizing electronics to detect neutrinos by measuring Cherenkov radiation of their secondary particles [13], produced in interactions with the ice. A detailed description of the data acquisition system can be found in [12] and in section 4.2.2. The detector was built in several stages between 2005 and 2010, such that each year several strings were added, until reaching the final configuration of 86-strings, containing more than 5000 DOMs.

The IceCube detector [14] recently measured a diffuse cosmic flux of high-energy neutrino events in two years of IceCube data by searching for neutrino-induced events with an interaction vertex well contained within the detector volume [15], for so-called High Energy Starting Events (HESE). The event selection is based on an outer veto layer, discarding events containing muon tracks originating outside of IceCube. The veto region is shown in Fig. 1.1(a), as a grey shaded area. This veto permits one to reduce the dominant atmospheric muon background, as they can not enter the detector without producing light in the veto region. The shaded region in the middle contains ice of high dust concentration, leading to worse reconstruction results and is therefore excluded from this search. The results of this analysis are shown in Fig. 1.1(b). The data in black yields an excess at high energies compared to the background assumption. 28 events with energies between 30 and 1200 TeV were observed on an background of $10.6^{+5.0}_{-3.6}$ events from atmospheric muons and neutrinos.

In a follow-up analysis this diffuse flux was investigated in more detail using three years of IceCube data [16]. This analysis yielded 37 events compared to an expected background of 15.0 events from atmospheric muons and neutrinos. The flux can be described by a E^{-2} neutrino spectrum with a per-flavour normalization of $E^{-2}\Phi(E) = (0.95 \pm 0.3) \cdot 10^{-8}\mathrm{GeV cm^{-2} s^{-1} sr^{-1}}$.

These events could provide information about potential cosmic ray astrophysical sources, but their origin is still unknown. Different attempts were made to assign these events to sources [17], but no conclusive answer is given and resolving these events into

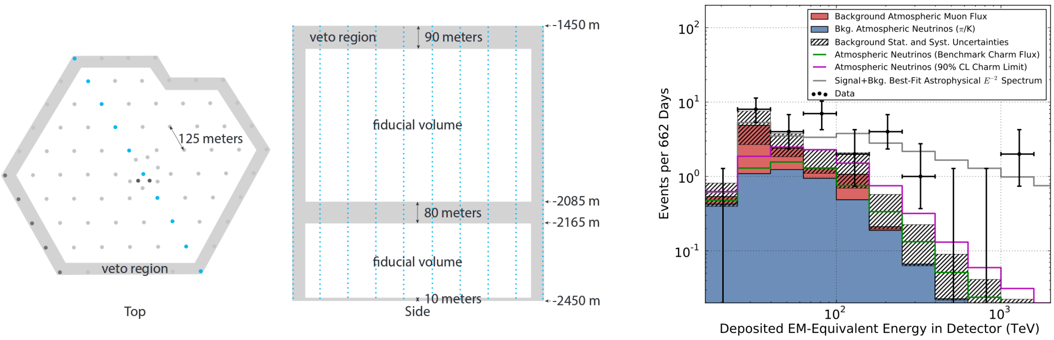

(a) HESE veto layer (b) HESE reults

Figure 1.1.: (a) Sketch of the In-Ice IceCube detector, showing the veto region of the HESE analysis as a grey shaded area. Events producing first light in the veto region were discarded as entering tracks and are not considered in the analysis. The shaded region in the middle contains ice of high dust concentration. (b) Results of the HESE analysis as a function of reconstructed energy. Observed data is shown in black, atmospheric muon and neutrino background in red and blue. An excess of 28 events was found over a background of $10.6^{+5.0}_{-3.6}$ events from atmospheric muons and neutrinos [15].

anisotropies or even into point sources will be one of the main challenges for IceCube. So far no point sources have been discovered with IceCube, but the measurement of the first astrophysical neutrinos motivates additional searches.
IceCube has completed different point source searches, including an energy-dependent likelihood point source search scanning the full sky [18], as well as searches for flaring and periodic neutrino emission [19]. Additionally there are searches for diffuse neutrino emission looking for deviations in the two dimensional distribution of energy and zenith angle [20]. Point source searches are most sensitive for finding individual sources of astrophysical neutrinos among the background of atmospheric events. Diffuse searches, on the other hand, are most sensitive for detecting within this background the presence of high-energy astrophysical neutrinos throughout the sky, without identifying individual sources. In between these two scenarios is the possibility that many weak sources exist. These could contribute to the detected diffuse signal and create a small number of events clustering on the background event distribution, while the individual clusters remain too weak to be detected by the point source searches. This work targets such small-scale event clustering and three different searches will be presented. All use a two-point-correlation (2-pt) function but aim at different regions of the sky.

The main part of this thesis covers these three analyses. The first search presented is a 2-pt analysis of the full sky and was initially applied in this configuration on IceCube data. This results have been published in [21]. The second search targets the Cygnus region and is updating a previous result. The third search opens a complete new analysis technique in using IceCube's own events for triggering. In the self-triggered flare search, the 28 events obtained in the search described above are used as such a

trigger of IceCube data and includes not only the search for spatial, but also temporal clustering.
Beside the work reported here, I also took care of some lower level analysis topics, like the reprocessing of the data sample collected during year 2009 - 2010 in adding new reconstructions.
This work is organised as follows: in Chapter 2 the theoretical background of cosmic ray physics is discussed and a link to gamma ray and neutrino physics is established, while Chapter 3 considers the atmospheric background in neutrino point source searches and presents rejection strategies. The IceCube detector and the principles of neutrino detection are described in Chapter 4. The data sample with IceCube's reconstruction methods and the statistical methods in point source searches are outlined in Chapter 5. The 2-pt analysis of the full sky is presented in Chapter 6, followed by the second search targeting the Cygnus region presented in Chapter 7. The third search, a self-triggered flare search of IceCube data is presented in Chapter 8. A discussion on the systematics follows in Chapter 9 and a conclusion is drawn in Chapter 10.

2

High Energy Neutrinos from Astrophysical Sources

The Earth's atmosphere constantly gets hit by the most energetic particles being produced in the Universe, the cosmic rays. They strike the Earth from all directions and can reach energies up to 10^{20} eV, far higher than the Large Hadron Collider (LHC). In their discovery in 1912, Victor Hess found an increasing electric charge in an ascending balloon experiment and attributed this to a radiation coming from outside the atmosphere. As it was first believed the radiation was of electromagnetic nature, they were named cosmic 'rays' by Millikan 1925 and it took until 1929 that Bothe and Kohlhörster [22] used a Geiger-Müller detector to establish the charged particle theory. Until the 50's, before particle accelerators emerged, cosmic rays were the only source of information about elementary particles, which led to the discovery of the positron [23] and the muon [24]. However, since the dawn of the space age, the main focus of cosmic ray research has been directed towards astrophysical investigations of where cosmic rays originate, what role they play in the dynamics of the Galaxy, and what their composition tells us about matter from outside the solar system [25]. For direct measurements high-altitude balloons and particle detectors build into satellites can be used or ground-based detectors for indirect measurements of the atmospheric shower and in the last years a lot of progress was made in measuring the properties and characteristics of cosmic rays in more details.

In this chapter the nature of cosmic rays will be explained in more detail in a first overview, while in a second part the link to gamma ray and neutrino astronomy will be drawn and possible galactic and extra-galactic cosmic ray sources are discussed.

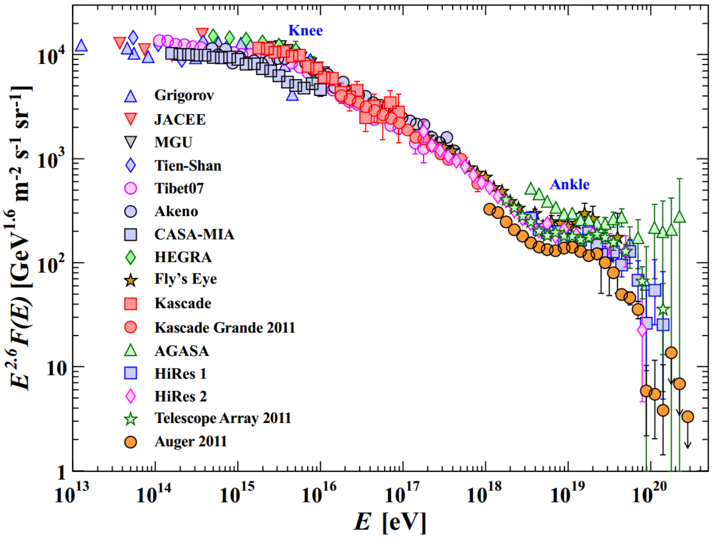

Figure 2.1.: All-particle spectrum of cosmic rays as a function of the energy, using data from several experiments. Two main features are visible, the knee at energies around 10^{15} eV and the ankle at energies above 10^{18} eV. From [27]

2.1 Cosmic Rays

Most of the cosmic rays originate from outside the solar system, distributed throughout our Galaxy.They are mainly composed of protons (90%), but they also include alpha particles (9%) and heavier nuclei [26]. Most of the cosmic rays are relativistic with energies comparable or above their masses. When they collide with a nuclei of the Earth's atmosphere, a shower of secondary particles is generated. These showers consist mainly of light particles as pions and muons, but also neutrinos are produced. Two types of cosmic rays have to be considered: 'primary' cosmic ray particles, accelerated at astrophysical sources and 'secondaries', produced in the interaction with interstellar gas.

Energy Distribution and Flux

The energies of cosmic rays range from 1 GeV up to 10^{12} GeV. The all-particle spectrum as a function of the energy is shown in Fig. 2.1, using data of several air-borne and ground-based experiments. The differential energy spectrum has been multiplied by $E^{2.6}$ in order to display the features of the steep spectrum. Between 10^{15} and 10^{16} eV a steepening occurs, which is known as the knee of the spectrum. Another feature around 10^{18} eV is called the ankle [27]. It is assumed that the part below the knee is of galactic origin, reflecting the fact that the maximum energy of most galactic cosmic accelerators is reached.

The rate at which these particles arrive at the top of the atmosphere decreases with growing energy, from about 10 000 particles per square metre per second at 1 GeV to less than one particle per square kilometre per century for the highest energy. In order to study these Ultra-High Energy Cosmic Rays (UHECRs), detectors with large areas of several square kilometres are required. The flux of low-energetic cosmic rays however, is not only dependent on the energy, but also on the solar wind and the Earth's magnetic field. The expanding magnetized plasma generated by the Sun acts as a barrier to cosmic rays and slows the particles down. This effect is called solar modulation and is correlated with the solar activity. Additionally, cosmic rays are deflected by the field lines of the Earth's magnetic field. Therefore, the intensity of the cosmic radiation depends not only on the energy, but also on the location and the time. The part up to the knee follows a power law of $E^{-2.7}$, while the spectrum above the knee steepens to $E^{-3.1}$, although current measurements indicate a more complex behaviour than a simple power law. The region above the ankle seems to flatten again, but still lacks an established theoretical description [28].

Galactic and Extra-Galactic Cosmic Rays

Cosmic rays up to the knee are believed to originate from inside our Galaxy. However, this view is not yet fully established, also the existence of the knee is still puzzling. Different models for the description of the knee are currently discussed in the literature(e.g. [29]). One of the most popular explanations is a break in the spectra at the source, due to the limited acceleration power of galactic objects, which is related to their size and their magnetic field, see also Sec. 2.3. Other explanations use a so-called 'cannon-ball' model, which yields a cut-off for individual elements proportional to their mass due to effects of relativistic beaming in jets. Another idea is, that the knee is due to propagation effects, which are accompanied by a leakage of particles. The most likely approach will probably be a combination of all of these scenarios [30]. A detailed review on galactic cosmic rays can be found in [31].
The transition from galactic to extra-galactic cosmic rays is assumed to happen at energies between 10^{17} - 10^{18} eV. The ankle can be interpreted as a signature for the transition of a purely extra-galactic cosmic ray spectrum. This scenario seems to be supported by measurements of HiRes data, which find a transition from a heavy to a light composition at energies around $10^{17.5}$ eV, but the full picture remains unclear.
At energies around $5 \cdot 10^{19}$ eV an indication of a cut-off is observed. This is explained with the theoretical Greisen-Zatsepin-Kuzmin (GZK) limit, which describes the interaction of UHECRs with the Cosmic Microwave Background (CMB) over long distances. In this process, a proton is hitting a 2.7 K photon of the CMB and looses energy. Thus, a suppression of particles at energies larger than $5 \cdot 10^{19}$ eV is predicted and could explain the non-observation of particles at higher energies. Analyses from Auger [32] and HiRes [33] may have confirmed such a limit, but large uncertainties remain.

Composition

The composition of cosmic rays is studied mainly by balloon-borne experiments. Besides the major part consisting of protons and alpha particles, heavier nuclei can be

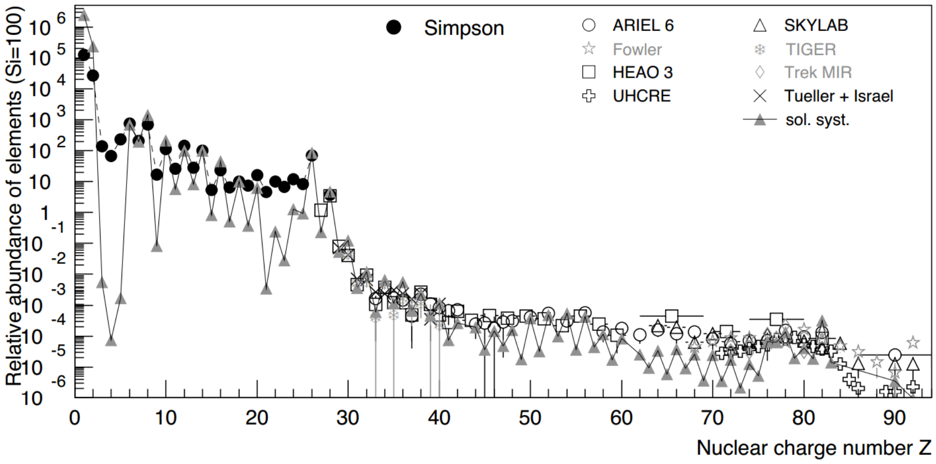

Figure 2.2.: Abundance of elements in cosmic rays as function of their nuclear charge number Z at energies around 1 GeV/n, normalized to Si = 100. Additionally, the abundance of elements in the solar system is shown. [30]

observed. In Fig. 2.2 the abundance of elements in cosmic rays is shown as a function of the nuclear charge number. All elements of the periodic table have been observed in cosmic rays. Their abundances are compared to the abundances in the solar system. Especially for light elements such as Li, Be and B a large discrepancy to the solar system can be seen. Such secondary cosmic rays are assumed to be produced when heavier cosmic rays such as carbon, nitrogen, and oxygen fragment into lighter nuclei during collisions with the interstellar gas. While propagating in a diffusive process through the Galaxy, these particles get deflected many times by the randomly oriented magnetic fields (B $\sim 3\mu$G) [30]. Electrons and positrons constitute only 1 % of galactic cosmic rays.

Detection Methods

For cosmic rays several detection methods are currently in use, dividing into three different types of experiments:

- **Ground-based experiments** e.g. High Resolution Fly's Eye (HiRes) [33], Pierre Auger Observatory [34]
- **Satellites** e.g. Payload for Antimatter Matter Exploration and Light-nuclei Astrophysics (PAMELA) [35], Alpha Magnetic Spectrometer (AMS) [36]
- **High-altitude Balloons** e.g. Balloon-borne Experiment with Superconducting Spectrometer (BESS) [37], Trans-Iron Galactic Element Recorder (TIGER) [38]

Satellites and balloon-borne experiments have the advantage of the direct detection of cosmic rays, although balloons are still affected by thin layers of atmosphere. However, both types of experiments are limited in their collection area, not being able to measure high-energetic cosmic rays. Ground-based detectors are considered as indirect measurements, observing the showers produced via a primary cosmic ray in the atmosphere. They extend the measurements to higher energies and are therefore a complementary addition to satellites and balloons. Ground-based experiments can again be divided into two types: ground arrays using water Cherenkov and scintillation detectors, such as Auger, AGASA [39] and KASCADE [40] or optical detectors, using the fluorescence light emitted by nitrogen atoms in the atmosphere that get excited by a secondary shower particle, such as HiRes.

Cosmic Ray Anisotropy

The arrival directions of cosmic rays could reveal information about their origin and acceleration site. However, as charged particles get deflected in magnetic fields, they do not point back to their originating sources. This makes the identification of sources difficult, since the detailed transport properties of cosmic rays are not well understood with the limited knowledge about the interstellar magnetic fields. In general, the arrival direction of cosmic rays is isotropic and has indeed been confirmed by different experiments, such as Auger, Milagro and IceCube. However, at the largest energies the deflection by magnetic fields decreases and a possible structure may be visible, but with very few statistics. In the last years, observations in the GeV to PeV range have shown, that the arrival directions of cosmic rays have a small anisotropy down to the order of $10^{-4} - 10^{-3}$. This anisotropy varies however with the energy range of the cosmic rays, although its topological structure remains unchanged up to 100 TeV, where it suddenly changes. This observed distribution is dominated by dipole and quadrupole structures, which refers as large-scale anisotropy. After subtraction of this large-scale structures, a non-negligible contribution from higher multipole terms is visible [41]. This observed small-scale anisotropy is however much weaker than the dipole terms and reaches the 10^{-4} level.

IceCube as the only experiment being able to measure the southern hemisphere has completed several studies and can combine its measurements with other experiments on the northern hemisphere. The result of such a combined measurement of IceCube [42] and Milagro [43] data is shown in Fig. 2.3.

The small-scale anisotropies vary at the level of 10^{-4} at energies of 20 TeV. The maps have both been smoothed with a 10° radius. There have been several attempts to explain these observations, such as the contribution of discrete cosmic ray sources at high energies [44, 45] or the diffusion of cosmic rays outside the galactic halo. In this scenario, cosmic rays diffuse outside the galactic disc into the halo, due to the lower matter density in the halo, and create an anisotropy perpendicular to the disk [46]. In addition, Compton and Getting [47] predict a dipole effect in cosmic rays, due to the motion of an observer with respect to an isotropic cosmic ray rest frame. None of the theories have been conclusively confirmed and the picture remains unclear.

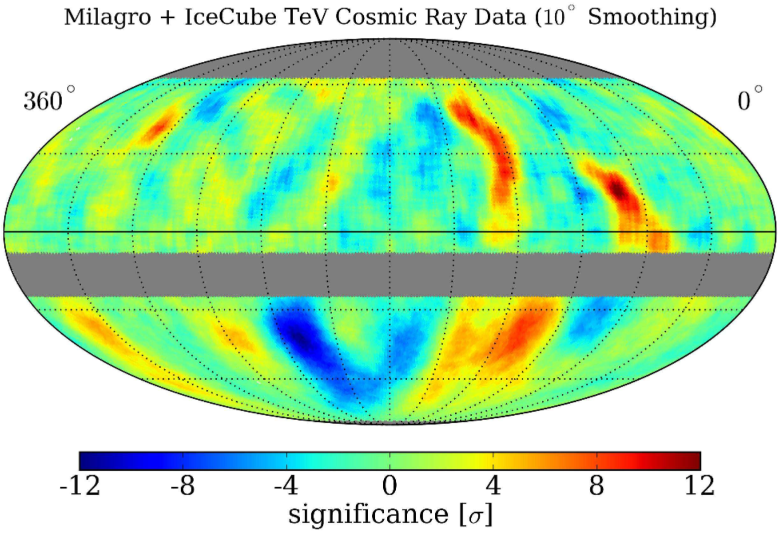

Figure 2.3.: Combined map of significances in the cosmic ray arrival direction distribution observed by Milagro in the northern hemisphere [43] and IceCube in the southern hemisphere. Both maps have been smoothed with a 10° radius [42].

2.2 Neutrinos and Gamma Rays from Cosmic Rays

Cosmic rays are produced in distant high-energy processes in our Universe and the question of their astrophysical origin is of striking interest. However, almost all cosmic rays are charged and suffer deflections by the weak galactic and extragalactic magnetic fields, which sizes and structures are unknown. Cosmic rays appear to be nearly completely randomized in direction and can not be associated to any astrophysical object. Therefore, only neutral particles, such as gamma rays and neutrinos can serve as messengers [48].

Gamma rays from the interstellar medium (ISM) can potentially reveal information about the sources and propagation of cosmic rays. The Galactic diffuse gamma-rays are produced in interactions of particles with gas via neutral pion production, and by electrons via inverse Compton scattering, bremsstrahlung or synchrotron radiation. These processes are dominant in different parts of the spectrum and can provide information about the leptonic components of cosmic rays. In turn, an improved understanding of the galactic gamma ray emission is important for the study of cosmic rays [49]. A sketch of the cosmic ray interaction and propagation is shown in Fig. 2.4.

In this section this connection between gamma rays and cosmic rays, but also neutrinos will be further investigated. The challenge in the interpretation of gamma rays is that they can be produced in two fundamentally different production processes: leptonic and hadronic interaction. Neutrinos however can be generated only in hadronic processes and could solve this ambiguity.

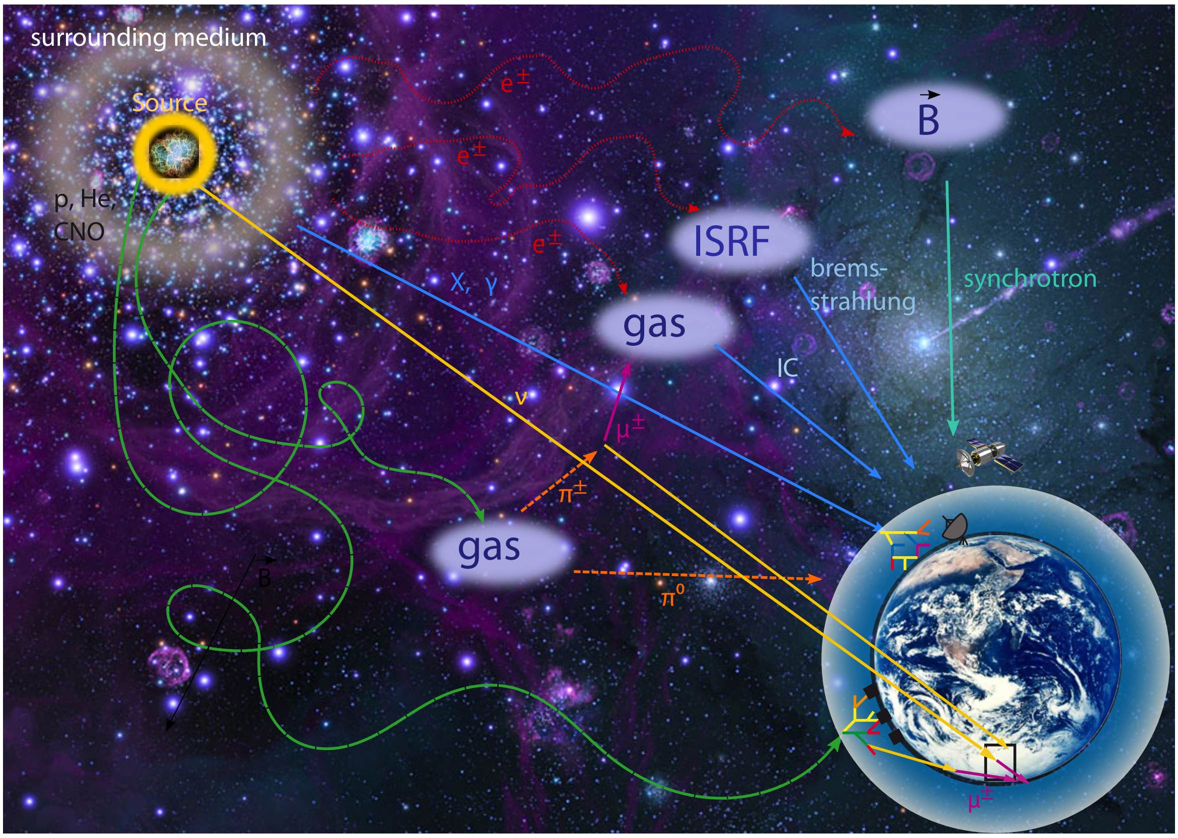

Figure 2.4.: Sketch of the cosmic ray interaction and propagation. Shown are the different types of interaction processes, such as bremsstrahlung, inverse compton and synchrotron mechanisms. Also the decay of neutral pions can produce gamma rays. Neutrinos, however, are produced only in hadronic interactions.

2.2.1 Leptonic Mechanisms

Leptonic interactions involve processes in which high-energy gamma rays are produced via the interaction of relativistic electrons with radiation and matter. Three processes can be distinguished: bremsstrahlung, inverse compton scattering and synchrotron radiation. A more detailed discussion of these mechanism can be found in [50, 51].

Bremsstrahlung

Bremsstrahlung occurs, if a charged particle gets deflected by an electric field of ions or nuclei of atoms. In an astrophysical context, electrons lose most of their kinetic energy in the interaction with ionized gas, which gets transferred into photons, producing gamma-rays. The emissivity of a plasma, having an electron density N_e in the low frequency limit can be written as

$$I(\omega) \approx \frac{Z^2 e^6 N N_e}{12\sqrt{3}\pi^3 \epsilon_0^3 c^3 m_e^2} \left(\frac{m_e}{\kappa T}\right)^{1/2} g(\omega, T) \tag{2.1}$$

where $g(\omega, T)$ is a gaunt factor and N the number density of nuclei. At high frequencies, the spectrum of thermal bremsstrahlung cuts off exponentially as $\exp(-\hbar\omega/\kappa T)$, reflecting the population of electrons in the high energy tail of a Maxwellian distribution at energies $\hbar\omega \gg \kappa T$. This process efficiency is proportional to the electrons energy and the density of the surrounding gas. In space, bremsstrahlung is observed in regions containing ionised gas, generating radio emission and in very hot (10^7K) intracluster medium.

Inverse Compton Scattering

A second mechanism, producing gamma-rays is the Inverse Compton scattering. In this process energy from a relativistic electron is transferred to a photon, generating high-energy gamma rays. It is assumed to be one of the dominant processes in the production of gamma-rays. It is probably responsible for the gamma ray emission in some quasars, at the base of AGN jets and in the extended regions of radio galaxies. For low energetic photons $E_\gamma \ll m_e c^2$ the scattering of electrons falls into the Thomson regime, while for $E_\gamma \gg m_e c^2$ quantum effects become important and the regime is called Klein-Nishina. The cross section for this regime can be described by

$$\frac{d\sigma_{KN}}{d\Omega} = \frac{r_0^2}{2}\left(\frac{E_{\gamma i}}{E_{\gamma s}} + \frac{E_{\gamma s}}{E_{\gamma i}} - \sin^2\theta\right) \tag{2.2}$$

with r_0 being the classical electron radius. In order to calculate the spectrum of the scattered radiation, the Klein-Nishina cross-section and the density of photons at each point of the electron path needs to be considered. Since the electron is suffering collisions from photons from various angles along its path, the geometry of the scattering gets complicated. As an approximation a segment of isotropic photon gas of differential density $dn = n(\epsilon)d\epsilon$ is used. The scattered photon spectrum can then be expressed by

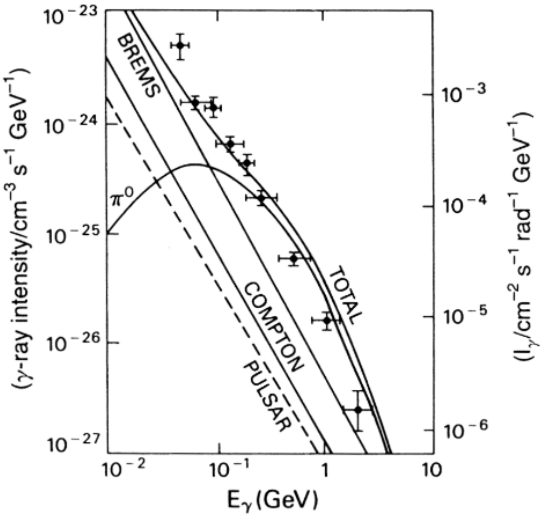

Figure 2.5.: Galactic gamma ray spectrum and theoretical measurements for bremsstrahlung, inverse compton and π_0 decay, which is dominating at energies E>70MeV [52].

$$\frac{dN_{\gamma,\epsilon}}{dtdE_1} = \frac{2\pi r_0^2 mc^3}{\gamma}\frac{n(\epsilon)}{\epsilon} \cdot \left[2q\ln q + (1+2q)(1-q) + \frac{1}{2}\frac{(\Gamma_e q)^2}{1+\Gamma_e q}(1-q)\right] \tag{2.3}$$

in using the energy of the scattered photon in units of the initial electron $\epsilon_1 = \gamma mc^2 E_1$ and $\Gamma_e = 4\epsilon\gamma/mc^2$ and $q = E_1/\Gamma_e(1-E_1)$. The parameter Γ_e determines then the domain of the scattering, $\Gamma_e \ll 1$ belongs to the Thomson limit, in which the photon energy remains nearly unchanged. However, the photon can gain energy in multiple scattering, since the Thomson cross-section is high. For $\Gamma_e \gg 1$, in the Klein-Nishina regime, the probability of scattering decreases, but large energy losses in individual Compton scattering become dominant [50].

In Fig. 2.5 the galactic gamma ray spectrum as well as theoretical estimates [53] are shown. At energies below 70 MeV relativistic bremsstrahlung might be the dominant source. At energies above 70 MeV the dominant gamma ray emission mechanism is the decay of neutral pions, created in collisions of cosmic rays with the ISM, which is described in the next section [52].

Synchrotron Radiation

Synchrotron radiation emerges, if a charged particle as a relativistic electron spirals around magnetic field lines. In this process electrons radiate photons, which energy corresponds to the electron radius in the magnetic field. The radiation is strongly polarised in the direction of the electrons motion, which is called 'beaming'. The total energy loss of such an electron is given by

$$-\frac{dE}{dt} = 2\sigma_T c \cdot U_{mag} \left(\frac{v}{c}\right)^2 \gamma^2 \sin^2(\theta) \tag{2.4}$$

with the Thomson cross-section σ_T, the energy density of the magnetic field $U_{mag} = B^2/2\mu_0$ and the angle between the electron and the magnetic field lines θ [52]. The emitted spectrum of a single electron can be written as

$$P(\nu) = \frac{\sqrt{3}e^3 B}{mc^2} \frac{\nu}{\nu_c} \int d\xi K_{5/3}(\xi) \tag{2.5}$$

with the critical frequency $\nu_c = \dfrac{3eB\gamma}{4\pi mc}$, the magnetic field B and $K_{5/3}(\xi)$ being the modified Bessel function of 5/3 order [50]. The maximum of the emission spectrum that is following a power law, is given by $\nu_{max} = 0.29\nu_c$. In astrophysical contexts, synchrotron radiation may account for the radio, optical and X-ray flux of objects and is responsible for the optical and X-ray emission of the Crab Nebula.

2.2.2 Hadronic Mechanisms

The more important mechanism for this work are the hadronic interactions, since they produce not only gamma-rays, but also neutrinos, which can conclusively identify sources of cosmic ray acceleration. If a high-energy particle interacts with its surrounding matter, such as molecular clouds close to the origin of the cosmic ray, high-energy neutrinos can be produced. This is possible in two processes, nucleon interactions via

$$\begin{aligned} p + p &\longrightarrow \pi^0 + 2p \\ p + p &\longrightarrow \pi^+ + n + p \end{aligned} \tag{2.6}$$

and photonuclear interactions via

$$\begin{aligned} p + \gamma &\longrightarrow \pi^+ + n \\ p + \gamma &\longrightarrow \pi^0 + p \end{aligned} \tag{2.7}$$

The mesons can then decay again via different channels into photons and neutrinos:

$$\begin{aligned} \pi^0 &\longrightarrow 2\gamma \\ \pi^+ &\longrightarrow \mu^+ + \nu_\mu \\ \pi^- &\longrightarrow \mu^- + \bar{\nu}_\mu \end{aligned} \tag{2.8}$$

The cross-section for $p\gamma$ interaction is about a factor of 100 smaller than the pp interactions. Nevertheless, they are important in environments, in which the target photon density is much higher than the matter density, which is typical for the most astrophysical systems. In the traditional view, pp interactions seem to be more important

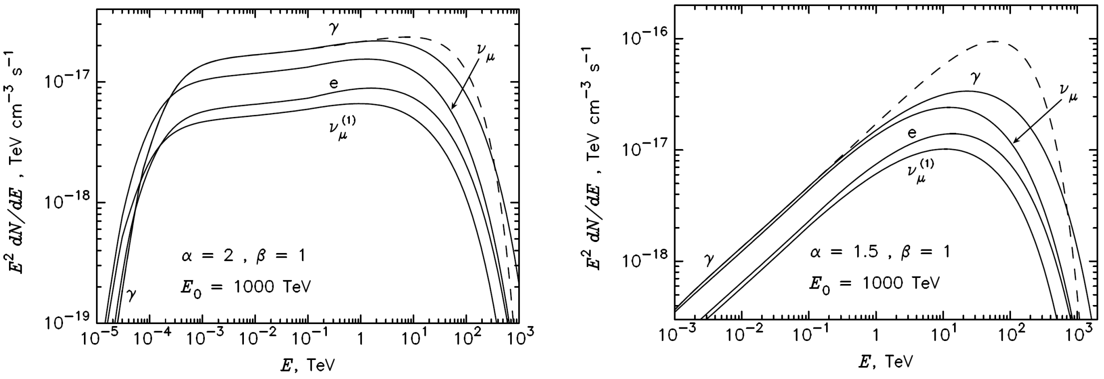

(a) Energy spectra with α=2

(b) Energy spectra with α=1.5

Figure 2.6.: Energy spectra of gamma rays and neutrinos from *pp* interactions for a source energy spectrum of $dN/dE \propto E^{-\alpha} \cdot e^{-(E/E_0)^\beta}$ with (a) α=2 and (b) α=1.5 [55].

in the Galaxy, while $p\gamma$ interactions are mostly responsible for the neutrino production in extragalactic sources, but this view has currently been modified [54].

The energy spectrum of neutrinos follows closely the energy spectrum of the primary cosmic rays. The production of neutrinos is strongly coupled to the production of gamma rays in hadronic interactions, but not in leptonic processes. In models describing the expected neutrino flux following the gamma ray flux, these leptonic processes are neglected. In Fig. 2.6 such a model for neutrinos and gamma rays is shown for a source with spectrum $dN/dE \propto E^{-\alpha} \cdot e^{-(E/E_0)^\beta}$ for two different parameters of α. In both figures the resulting neutrino flux is roughly a factor two below the gamma ray flux and shows an earlier cutoff. It should be noted, that the hardening of the spectra around 0.1 TeV in Fig. 2.6(a) is caused by the increase of the inelastic cross-section, which becomes significant at energies above 1 TeV [55].

The neutrinos are produced at different flavour ratios, depending on their production mechanism. As most of the astrophysical neutrinos are believed to be produced by the decay of charged pions the flavour ratio is $\nu_e : \nu_\mu : \nu_\tau = 1 : 2 : 0$, assuming that the muon decays into neutrinos before it loses a significant fraction of its energy. In a second scenario, the muon may lose its energy by interacting with strong magnetic fields or with matter, which eventually decays into neutrinos with energies much lower than that from pion decays. Then the flavour ratio for this type of source changes to $\nu_e : \nu_\mu : \nu_\tau = 0 : 1 : 0$ and is called muon-damped source. A third type of source is believed to emit neutrons, originating from the photo-dissociation of heavy nuclei. As neutrons produce ν_e via β-decay, while propagating to the Earth the neutrino flavour ratio results in $\nu_e : \nu_\mu : \nu_\tau = 1 : 0 : 0$. However, the expected ratio at Earth changes from the numbers of the pion decay duo to neutrino oscillations to $\nu_e : \nu_\mu : \nu_\tau = 1 : 1 : 1$.

2.2.3 Gamma Ray Astronomy

Additionally to the direct measurement of cosmic rays, gamma rays produced in the acceleration processes of primary cosmic rays can be used to search for their origin. However, they get also produced in leptonic processes and can not conclusively establish the sources of cosmic radiation. Also they can get absorbed in molecular clouds and reach not necessarily the Earth. Nevertheless, they are not deflected by magnetic fields, as charged particles and point back to their origin. Due to much higher cross-sections than e.g. neutrinos, they are also much easier to detect. The observation range for gamma-ray telescopes starts above the X-ray regime at energies of $\sim 100\,\mathrm{keV}$.

Since the atmosphere of the Earth is not transparent for gamma rays, direct detection needs platforms in space. The most important observatories in terms of satellites are the Energetic Gamma Ray Experiment Telescope (EGRET) and its successor Fermi-LAT, launched in 2008. However, above $\sim 10\,\mathrm{GeV}$ gamma ray fluxes decrease dramatically and larger detection areas are not affordable for space-based platforms. Therefore, at higher energies a second type of experiments becomes important: ground-based techniques reconstructing atmospheric showers [56]. They can be categorized in the following two groups:

- **Imaging Atmospheric Cherenkov Telescopes (IACTs)** e.g. High Energy Stereoscopic System (HESS), MAGIC, Very Energetic Radiation Imaging Telescope Array System (VERITAS), Cherenkov Telescope Array (CTA)
- **Water Cherenkov Telescopes** e.g. Milagro, High-Altitude Water Cherenkov Observatory (HAWC)

IACTs use the Cherenkov radiation of relativistic electrons, produced in the electromagnetic showers to reconstruct the original gamma ray. With telescopes with a diameter of $10\,\mathrm{m}$ and collection areas of $10\,\mathrm{m}^2$, high energy primary gamma rays can be detected. From the number of registered photons, the direction of the shower and its shape, the energy, the arrival direction and the character of the primary can be reconstructed. However, IACTs are limited in the search of very extended structures or solitary events as GRBs. Therefore, Water Cherenkov Telescopes, such as Milagro or HAWC, are a complementary addition to IACT telescopes. Widely-spread Water Cherenkov telescopes were originally designed for the detection of high-energetic cosmic rays. In order to adopt the technique for gamma ray astronomy, the energy threshold needs to be lowered by a few orders of magnitude in using dense arrays at high altitudes [56]. In the future, the next generation of IACTs, such as CTA, will extend the field of gamma ray astronomy even further.

2.3 Candidate Sources of Cosmic Rays

Candidate sources for the origin of cosmic rays cover a large variety of objects, ranging from supernova remnants to gamma ray bursts or processes in active galaxies. In this

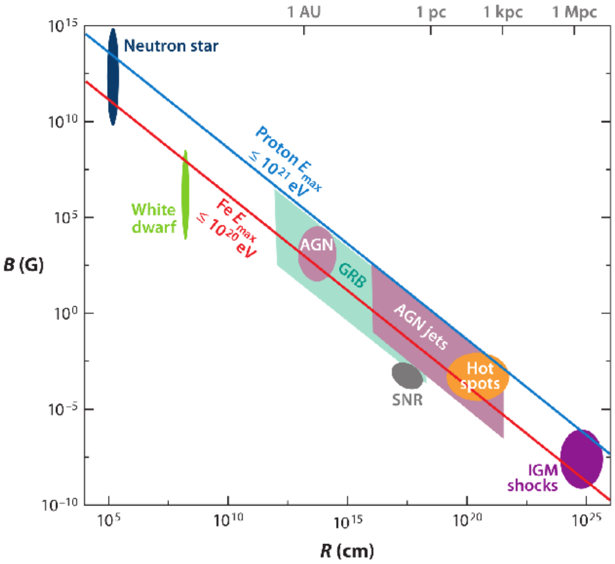

Figure 2.7.: Hillas diagram showing the B-R phase space of different candidate source with their uncertainties. Above the blue (red) line protons (iron nuclei) can be confined to a maximum energy of $E_{max} = 10^{20}$ eV. The region occupied by each source type indicates the uncertainties in their parameters. [58].

section a brief description of constraints on the acceleration sites and the acceleration mechanisms will be given and a discussion about potential galactic and extra-galactic sources will follow in the next sections.

In revealing the sources of cosmic rays, two approaches have to be considered: top-down scenarios assume that cosmic rays are produced as secondaries of the decay of heavy particles, while in bottom-up scenarios, cosmic ray particles are accelerated within regions of intense magnetic fields [57]. Neutrinos are assumed to be produced in both scenarios, however the detection of a neutrino point source would strongly favour a bottom-up scenario.

2.3.1 Hillas Criterion

For being considered as a possible source of acceleration different criteria have to be fulfilled. Apart from the density and power of an object, also its geometry needs to be considered. If a particle is accelerated by a magnetic field, its Larmor radius should not exceed the size of the accelerator. This criterion is recognized as the Hillas criterion [59] and can be expressed by

$$E_{max} \leq qBR \tag{2.9}$$

with E_{max} the energy gained by a particle with charge q in a region of size R and the magnetic field B. A version of a Hillas plot, illustrating the constraints on B and R is shown in Fig. 2.7. In this plot candidate sources are placed into the B-R phase

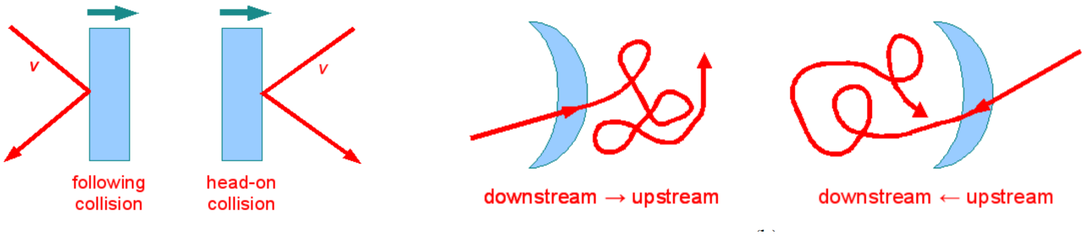

(a) Second-order Fermi Acceleration

(b) First-order Fermi Acceleration

Figure 2.8.: (a) Second-order Fermi Acceleration showing the magnetic mirror on which the particle gets reflected. (b) First-order Fermi Acceleration using a shock front for the deflection of the particle [57]

space, including their uncertainties. Sources above the top line are able to accelerate protons up to 10^{20} eV, while sources above the bottom line are able to accelerate iron up to 10^{20} eV. The most promising candidates for acceleration sites in this context are Supernova Remnants (SNRs), Active galactic Nuceli (AGNs) and Gamma Ray Bursts (GRBs).

2.3.2 Acceleration mechanisms

In order to search for suitable sources of cosmic rays, the acceleration mechanisms have to be understood. The mechanism to accelerate particles to such extreme energies are still under investigation, although currently accepted models exist. In the following two of these models will be discussed.

Second-Order Fermi Acceleration

In 1949, Fermi [60] proposed a process describing the efficient acceleration of particles, which was later called second-order Fermi acceleration. It explains the acceleration with the interaction of primary cosmic rays with interstellar clouds in the Galaxy. These clouds move randomly and can be treated as a magnetic mirror, in which the particle gets reflected. Statistically, more head-on than following collisions between the particle and the magnetic mirror occur and in each collision the particle gains energy. This reflection mechanism is shown in Fig. 2.8(a). It is called second-order, since the energy gain in each collision $\Delta E/E$ is proportional

$$\frac{\Delta E}{E} \propto \frac{8}{3}\left(\frac{v}{c}\right)^2 \tag{2.10}$$

with v and c the speed of the cloud and the particle, respectively. Although the mechanism succeeds to produce a power-law it can not explain the observed value of 2.7 in the exponent [57].

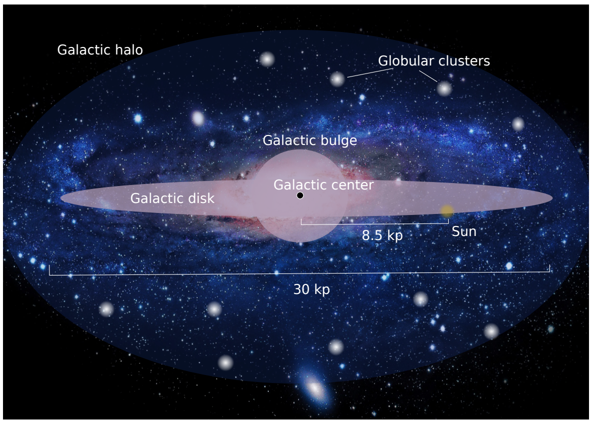

Figure 2.9.: Sketch of the structure of the Milky way. Shown are the galactic center with the bulge and the rotating disk. The Sun is located ~8.5 kpc from the galactic center. Adapted from [63]

First-Order Fermi Acceleration

Fermi's suggestion eventually led to a more efficient model, see [61]. It is the currently accepted model and is called first-order Fermi acceleration. It uses the existence of a strong shock front caused by a supernova or a supernova remnant (SNR) and is believed to explain cosmic ray acceleration up to the knee. This shock front is assumed to move super-sonically compared to the speed of the gas. The gas in front of the shock is called upstream, after it has passed the shock wave downstream. The particle is repeatedly deflected by the shock waves, crossing the downstream and upstream regions several times, as illustrated in Fig. 2.8(b). In each circle an energy gain $\Delta E/E$ of

$$\frac{\Delta E}{E} \propto \frac{4}{3}\left(\frac{v}{c}\right) \tag{2.11}$$

can be achieved. High-energetic particles are assumed to stayed longer in the shock waves, repeating more acceleration circles. The energy gain of the particle is then linearly proportional to the velocity v/c of the shock wave. This leads to an upper limit of $E_{max} \approx Z \cdot 10^{14}$ eV for Supernovae Type II [62, 30].

2.4 The High Energy Galaxy

In this chapter possible sources for cosmic ray and neutrino emission inside the Galaxy will be discussed.

The Galaxy is the main target in the search for the sources of cosmic rays and thus, for neutrino emission. It is a barred spiral-galaxy with a diameter of 30 kpc and a width of 0.3 kpc. The center builds a bar-shaped region, which is surrounded by a large flat disk containing large amount of stars, gas and dust, see Fig. 2.9. The Sun is located 8.5 kpc from the galactic center, consisting of a super-massive black hole with a mass of $4M_{\odot}$.

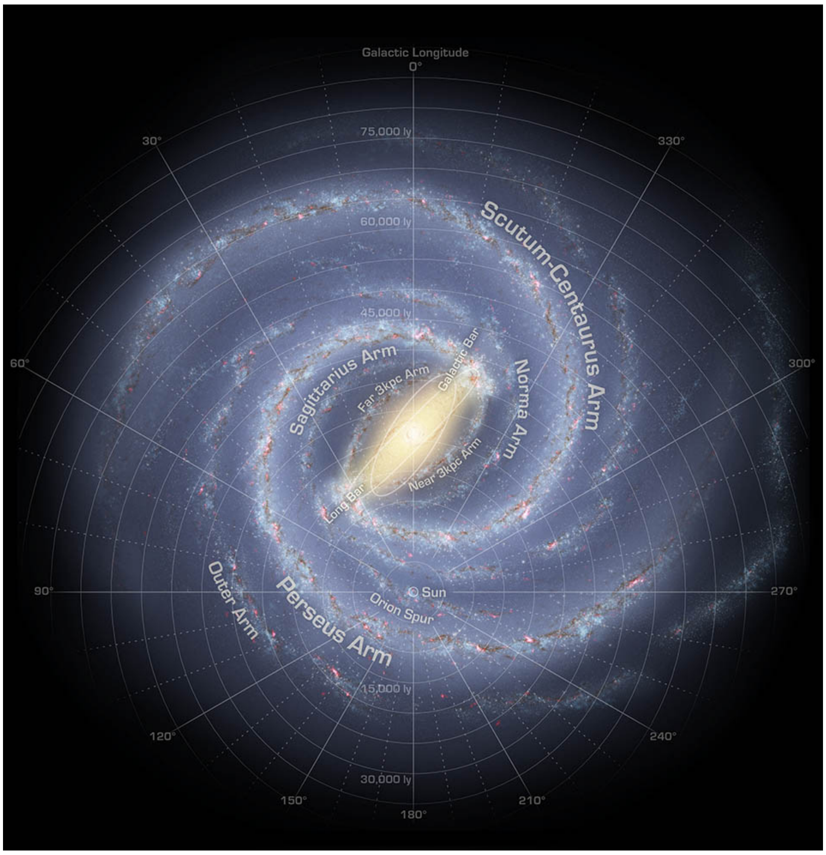

Figure 2.10.: Artistic view of the Milky Way, revealing its spiral structure [64].

Around the black hole a dense concentration of mass, mainly containing old stars, is spread in a spherical shape, called bulge region. This region extends up to 1.5 kpc and includes a complex radio source, Sagittarius A. This region is assumed to contain a significant amount of the Milky Ways star formation activity and is very active in high-energy gamma rays. Outside the galactic bar, the Milky Way is organised in four spiral arms. Figure 2.10 shows an artistic view of the Milky Way, illustrating its spiral structure. It is based on IR-measurements, obtained with the Spitzer telescope. The two main components are the Perseus arm and the Scutum-Centaurus arm, both starting near the Galactic Center. The Sun is supposed to be contained in a sub-arm of the Perseus arm, called Orion Spur.

The disk of the Milky Way contains mainly stars, atomic and molecular gas. It can be mapped by the distribution of neutral hydrogen (HI) via the 21 cm line and shows a diffuse distribution of denser regions, called clouds. They can even reach masses of $10^4 - 10^6 M_\odot$ and are then called giant molecular cloud complexes (GMC). They are among the most prominent candidates for star formation regions. The disk is surrounded by a spheroidal halo, which is believed to be constituted of dark matter, due to the observed mass discrepancies in the rotation curve of the Galaxy. In the following a few selected regions and objects inside the Galaxy, which are promising candidates for neutrino emission will be discussed.

2.4.1 The Cygnus Region

The Cygnus region is one of the brightest diffuse gamma ray emission region in the Galaxy and thus, a promising region for possible neutrino emission. It has been studied in a broad range of wavelengths, going from radio to TeV gamma rays. It is roughly located within Galactic longitudes of 70°- 90° and latitudes of -4° - 8°. From the Earth's point of view, this part of the sky is considered to look down a spiral arm, meaning that regions from only a few hundred pc to several kpc are superposed [65]. Even a projection of the Perseus and the Outer arm has to be considered and complicates the interpretation of the observations. It contains a variety of possible cosmic ray accelerators, such as several massive giant molecular cloud complexes, Wolf-Rayet stars, OB associations and numerous regions of young stars with different masses. Additionally, it is one of the richest known regions in terms of star-formation.

The most studied regions are the North America and Pelican Nebulae and the Cygnus X region, a large ∼10° wide radio emission feature, composed of numerous individual HII regions [65]. Cygnus X contains a large number of massive protostars and the largest known stellar association in the northern hemisphere, Cygnus OB2. Infrared observations indicate that Cygnus OB2 may contain more than 2000 OB stars, with a total stellar mass that could be as high as $10^5 M_\odot$ [66]. The existence of a large number of massive protostars makes Cygnus-X to one of the most active and massive star-forming complexes within only two kpc from the Sun.

A strong TeV gamma ray emission was observed by several experiments, such as Milagro and Veritas. The Milagro sky survey identified several bright and extended high-energy gamma ray sources in the region [67]. A big challenge in the analysis of the region is the proper separation of the gamma ray flux, attributed to point or extended sources or a diffuse emission [68]. MGRO J2019+37 and MGRO 2031+41 are considered to be among the brightest TeV-objects in this region, shown in Fig. 2.11(a) with Milagro data. For MGRO J2019+37 the emission can be well fitted by a power law with an exponential cutoff ($E_c = 29^{+50}_{-16}$TeV) and a spectral index ($\alpha = 2^{+0.5}_{-1}$), while a simple power law is disfavoured [68]. However, the flux has not been confirmed by other experiments and its inner structure remains unresolved. New measurements by Veritas suggest at least two separate sources, see Fig. 2.11(b), but the picture remains complex [69].

The emission of MGRO 2031+41 can be modelled by a power law with $\alpha = 3.22^{+0.23}_{-0.18}$ and agrees with measurements from ARGO. The morphology seems to be structured by a central point-like source with extended emission, possibly produced by other unresolved sources [68]. HAWC, the successor of Milagro, might be able to produce a more accurate picture of this region.

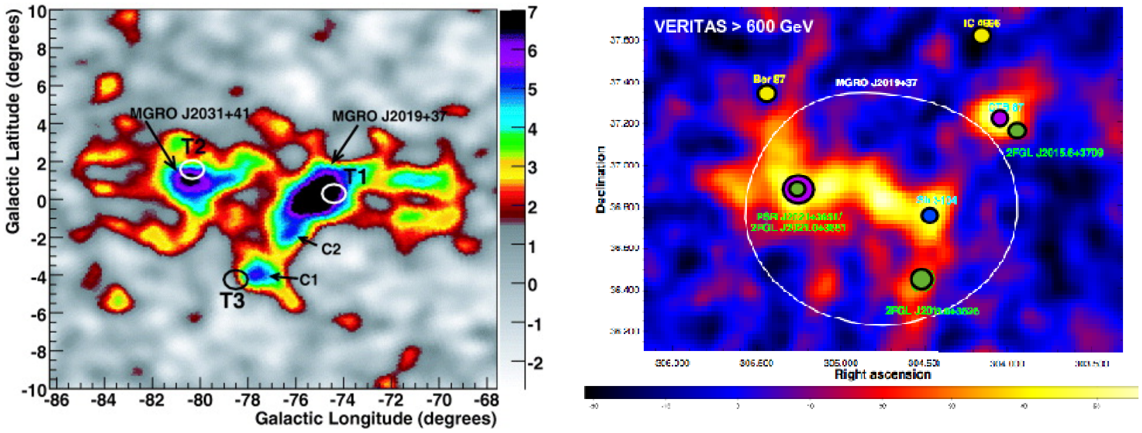

(a) Milagro

(b) Veritas

Figure 2.11.: (a)The Cygnus Region as seen in TeV gamma rays. The color scale represents observations from the Milagro observatory. [70]. (b)blow-up of the Cygnus OB1 region showing the excess counts at energies above 600 GeV observed by VERITAS (color scale). Fermi-LAT sources are shown by the filled green circles. Other known sources are shown by the filled yellow, purple and blue circles. [71]

2.4.2 Supernova Remnants (SNRs)

At final stage of its evolution a star has consumed its hydrogen and heavier elements for the fusion reactions counteracting the gravitational pressure. If the star is massive enough ($>8M_\odot$), its stellar core will collapse and the star explodes in a supernova, ejecting its outer shell. Depending on the stars mass, a neutron star or a black hole is established. The remaining outer shell is called a supernova remnant (SNR). They are able to heat the surrounding medium and are suspected for a long time to accelerate cosmic rays to extremely high energies. There are different types of SNRs: shell-like or composite, with a pulsar wind nebulae (PWN) in the center, which will be discussed in the next section.

Shell-like SNRs are considered to radiate thermal emission from shock-heated gas and non-thermal emission from shock-accelerated particles. As discussed in Sec. 2.3.2, particles get accelerated in the SNR via the interaction with shock fronts. This particles can then interact with ambient magnetic fields or with matter. While the SNR expands over a thousand years, it undergoes different stages. The first phase is the free-expansion, which is dominated by the explosion of ejecta from the stellar progenitor and kinetic energy is transferred into the ISM. This phase can last a few hundred years. At the end of the free expansion phase the ISM builds significant pressure on the ejecta, forming a reverse shock. This phase is called Sedov-Taylor phase and is characterized by high temperatures and strong magnetic fields. While decelerating radiative losses become more important and the ejecta is cooling down and forming a thin, dense shell.

As the SNR passes trough the free expansion stage, the amount of relativistic particles increases and reaches a maximum in the early Sedov-phase. Correspondingly, the gamma ray luminosity peaks around $10^3 - 10^4$ years after the supernova explosion [56].

2.4.3 Pulsar Wind Nebulae (PWNe)

A pulsar wind nebula is a nebula powered by the wind of a pulsar in its center. A pulsar originates from a rotating neutron star, that can be formed in a supernova explosion. At the beginning of its evolution the nebula around the pulsar can expand freely into the supernova ejecta, providing a constant wind power, which accelerates the swept-up shell of the ejecta. At a timescale of 10^3 years the nebula expands adiabatically. After 10^4 years the interaction of the SNR with the surrounding medium produces a reverse shock front, that travels back to the center of the remnant, while compressing the nebula. This results in constant contraction and expansion of the PWN [72].
Relativistic winds from the pulsar can transport most of their rotational power into the surrounding medium and accelerate particles to high energies during the expansion or in shocks, that are generated in a collision of the winds with the sub-sonic environment. Accelerated leptons can then interact with the magnetic fields and produce a non-thermal radiation reaching energies of $\sim$100 TeV. For magnetic fields of a few μG, electrons create a nebula of synchrotron radiation around the pulsar, usually observed in the radio band, but also going up to X-ray energies. At high energies, comptonization of soft photons and relativistic electrons can take place and produce an extended IC-nebula around the pulsar [56].
One of the best observed PWN is the Crab nebula, shown in Fig. 2.12, corresponding to a supernova observed by chinese astronomers in 1054. It is located at a distance of $\sim$2 kpc and has a diameter of 3.4 pc. For many years, the Crab served as standard candle for cross-calibrations of gamma ray measurements in being the brightest persistent point-like TeV gamma ray source, with a steady gamma ray flux above 1 TeV of $(2.1 \pm 0.1_{stat}) \cdot 10^{-11}\mathrm{GeV cm^{-2} s^{-1}}$.

2.5 The Extra-Galactic Sky

It is believed that the cosmic ray spectrum above energies ($E>10^{17}$eV) are of extra-galactic origin. The two most promising candidates for extra-galactic source are Active Galactic Nuclei (AGN) and Gamma Ray Bursts (GRBs) and will be discussed in the following.

2.5.1 Active Galactic Nuclei (AGN)

An Active Galactic Nuclei (AGN) is the inner region of a galaxy, which yields an extremely high luminosity ($L > 10^{42}$erg/s) in a very compact and dense environment. Emission has been observed in almost all wavebands, going from radio to gamma rays, being able to exceed the emission of all other objects in that galaxy. All that emission

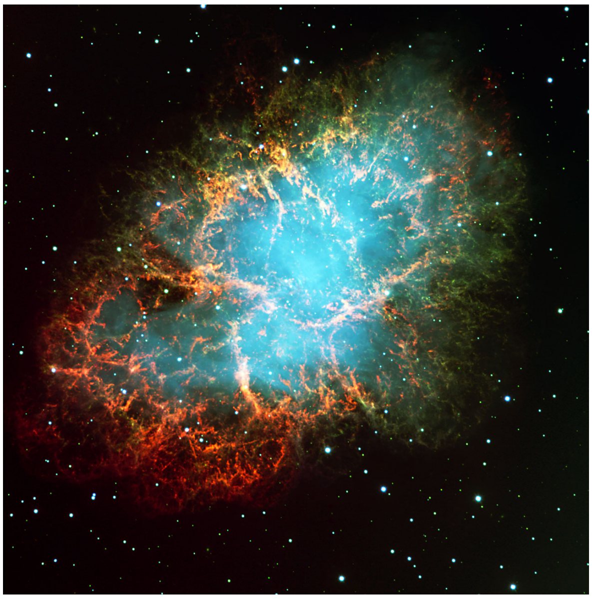

Figure 2.12.: The Crab Nebula as seen with the Hubble Space Telescope [73]

is coming from a region, that is small by galactic standards and not bigger than our solar system.This high power can only be achieved by the accretion of matter into a deep gravitational potential and can not be explained by nuclear reactions. Nowadays it is agreed, that a supermassive black hole ($\geq 7M_{\odot}$) in the center of the galaxy creates this high luminosity by accretion of mass [74]. A galaxy having such a black hole in its center is called 'active galaxy', characterizing at least 5% of the galaxies in the Universe. The gravitational energy of the accreted matter can be transferred into mechanical and electromagnetic energy, and can result in one or two-sided jets.

Matter that is drawn towards the black hole will lose angular momentum via turbulent processes in the accretion disk, which radiates UV and soft X-ray emission. Hard X-rays may also be produced in the vicinity of the black hole via hot electrons above the disk. In so called 'broad-line' regions, clouds of gas are moving rapidly towards the black hole and produce strong optical and UV emission. Outside the obscuring torus slower moving clouds, the 'narrow-line' region produces narrow emission lines. At the poles, outflows of particles can occur and form collimated radio-emitting jets. The particles in a jet have very high velocities, beaming radiation relativistically in the forward direction [75].

These objects can be divided into two groups: radio-loud and radio-quiet AGNs, where the separation depends on the ratio of the 5 GHz radio flux and the optical B band, $R_L = \log(F_{5GHz}/f_B)$. Radio-loud corresponds to $R_L \gg 1$, which make probably 10% to 15% of all AGNs and radio-quiet AGNs, where $R_L \ll 1$. Both groups can be further classified into different subcategories, while the classification depends strongly on our orientation towards the AGN:

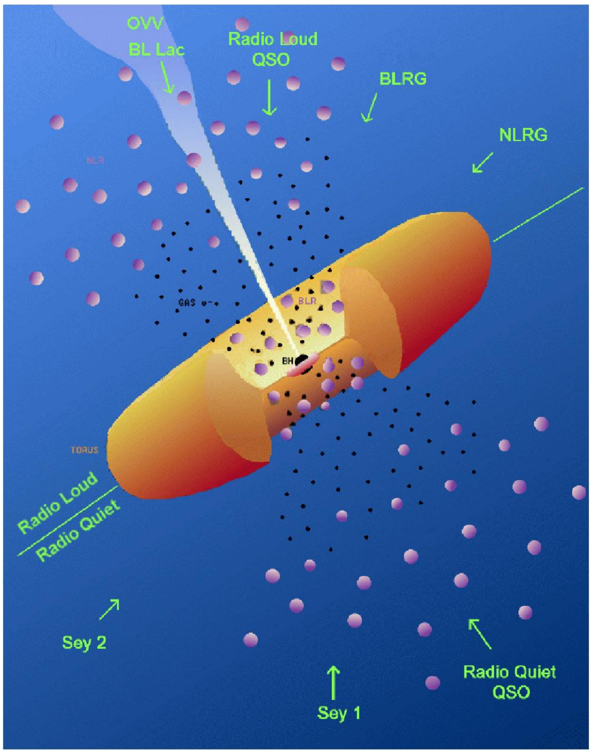

Figure 2.13.: Sketch of an AGN. Shown are the different components, such as the black hole and the narrow line and broad line regions. Depending on our orientation to the AGN, different classifications can be made. Adapted from [75, 77]

Quasars (quasi-stellar radio sources) are the brightest members in the AGN class at large distances. Their spectra covers the entire electromagnetic spectrum.

Blazars are rapidly variant source, as the jet is pointing directly towards the Earth. The name comes from the combination of quasars and BL Lac objects, since they appear to have a mixture of properties of both classes.

Seyfert Galaxies are lower luminosity AGNs with two subclasses, Type I or II, depending on the presence of broad line components.

Radio Galaxies can be divided again in radio-loud and radio-quiet AGNs, depending on the viewing angle, They are typically associated with giant elliptical galaxies, very similar to Seyfert galaxies [76].

Qasars and Blazars belong to the radio-loud group, while Seyfert galaxies belong to the radio-quiet AGNs. A sketch illustrating the different classifications is shown on Fig. 2.13.

2.5.2 Gamma Ray Bursts (GRBs)

Gamma Ray Bursts are outbursts of gamma rays, which can outshine every other object in gamma rays. Bursts are observed on timescales of some ms to some minutes, dividing GRBs into short and long GRBs. The gamma ray fluxes that are measured imply a total energy of $10^{54}\Omega_{\gamma}/4\pi$, where $\Delta\Omega_{\gamma}$ is the solid angle into which the gamma-rays are beamed. They were first discovered in the late 1960's by the U.S. Vela satellites and until the late 90's there existed no detection in softer wavelengths. 1997 the Beppo-SAX satellites provided first measurements of X-ray and optical afterglows and allowed measurements of their distances via the redshift.

The current interpretation of such enormous energy outbursts assume that a large amount of gravitational energy ($\sim 1M_{\odot}$) is released in a narrow beam of gamma rays, produced by a supernova or the merger of binary neutron stars. The largest amount of energy would escape in the first few seconds as neutrinos. In the fireball shock scenario, a high temperature fireball is expanding at relativistic speed, which can undergo internal shocks, leading to gamma rays. As it decelerates against the external medium it would develop into a blast wave and a reverse shock, producing a weakening afterglow. The resulting photon output is only in the range of a few percent of the total energy output, but even this is comparable to the optical output by a supernova over weeks. This scenario has been able to predict many observed properties of the bursts and leads the current understanding of GRBs [78, 4].

In contrast to most other astronomical transient sources, the light curves of GRBs are extremely diverse and complex and a classification is difficult. Not only the duration of the bursts can vary between ms and tens of minutes, but also the shape of the light curve can differ intensely [79]. They are divided into two main groups based on their duration and spectral hardness: short gamma ray bursts with durations of less than 2 s and rather hard spectra and long gamma ray bursts with durations longer than 2s and softer spectra [80].

3

Atmospheric Muons and Neutrinos: a 4π Background

The major part of the background for neutrino telescopes as IceCube is represented by muons and neutrinos produced in the atmosphere. As the discrimination of signal from background is an important part for point source analyses, the production mechanism and analysis strategies for this background will be discussed briefly in this chapter.

3.1 Muons and Neutrinos from Cosmic Ray Air Showers

Atmospheric muons and neutrinos are abundantly produced in the Earth's atmosphere induced by a cosmic ray primary particle. When such a high energy cosmic ray hits the atmosphere and collides with one of its molecules, a shower of secondary particles is produced. This shower can be divided into three main parts: an electromagnetic, a hadronic and a muonic component, as shown in Fig. 3.1(a). The electromagnetic component consists only of electrons and photons. However, the hadronic part of the shower consists mainly of protons, neutrons, but also pions and kaons, which can decay into muons and muon neutrinos, forming the muonic component of the shower. Pions can decay into muons and neutrinos via the following mechanisms [27]:

$$
\begin{aligned}
\pi^+ \longrightarrow & \mu^+ + \nu_\mu & (99.9\%) \\
& \hookrightarrow e^+ + \nu_e + \bar{\nu}_\mu & \\
\pi^- \longrightarrow & \mu^- + \bar{\nu}_\mu & (99.9\%) \\
& \hookrightarrow e^- + \bar{\nu}_e + \nu_\mu &
\end{aligned}
\tag{3.1}
$$

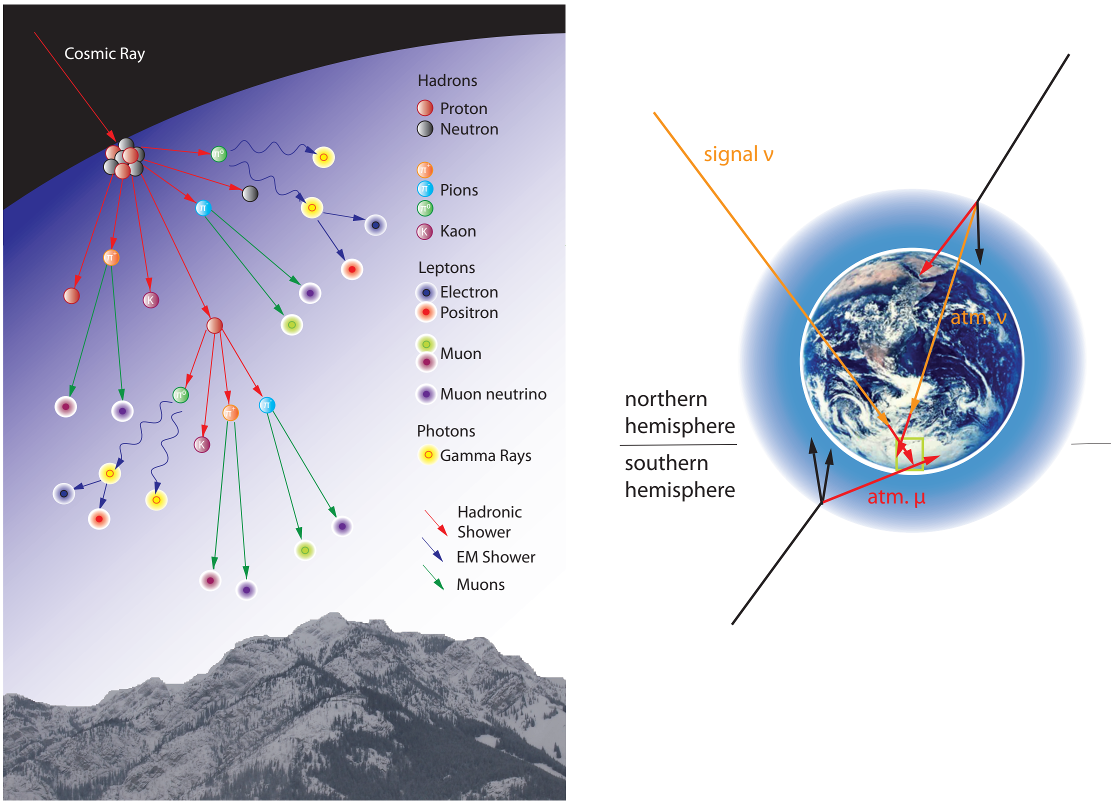

(a) Atmospheric Shower

(b) 4π Background

Figure 3.1.: (a) Illustration of an atmospheric shower induced by a high-energy cosmic ray primary. The shower can be divided into three components: a hadronic (red), electromagnetic (blue) and muonic (green) component. Adapted from [81]. (b) Sketch of the different background observed in IceCube for the two hemispheres. In the northern hemisphere atmospheric muons are shielded by the Earth and the dominant part in the background are atmospheric neutrinos. In the southern hemisphere however, both, atmospheric muons and neutrinos can reach the detector.

Both pion decays have a branching ratio of almost 100%. Each produced muon in this process can again decay into ν_μ. For kaons the most important decays producing muons and neutrinos are:

$$\begin{aligned} K^+ &\longrightarrow \mu^+ + \nu_\mu && (63\%) \\ K^- &\longrightarrow \mu^- + \bar{\nu}_\mu && (63\%) \\ K^+ &\longrightarrow \pi^0 + e^+ + \nu_e && (5\%) \end{aligned} \tag{3.2}$$

In this process the branching ratio into muons is $\sim$ 63%, while the decay into a π^0 has a ratio of $\sim$ 5%.

For IceCube the background reaching the detector is different for each hemisphere. In the northern hemisphere atmospheric muons are shielded by the Earth and the background consists mainly of atmospheric neutrinos from above, as they can not be shielded by the Earth. They reach the detector at a rate of$\sim 10^5$ events per year. For the southern hemisphere, the situation is even worse, since no shielding effects can be used and the complete flux of atmospheric muons and neutrinos hits the detector. The rate of atmospheric muons enlarges in the southern hemisphere to $\sim 10^{11}$ events per year. For dealing with the two types of backgrounds different strategies have been considered.

Muons are the dominant component of charged particles reaching the sea level, with a mean energy of $\langle E_0 \rangle \approx 4\,\mathrm{GeV}$ near the zenith. In order to suppress the muon background, neutrino telescopes are usually buried deep inside ice or on the bottom of the sea. Additionally, as mentioned above the Earth can shield parts of the sky from atmospheric muons and prevent them to reach the detector. For suppression of the atmospheric neutrino background in searches for astrophysical signal, cuts on the energy distributions can be made, since neutrinos produced in astrophysical objects are supposed to have higher energies than those produced in the atmosphere.

3.2 Atmospheric Neutrino Flux

Since atmospheric neutrinos penetrate through the Earth, their flux must be known precisely in order to establish suppression methods. Their flux is dependent on the production rate of pions and kaons in atmospheric showers. Up to energies of ϵ_π = 115 GeV and ϵ_K = 850 GeV, neutrinos resulting from muon decays are the most important contributors to the atmospheric flux. A muon of 1 GeV with a Lorentz factor $\gamma = E_\mu / m_\mu c^2 \sim$10 has a typical mean decay length of $d_\mu = \gamma \tau_\mu c \sim 6\,\mathrm{km}$. Since pions are usually produced in altitudes of 15 km and decay relatively fast, the daughter muons do not reach the sea level, but rather decay themselves or get absorbed in the atmosphere [82]. At higher energies the situation is different, as most muons reach the ground before decaying and therefore do not contribute to the neutrino flux anymore. Kaons become then the dominant source of atmospheric neutrinos for $E_\nu >$100 GeV [83, 84]. An illustration of the contributions of pions and kaons to the atmospheric muons and muon neutrinos depending on the energy is shown in Fig. 3.2.

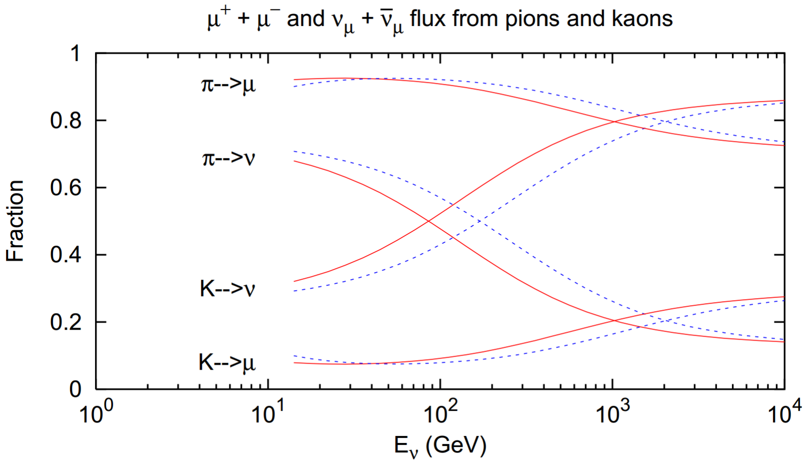

Figure 3.2.: Fractional contribution of pions and kaons to atmospheric muons and muon neutrinos. Solid lines are for vertical and dashed line for a zenith angle of 60° [85].

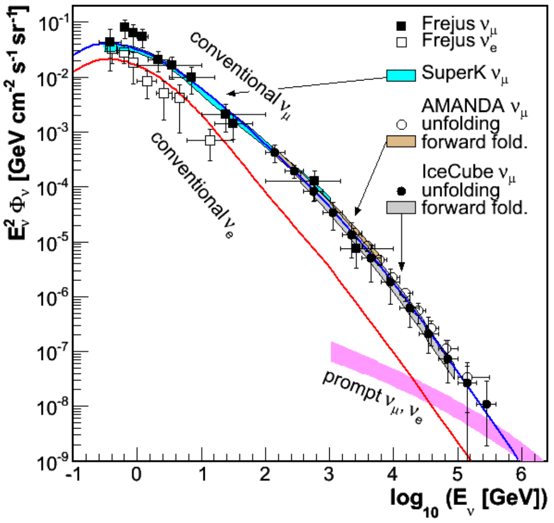

Figure 3.3.: Energy-dependent atmospheric neutrino flux measured in different experiments in comparison to the predicted flux of conventional atmospheric muon neutrinos in the Honda model [86]. Below 100 TeV the atmospheric neutrinos flux is dominated by the conventional flux, while above 100 TeV the prompt component in the neutrino flux becomes the dominant part [87].

As the lifetime of pions and kaons belongs to the order of 10^{-8}s they can lose energy in collisions prior to decaying, leading to less subsequent neutrinos. This steepens the primary cosmic ray spectrum of $E^{-2.7}$ to a spectrum of $E^{-3.7}$ for atmospheric neutrinos [88]. This flux is called conventional neutrino flux. Since for high energies, the decay length of pions and kaons becomes longer than their path lengths in the atmosphere [89], the production of neutrinos is supressed at high energies and the resulting flux is dependent on the energy. Additionally, the interaction depends on the temperature of the air. For higher temperatures, the air is less dense and therefore the interaction length gets longer. This is called seasonal variation in the atmospheric flux, resulting in a higher flux during summer and a lower flux during winter [90]. Figure 3.3 shows an overview of the energy dependent flux from atmospheric neutrinos for ν_μ and ν_e, measured by different experiments. It is compared to the predicted flux of conventional atmospheric muon neutrinos described in the Honda model [86]. In this model the neutrino flux for ν_μ and ν_e and their anti-particles can be estimated by

$$\frac{dN_\nu}{dE\nu} \simeq \Phi_0 \cdot E_\nu^{-\gamma} \left(\frac{A_{\pi\nu}}{1 + B_{\pi\nu} E_\nu cos(\theta^*)/\epsilon_\pi} + \frac{A_{K\nu}}{1 + B_{K\nu} E_\nu cos(\theta^*)/\epsilon_K} \right) \tag{3.3}$$

with the constant parameters $A_{\pi\nu}$, $B_{\pi\nu}$, $A_{K\nu}$, $B_{K\nu}$ including the components from pion and kaon decay and the inclination angle θ^* referring to the zenith angle θ of the neutrino measured in the detector corrected for the curvature of the Earth [91]. $\epsilon_\pi = 115$ GeV and $\epsilon_K = 850$ GeV are the critical energies at which the interaction probability in the atmosphere equals the decay probability.

For high energies another component is anticipated, called prompt flux. This flux is assumed to be generated by the immediate decay of heavy mesons, especially those containing a charm quark, such as D^0 or D^+. Since their masses start at a few GeV, their production in air showers needs higher primary particle energies than the production of pions and kaons. As the prompt meson decays immediately, it has in approximation the same energy spectrum as the primary cosmic rays of $E^{-2.7}$. The cross-over between conventional and prompt dominated fluxes occurs at energies of 100 - 1000 TeV [92]. Such a prompt atmospheric flux has not yet been measured experimentally and still contains large uncertainties.

The flavour ratio for conventional atmospheric neutrinos beyond TeV energies is approximately $\nu_e : \nu_\mu : \nu_\tau = 1 : 20 : 0$, while the ratio for prompt atmospheric neutrino is at $\nu_e : \nu_\mu : \nu_\tau = 1 : 1 : 0.1$. Such flavour ratios differ significantly from those of astrophysical neutrinos which arrive on Earth with $\nu_\mu \approx \nu_\tau$ [93].

4

The IceCube Neutrino Observatory

The first ideas of high energy neutrino detection date back up to the 50s. In 1960, Markov [94] published his idea to install detectors deep in a lake or a sea to determine the direction of charged particles with the help of Cherenkov radiation. It took until 1965 until atmospheric neutrinos were detected for the first time, almost simultaneously by two groups, both using old gold mines. In the eighties a phalanx of new detectors emerged, like the Baksan Neutrino Telescope (BNT) in the Caucasus or Kamiokande in Japan. However, for the detection of extra-terrestrial neutrinos large-scale experiments were needed. By using Markovs idea of underwater detection, the Deep Underwater Muon and Neutrino Detection (DUMAND) project took shape in constructing prototype strings of photomultipliers in the pacific ocean off the shore of Hawaii in a depth of 5 km [95]. Due to technical difficulties the project got cancelled, but led way to the idea of using the Antarctic ice sheet as detector material [96]. This resulted in first experiments at the South Pole in 1991 leading to Icecube's predecessor, the Antarctic Muon and Neutrino Detector Array (AMANDA) in 1997 [97]. The first AMANDA array with 4 strings and 80 optical modules was upgraded stepwise until January 2000 19 strings with a total of 667 optical modules were deployed in a depth of 1.5 to 2 km. Other experiments starting at that time are the Baikal detector in lake Baikal in Siberia and the Astronomy with a Neutrino Telescope and Abyss environmental RESearch project (ANTARES) in the Mediterranean sea, which are both still on-going [98]. Although photons in water are less scattered than in ice, using the clear and compressed ice at the South Pole in a depth of 1.5 to 2.5 km has several advantages, such as the long mean absorption length of photons, the lack of radioactivity and the drilling on solid surface.

As AMANDA proved to be working well, plans for an even bigger detector arose and resulted in the first deployment of IceCube-strings in 2004.

In this chapter first the principles of neutrino detection will be discussed and a description of the IceCube detector will be given. The last part contains the characterization of the Antarctic ice.

4.1 Principles of Neutrino Detection

Neutrinos are affected only by the weak force and therefore hard to measure with the need of large detector volumes or long exposure times. There are two main processes in which neutrinos can interact with nucleons:

- charged current (CC) interactions involving a $W^{\pm}$ boson: $\nu_\ell + N \longrightarrow \ell^- +$ hadronic shower
- neutral current (NC) interactions involving a Z boson: $\nu_\ell + N \longrightarrow \nu_\ell^{'} +$ hadronic shower

with ℓ being the lepton flavour (muon, electron or tau) and N a nucleon.

Neutrino Cross-Sections

The cross sections of CC and NC-interactions can be evaluated as described in [99]. The differential cross section for charged current interactions is given by

$$\frac{d^2\sigma}{dxdy} = \frac{2G_F^2 M E_\nu}{\pi} \left(\frac{M_W^2}{Q^2 + M_W^2}\right) \left[xq(x,Q^2) + x\bar{q}(x,Q^2)(1-y)^2\right] \tag{4.1}$$

with the Bjorken scaling variable $x = Q^2/2M_\nu$ and $y = \nu/E_\nu$, the invariant momentum transfer between incident neutrino and outgoing muon $-Q^2$, the energy loss in the target frame $\nu = E_\nu - E_\mu$, the nucleon and W-boson masses M and M_W and the Fermi constant $G_F = 1.16632 \cdot 10^{-5} GeV^{-2}$. The quark distribution functions can be written by

$$q(x,Q^2) = \frac{u_v(x,Q^2) + d_v(x,Q^2)}{2} + \frac{u_s(x,Q^2) + d_s(x,Q^2)}{2} + s_s(x,Q^2) + b_s(x,Q^2) \tag{4.2}$$

and

$$\bar{q}(x,Q^2) = \frac{u_s(x,Q^2) + d_s(x,Q^2)}{2} + c_s(x,Q^2) + t_s(x,Q^2) \tag{4.3}$$

with the quark flavours u, d, c, s, t, b with the label v and s for valence and sea quarks. In Figure 4.1(a) the neutrino and anti-neutrino cross sections for both interactions are shown as a function of the energy. In general, the CC cross sections are larger than the NC cross section. At low energies all cross-sections scale linearly with the energy, while at energies above 10^4 GeV the cross section is reduced due to the W-boson propagator. Also, the cross section for ν and $\bar{\nu}$ differ at low energies, while they become

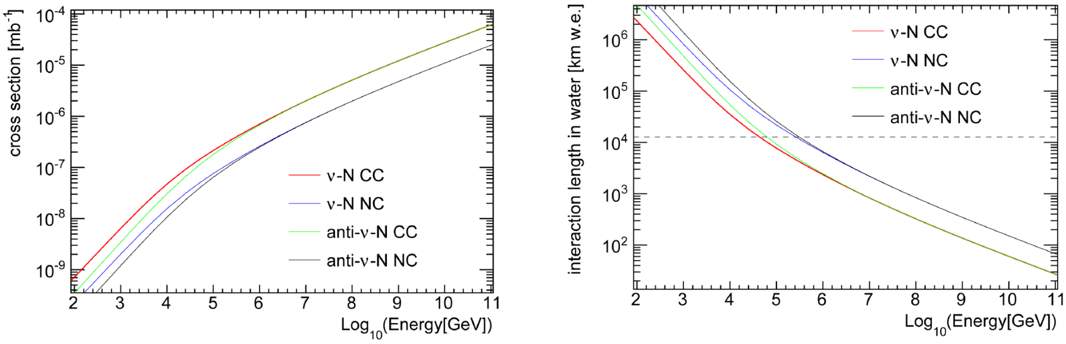

(a) Neutrino cross section (b) Neutrino Interaction Length

Figure 4.1.: (a) Neutrino and Anti-Neutrino cross sections for CC and NC-interactions as a function of the energy. (b) Neutrino and Anti-Neutrino Interaction Length in water (water equivalent w.e.) as a function of the energy. The Earth's diameter is shown as a dashed line. Plots from [101, 102]

equal for high energies, as the valence quark contribution becomes negligible. As the cross sections of interactions of ν and electron are usually too low to be considered, a resonant behaviour of $\bar{\nu}_e e^- \rightarrow W^-$ can be observed at energies of $\sim 6.3\,\mathrm{PeV}$. This peak is called Glashow resonance [100] and can reach values two orders of magnitude above the NC-cross section. Fig. 4.1(b) shows the interaction length of neutrinos and anti-neutrinos in water, which can be described by

$$L_{int} = \frac{1}{\sigma_{\nu N}(E_\nu) N_A} \tag{4.4}$$

with N_A being the Avogadro constant $6,022 \cdot 10^{23}\mathrm{mol}^{-1}$ (water equivalent w.e.). At energies above $\sim$ 100 TeV the interaction length becomes smaller than the Earth's diameter, meaning that the Earth turns opaque only for high energy neutrinos. This can be used in the background rejection of neutrino experiments, since muons produced in the atmosphere can not traverse the Earth.

For detecting the products of these interactions several methods can be used. For high energetic neutrinos optical methods are combined with large volumes of transparent media like water or ice. High energetic charged leptons from these interaction can then radiate Cherenkov light which can be detected by the optical modules of the detector.

Cherenkov Radiation

Cherenkov radiation is emitted if a charged particle moves through a dielectric medium at a speed greater than the speed of light in that medium [103]. The idea of using this radiation for the detection of particles was first described in [104].

If a charged particle is moving relatively slowly through a transparent medium the electric field of the particle distorts the atoms in building up a polarization field. Owing

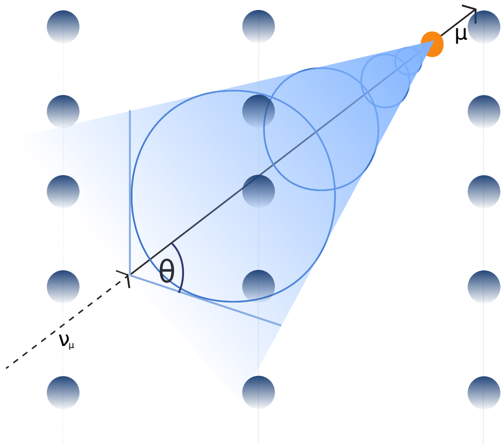

Figure 4.2.: Sketch of a muon propagating through the IceCube detector, showing the resulting Cherenkov cone.

to the complete symmetry of the polarization field surrounding the particle, there will be no resultant field at large distances and therefore no radiation. If however the particle is moving with a speed that is comparable to the speed of light in the medium, the polarization field is no longer completely symmetrical. This results in a dipole field along the axis of the particle and will momentarily excite the electrons of the atoms along the track inside the medium, which then return to their normal state by emitting photons. However, if the velocity is faster than the speed of light in that medium, the photon waves emitted along the track can be in phase, so that there is now a resultant field. This can be expressed in the so-called Cherenkov threshold

$$\beta \geq 1/n(\lambda) \tag{4.5}$$

with $n(\lambda)$ being the phase velocity refractive index in the medium. Since the photons are moving slower than the charged particle the photons form a cone forward the region where the interaction took place, called Cherenkov cone, see Figure 4.2. The angle of the Cherenkov cone θ is correlated with the velocity of the charged particle $v = \beta c$ and the speed of light in the medium $c^{'} = c/n(\lambda)$ and the refractive index in the medium $n(\lambda)$, resulting in:

$$cos(\theta) = \frac{c^{'}}{v} = \frac{1}{\beta n(\lambda)} \tag{4.6}$$

For relativistic muons in ice ($n(\lambda) \sim 1.32$ at 400 nm), $\beta \sim 1$ can be assumed and the angle θ is fixed at 40.75°. The number of photons emitted by a charged particle per unit path length and per wavelength λ of the photons is equal to

$$\frac{d^2 N_\gamma}{dx d\lambda} = \frac{2\pi\alpha}{\lambda^2}\left(1 - \frac{1}{\beta^2 n(\lambda)^2}\right) \tag{4.7}$$

with α being the fine-structure constant $\sim 1/137$. The number of photons is then inversely proportional to the wavelength and the spectrum peaks in the UV-region.
With these preliminary consideration of the detection of neutrinos, the design of an optical neutrino telescope requires large transparent material like water or ice, instrumented with several optical sensors. The instrumented volume needs to be deep underground to suppress the main background of atmospheric muons, but still accessible to maintaining work. The biggest of the currently operating neutrino telescopes is the IceCube detector deployed inside the Antarctic ice.

4.2 Design of the IceCube Detector

The IceCube detector located at the geographic South Pole is buried deep inside the Antarctic ice and is with an instrumented volume of $1\,\mathrm{km}^3$ the biggest neutrino detector. The detector uses the 2800 m-thick polar ice sheet to provide a target, an optically clear radiator, and a stable instrument deployment platform [12]. It consists of three main components: an in-ice array, an additional air shower array on the surface, called IceTop, and a denser instrumented region in the center, called DeepCore [105]. The in-ice detector consists of Digital Optical Modules (DOMs), placed on strings deployed vertically in depths between 1450 m and 2450 m. The strings hold 60 DOMs each equipped with a photomultiplier tube (PMT) and digitizing electronics to detect neutrinos by measuring Cherenkov radiation of their secondary particles [13]. The detector was built in several stages between 2005 and 2010, such that each year several strings were added, until reaching the final configuration of 86-strings, containing more than 5160 DOMs. For the deployment of a string a hole is drilled into the ice, using a hot-water jet. Then the string with the attached DOMs is deployed. After the installation of the DOMs the water freezes again and the DOMs become inaccessible for maintenance work. The distance between two adjacent DOMs is 17 m on the strings, which are arranged on a grid with a hexagonal alignment with a 125 m inter-string distance.
In the center of the grid additional eight strings with a smaller spacing are installed, building a dense instrumented volume called DeepCore. DeepCore lowers the energy threshold of IceCube from around 100 Gev to 10 GeV and is dedicated to low-energy analyses below 1 TeV.
The IceTop component consists of 81 surface stations, each of which is a pair of tanks separated by 10 m. Each tank is instrumented with two DOMs frozen in the upper side of the 2.7 m diameter ice-filled tank, which gives a total number of 324 sensors. Although the goals of IceTop are mainly measurements of the primary cosmic ray spectrum and their composition, it can also veto high energetic air showers which are considered as background in the neutrino telescope [106].

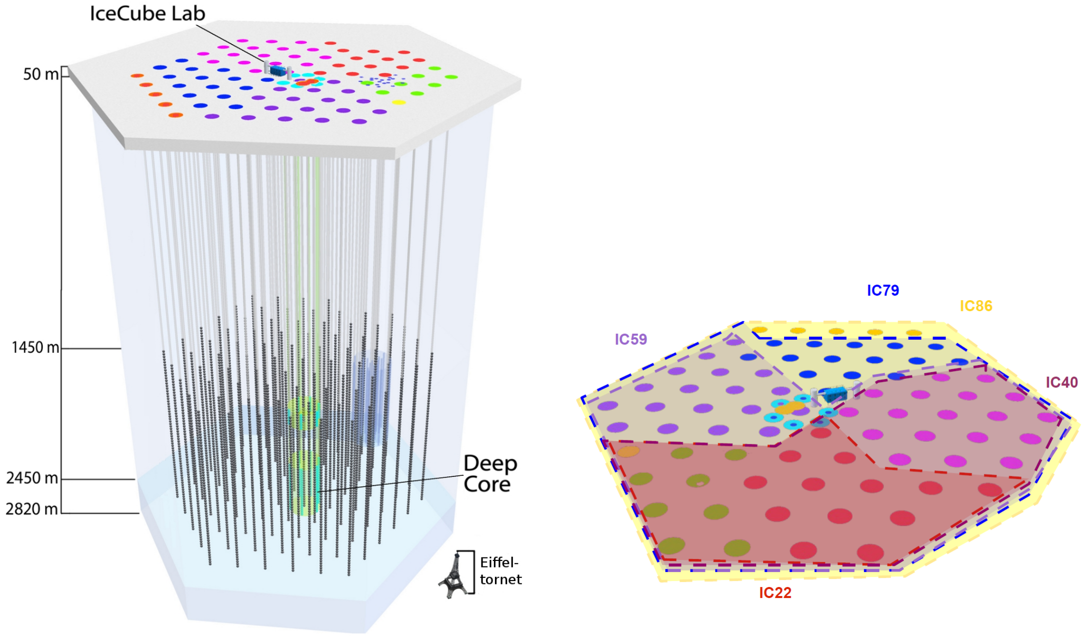

(a) IceCube Detector (b) IceCube configurations

Figure 4.3.: (a) Schematic view of the IceCube detector, including the DeepCore strings. (b) IceCube configurations used in this work, going from the 40-used string configuration (IC40) to the final 86-string configuration (IC86)

Figure 4.3(a) shows a schematic view of the IceCube detector including the DeepCore strings. Figure 4.3(b) illustrates the different stages of construction. In this work, data from the 40-string configuration (IC40) to the final 86-string configuration (IC86) is used, see Sec. 5.1.6 for details.

4.2.1 Digital Optical Modules (DOMs)

One of the most fundamental elements of the IceCube array are the DOMs. The main task of the DOMs is to collect the blue and near UV Cherenkov light emitted by relativistic charged leptons passing the IceCube array. In Fig. 4.4(a) a schematic view of a DOM [12] is shown. The IceCube DOMs consist of a downwards-facing HAMAMATSU R7081-02 PMTs build in a 33 cm diameter borosilicate glass sphere, with a thickness of 13 mm. The majority of the DeepCore DOMs however use a newer PMT model, R7081MOD, with a higher quantum efficiency. Additionally, the glass sphere is inlayed with a μ-metal grid to shield the Earth's magnetic field. The IceCube PMT works with 10 dynodes, leading to a gain of $\sim 10^7$ in which the high voltage of 1300V-1500V is provided by a Cockroft-Walton power supply. The PMT has a standard 10 in diameter bi-alkali photocathode with a maximum quantum efficiency of 25 % at a wavelength of 390nm [107]. This wavelength matches reasonably well the Cherenkov spectrum in ice and the cutoff at wavelenghts of 350 nm caused by the glass sphere.

Other components are a LED flasher board, used for calibration and measurements of the ice properties, a high voltage divider and the DOM mainboard. A block diagram of the DOM mainboard is shown in Fig. 4.4(b).

The principal function of the DOM is to produce a digital output, called 'hit' whenever one or more photons are detected. A hit always contains at least a timestamp and a measure of charge. These elements can be read out from the shape of a waveform. If a PMT gets hit, these waveforms immediately get digitized by two different digitizers, called Analog Transient Waveform Digitizers (ATWDs) and Fast Analog to Digital Converters (FADCs), installed on the DOMs main board. The signal is processed by the digitizers only, if the discriminator threshold of 0.25 times the single photoelectron peak (∼8mV) is passed [13]. The waveform signal for the digitizers (FADCs, ATWDs) is delayed by 75 ns. By this it is ensured that the discriminator signal arrives early enough, that the entire waveform can be digitized. The ATWD captures pulses in a small time window with high temporal resolution (128 bins of 3.3 ns covering 422 ns), while the FADC uses coarser binning but a longer time interval(256 bins of 25 ns covering 6400 ns). Additionally, each ATWD has three channels, with different amplifications (0.25x, 2x, 16x) of the PMT signal, providing a dynamic range, as the slower channels are only read-out if the faster saturates.

In converting each pulse into digital format individually inside each DOM the quality of the signal is preserved and no data gets lost. The entire waveform is transmitted to the surface only, if one of the four neighbouring DOMs on the same string are hit within a time window of usually less than 1 μs. These condition is called Hard Local Coincidence (HLC). If the condition is not fulfilled and the hits are isolated they are called Soft Local Coincidences (SLC) and only the three sample points from the fADC with the highest charge.

After digitization the signal is sent to the DOMHub, a computer communicating with all DOMs on one string and then further to the computers of the surface data acquisition system (DAQ).

4.2.2 DAQ and Filtering

The DAQ is located in the IceCube Laboratory (ICL) on the surface of the IceCube detector. Since the raw data collected by the IceCube detector exceeds the daily satellite bandwidth (30 GB/day), the first level of reconstruction and filtering happens real-time, coordinated by the DAQ. A first step here is the reduction of pure noise via local coincidence conditions, as described above. SLC hits are mainly needed to improve the reconstruction of cascades and low energy muon tracks, but are also crucial to any veto technique against atmospheric muons. This is true only for SLC hits of physics origin, but most SLC hits recorded are due to dark noise. Therefore an effective cleaning is necessary. A module for the reduction of noise is the SeededRT Cleaning [108]. It requires a coincident SLC hit in a certain radius (R=150 m) and time (T=1000 ns) around each HLC hit, everything else is treated as noise. One of the most important triggers in this context is the Simple Multiplicity Trigger (SMT). It

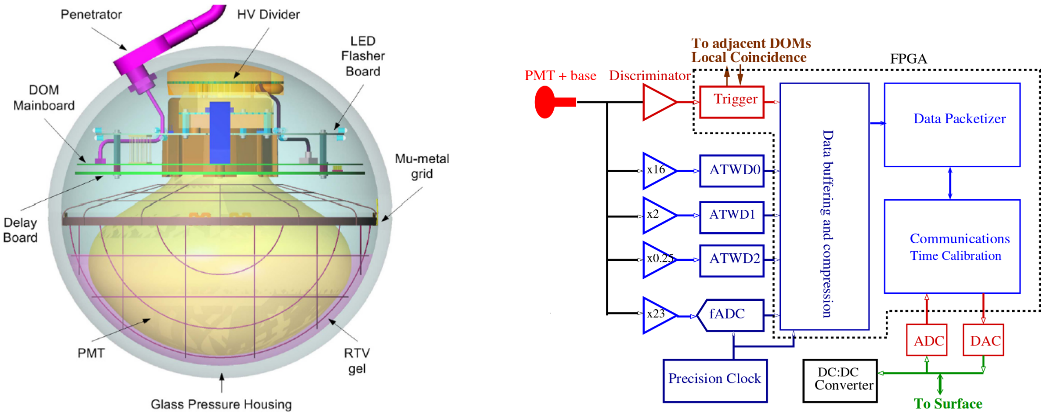

(a) IceCube DOM (b) Block diagram of the DOM mainboard

Figure 4.4.: (a) Schematic view of the DOM with the different components (b) Block diagram of the IceCube main board electronics [107]

requires minimum eight DOMs hit within a time window of 5 μs. Other triggers in IceCube are operating, but are not used in context of this work. All triggers use HLC hits only.

Filters

The Online Processing and Filtering system is responsible for accepting raw, triggered events from the DAQ. For further reduction of the data rate to be sent via satellite, it gets processed "online", meaning that several filters are applied. One of the most essential of these filters for point source analyses is the muon filter. It selects track-like events that were produced by muons in separating the signal from the background events coming from cosmic ray air showers in the northern hemisphere and muon bundles in the southern hemispheres, see Sec. 5.1.2. Additionally, a cut on the quality parameters of the reconstructed track is done. Another filter used is the Extreme High Energies (EHE) filter, which selects events based on their amount of total charge. All events passing the online filters are transferred north for further off-line analyses. Furthermore, raw data is stored on magnetic tape and transported North during the austral summer.

4.3 The Antarctic Ice

The ice at the South Pole has a very high transparency and is the most transparent solid medium known at wavelengths of 200-400 nm, see [109]. The Antarctic ice is characterized by it's absorption and scattering length, as function of depth and wavelength. However, the scattering length of photons can be short, due to trapped air bubbles or dust in the ice, which both depend on the depth of the ice. Air bubbles are mainly concentrated in depths above 1400 m or in newly freezed bore-holes. Depending on the depth, the pressure rises and the air bubbles get compressed and convert into air-hydrate crystals with a refractive index very close to the ice itself. Both, the dust and the air bubbles effect largely the prediction of propagating Cherenkov photons in the ice and the numbers hitting a DOM can be over- or underestimated. Therefore a better understanding of the optical properties of the ice and its structure is crucial for the simulation and reconstruction algorithms.

The two most important processes in this context are the scattering and the absorption of the ice.

4.3.1 Scattering

Scattering of photons occurs if small air bubbles or dust grains are spread in the ice. It can be described by the scattering length λ_s and the average scattering angle $\langle\cos(\theta)\rangle$. Mainly, the scattering happens in forward direction with $\langle\cos(\theta)\rangle{>}0$. Since most of the photons scatter several times, it is convenient to define an effective scattering length λ_e [110], given by

$$\lambda_e = \frac{\lambda_s}{1 - \langle\cos(\theta)\rangle}. \tag{4.8}$$

It describes the distance after which the scattered direction has been fully randomized. The average scattering angle for dust lies at $\langle\cos(\theta)\rangle{>}0.94$. Usually, the effective scattering length is expressed via the effective scattering coefficient $b_e = 1/\lambda_e$.

4.3.2 Absorption

The absorption length λ_a is defined in a similar way as the distance at which the survival probability of a photon drops to 1/e. It is usually expressed by the absorption coefficient $a = 1/\lambda_a$.

For the determination of the ice parameters, dedicated measurements are performed using LED flashers integrated inside each DOM [111]. They emit short light pulses which are measured by the surrounding DOMs. The results of flasher measurements between 1400 m and 2400 m depth are illustrated in Fig. 4.5(a) and Fig. 4.5(b). The values of the absorption coefficient a(400nm) and effective scattering coefficient b_e(400nm), which are the inverse of the effective scattering and absorption length, respectively, are shown. The most prominent feature in both figures is the dust layer between 1950 m and 2100 m depth, due to geological and atmospheric conditions in history. The absorption length is here only ∼20 m and the effective scattering at ∼5 m. Apart from this, three smaller dust layers between 1500 m and 1900 m are visible. In these regions the absorption and scattering of photons is much higher and signal is less visible. The clearest ice is found in depths of 2200 m to 2500 m, in which the DeepCore strings are installed. There, the absorption length reaches values of uo to 250 m and the effective scattering of up to 100 m. An alternative model shown is the Additionally Heterogeneous Absorption model (AHA) [109], which is providing a similar structure but has

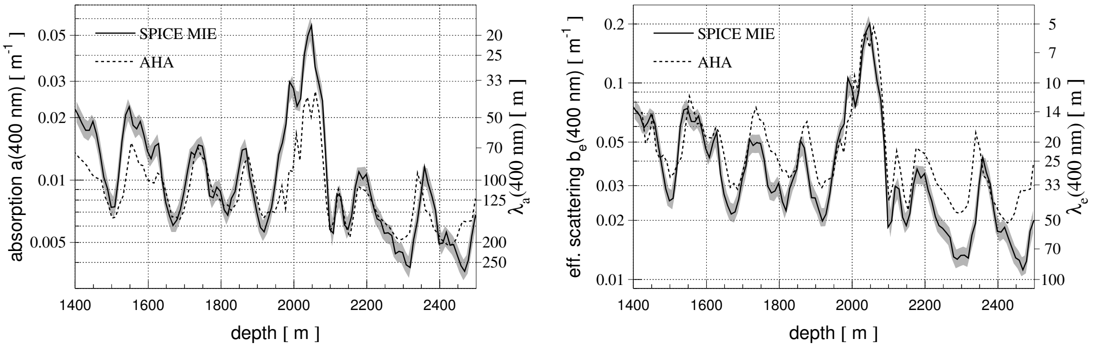

(a) Absorption coefficient a (b) effective scattering coefficient b_e

Figure 4.5.: (a) Values of the absorption coefficient $a(400\text{nm})$ and effective scattering coefficient $b_e(400\text{nm})$ (b) vs. depth for a converged solution (solid line). The grey bands show the $\pm 1\sigma$ range of combined systematic and statistical uncertainty. The updated model of the Additionally Heterogeneous Absorption model (AHA) [109] is shown with a dashed line [111].

higher variations in the coefficients.

Additionally, data from ice core measurements and using laser dust loggers inside the boreholes during detector commissioning between 2004 and 2010 can be used [112]. It was shown that the age of the ice varies between 25,000 years around 1400m depth and 100,000 years around 2800 m depth, where the bedrock starts [113]. From radar measurements a temperature profile of the ice can be estimated and varies from -50°C at the surface to -9°C at the bedrock [114].

5

Data Sample and Statistical Methods from Point Source Searches

In the first part of this chapter the event selection process with the reconstruction methods will be described and the used data samples will be outlined. In a second part, the statistical methods used in point source searches and the methods used in the three analyses will be presented.

5.1 Data Sample and Reconstruction Algorithms

The event selection in IceCube is a complicated process and is usually done for each analysis separately. For point source analyses however, a joint data sample is produced on which different analyses are performed. In this section, the standard reconstruction algorithms, used in almost all analyses and the most important steps in the creation of a specific point source data sample are presented. As a first step in the event selection it has to be decided which event topologies will be used. In IceCube different interactions leave different signatures in the detector, which have to be considered in the next steps.

5.1.1 Signatures in IceCube

As discussed in Sec. 4.1 neutrinos can interact via charged and neutral current interactions. CC-interactions produce a charged lepton depending on the flavour of the interacting neutrino, which carries an average of 50 % (at GeV energies) to 80% (at high energies) of the neutrino energy [115]. The remaining residue is transferred into a hadronic shower. The ν_μ CC event signature differs strongly for all other cases. Therefore, different interactions leave different signatures in the IceCube detector, as

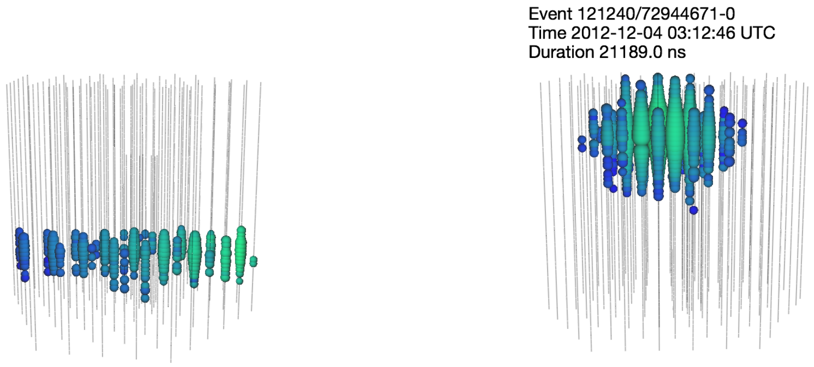

(a) Track

(b) Cascade

Figure 5.1.: (a) Track-like signature in IceCube from simulation. Shown is a 130 TeV muon produced in CC interactions. (b) Example for a cascade signature from data observed in [15].

shown in Figure 5.1. There are two basic topologies: tracks coming from ν_μ (left) and cascades from ν_e and ν_τ (right).

Muon Neutrinos (ν_μ)

In case of a muon neutrino a muon is produced, which has a great penetrating power with up to 10 km long tracks at PeV energies. They travel much further than the detector scale and can therefore enlarge the effective volume of the detector by observing also muons from far outside the detector. Since they leave a track-like signature, the angular resolution for the muon direction (and thus, the neutrino direction) lies below 1° for high energies and makes them suitable for point-source studies. Disadvantages are that the events are not contained and it is therefore difficult to determine the neutrino energy.

Electron Neutrinos (ν_e)

Cascades in this context are, compared to the detector's extension, almost point-like. In case of ν_e an electron is produced, which is heavily affected by bremsstrahlung. Only 0.5% to 0.8% of its energy are deposited into an electromagnetic shower with a typical length of a few meters, while the rest transfers into a hadronic cascade. Since the shower is not totally symmetric, but elongated into the direction of the leading electron, the direction of the incident neutrino can be reconstructed [116]. Since the events are contained the energy reconstruction is superior, using largely a calorimetric measurement where the cascade energy scales nearly linearly with the light output.

Tau Neutrinos (ν_τ)

For ν_τ, which have the great advantage that they are not absorbed by the earth, in CC interactions a τ with a mass of 1777 MeV gets produced. The generated τ has a lifetime of only 0.29 ps and decays with a main branching ratio of 64.8 % gain into a ν_τ: $\tau \longrightarrow \nu_\tau + X$ [27]. Whereas at low energies the showers are not distinguishable from the ones initiated by a ν_e, at high energies (>2 PeV) they produce a specific signature, called 'double bang', caused by the first hadronic shower from the initial interaction and a second shower induced by the τ decay. However, in the atmospheric neutrino flux no high energy ν_τ are expected and there is no evidence yet for a detection of a ν_τ with IceCube.

In this work data-samples dominated by muon tracks, induced by a ν_μ are used. However, ν_e or ν_τ which are misidentified as track-like could also contribute to the samples. Cascade events are not suitable for point source studies due to their poor angular resolution, but can still be used for the triggering of point-source studies. Different reconstruction methods are used in order to suppress the atmospheric background and to produce a final data sample used for point source analyses. These reconstruction methods and the final data samples will be presented in the next sections.

5.1.2 Angular Reconstruction

As discussed in Sec. 5.1.1 muons coming from a muon neutrino are characterized as a track inside the detector. The interaction angle Ψ between the muon neutrino and the emerging muon can be described by

$$\Psi = 0.7^\circ \cdot (E_\nu/\mathrm{TeV})^{-0.7} \tag{5.1}$$

and decreases with energy [117]. At high energies, the direction of the muon can be very well approximated with the direction of the incident neutrino, which makes neutrino astronomy possible.

The muon track reconstruction algorithm is a maximum likelihood procedure. Prior to this sophisticated reconstruction, simple pattern recognition algorithms are used to generate the initial estimates that are required by the maximum likelihood reconstructions to start the minimization of the negative likelihood -log($\mathcal{L}$). This initial track is derived from first guess methods, which are fast analytic algorithms that do not require an initial track [118]. The most important first-guess algorithm is the LineFit.

LineFit

The LineFit algorithm uses the hit times of an initial track with an optional amplitude weight. The geometry of the cherenkov cone and the optical properties of the ice are ignored. It assumes light travelling with a constant velocity v at a straight path through the detector. The magnitude of the LineFit is the mean speed of the light propagating through the detector and can be used to distinguish between minimally

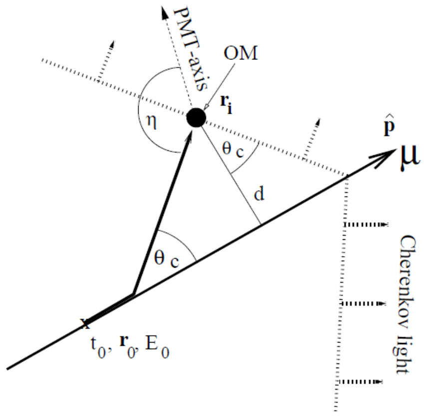

Figure 5.2.: Cherenkov light front of a muon with the different variables used to calculate t_{geo} [118]

ionizing muon tracks, which have large values and spherical events (cascades) or high energy muons, which have low values.

Maximum Likelihood Reconstructions

After seeding with a first-guess algorithm, the more refined maximum likelihood method is applied. The parameters varied in the maximization are described by the track parameters $a = r_0, t_0, \mathbf{p}, E_0$ with r_0 as an arbitrary point on the track, which passes at time t_0 with energy E_0 along a direction $\mathbf{p}$. Given a set of experimentally measured values $x = x_i$ this reduces to

$$\mathcal{L} = (x \mid a) = \prod P_i^{N_{hits}}(x_i \mid a) \tag{5.2}$$

where $P(x_i \mid a)$ is the probability density function of observing the measured value x_i for given values of the parameters a [118]. The reconstruction is performed by minimizing -log($\mathcal{L}$) with respect to a. Taking only the time information each DOM was triggered t_i and the DOM's position r_i into account, we can calculate from simple geometry the time at which photons are expected to hit the DOM, t_{geo}, see Figure 5.2. This results in a time residual between the expected time t_{geo} without any scattering and the actual time the DOM gets hit t_{hit}

$$t_{res} = t_{hit} - t_{geo}\,. \tag{5.3}$$

The distribution of the time residuals can be approximated analytically by the Pandel function [119], a parametrization giving the delay probabilities in photon arrival times. It can be expressed as

$$\mathcal{P}(\rho, \xi, t) = \frac{\rho^{\xi} t^{\xi-1}}{\Gamma(\xi)} e^{-\rho t} \tag{5.4}$$

with ρ and ξ being phenomenological parameters depending on the properties of the medium and the distance between the track and the DOM. Since photons arriving with only a few ns difference can not be distinguished by the PMT, the first photon, which is usually less scattered than a single photon, defines the arrival time. If only the first measured photon is used for the reconstruction, the likelihood is called Single Photon Electron (SPE) likelihood. If the presence of additional pulses is taken into account it is called Multi Photon Electron (MPE) likelihood and the probability density function (pdf) can be written as

$$p_N^1(t_{res}) = N \cdot p_1(t_{res}) \cdot \left(\int_{t_{res}}^{\infty} \cdot p_1(t) dt \right)^{N-1} \tag{5.5}$$

In the analyses presented in this work MPE will be the standard angular reconstruction.

SplineMPE

Although the Pandel function includes the effect of scattering it does not account for details like different ice layers and the angular sensitivity of the DOMs. Therefore, a more realistic likelihood model was developed during the processing of the IC86 data sample (see Sec. 5.1.6) and is called SplineMPE [120]. The SplineMPE uses Monte-Carlo based tables [110] of simulated photons propagated through the ice. In order to get a continuous distribution, cumulative discrete distributions are interpolated with splines, which are based on the piecewise polynomial interpolation of infinite muon tracks. Fitting Splines to photonic tables allows to include information about the ice layers and the angular sensitivity of the DOMs also in the MPE reconstruction and is used in the multi point source study and the self-triggered flare search, see Sec. 7 and Sec. 8. Figure 5.3 shows the median angular resolution as a function of energy for the IC79 sample using different reconstruction methods. The SplineMPE yields an improvement at all energies, reaching a median angular resolution of 0.4° at the highest energies.

Paraboloid Sigma

For obtaining the angular uncertainty of the likelihood fit a method called paraboloid sigma is used. It fits the likelihood space around the reconstructed track minimum with a paraboloid with giving the values σ_x and σ_y for the major and minor axes x and y of the event error ellipse [121]. With $\sigma = \sqrt{(\sigma_x^2 + \sigma_y^2)/2}$ the resulting value of paraboloid sigma σ gives the final uncertainty for each event. However, paraboloid estimates on average too good angular resolutions for high energies. This is presumably related to inaccuracies of the likelihood used in the reconstruction. This effect is mitigated by a rescaling of paraboloid sigma as a function of energy.

5.1.3 Energy Estimation

Each particle travelling trough matter has a characteristic energy loss induced by three different processes: ionization, bremsstrahlung and photo-nuclear reactions. Between

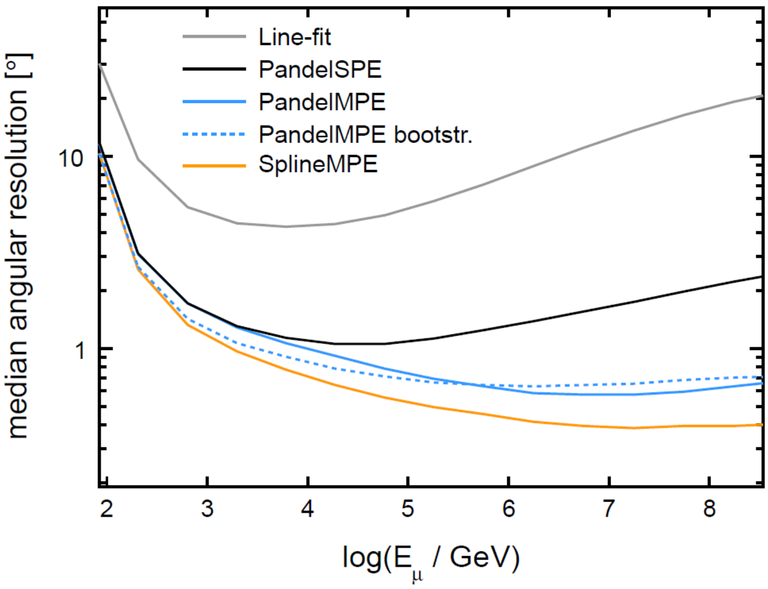

Figure 5.3.: Median angular resolution as a function of energy for the IC79 sample using different reconstruction methods [101]. The LineFit as a first-guess algorithm is the starting point for more sophisticated reconstructions with the SPlineMPE yielding the best angular resolution.

10 MeV and 100 GeV ionization is the dominant process and can be described as the mean rate of energy loss -$\langle dE/dx\rangle$ (stopping power) by the Bethe-Bloch formula [27]

$$-\left\langle \frac{dE}{dx} \right\rangle = Kz^2 \frac{Z}{A}\frac{1}{\beta^2}\left[\frac{1}{2}\ln\frac{2m_ec^2\beta^2\gamma^2T_{max}}{I^2} - \beta^2 - \frac{\delta(\beta\gamma)}{2}\right] \tag{5.6}$$

Here, K is a constant factor, Z the atomic number, A the mass number of the material and T_{max} the maximum kinetic energy which can be imparted to a free electron in a single collision. I is the mean excitation energy in eV and $\delta(\beta\gamma)$ the density effect correction term to the ionization energy loss. At higher energies radiative processes become more important, for muons this 'critical energy' lies at a few hundred GeV. These processes can hardly be described as uniform, since they suffer small cross-sections and large energy fluctuations. It is conveniently to write the average rate of the muon energy loss as

$$-\frac{dE}{dx} = a(E) + b(E)\cdot E \tag{5.7}$$

with a(E) the ionization power described by equation 5.6 and b(E) the sum of e^+e^- pair production, bremsstrahlung, and photonuclear contributions. The energy loss due to Cherenkov radiation lies around $\sim 0.1\,\mathrm{MeVm^{-1}}$ and is thus negligible compared to the other contributions.

In IceCube different algorithms for the determination of the energy loss are used. For point source studies those are favourable, which are based on the energy loss

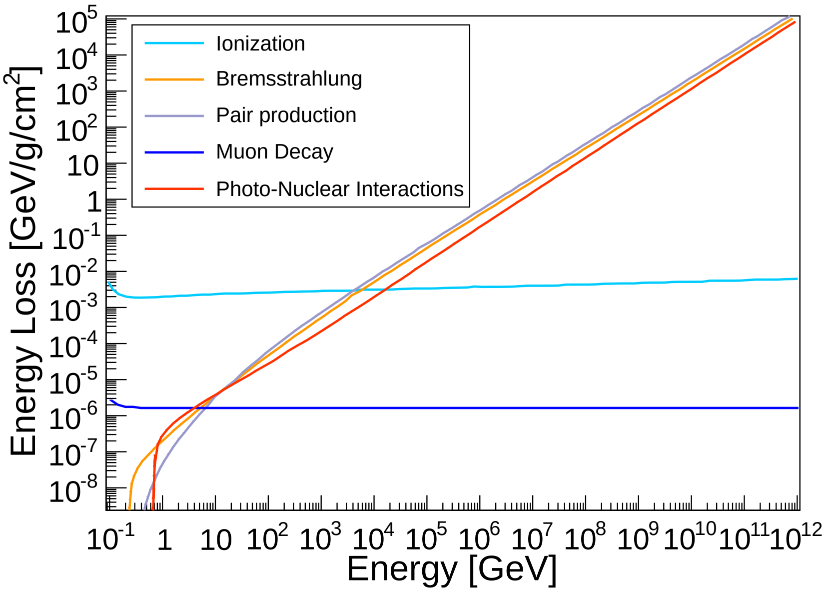

Figure 5.4.: Energy loss of muons in ice showing the contributions of ionization, bremsstrahlung, pair production, muon decay and photo-nuclear interactions. Above a few 100 GeV bremsstrahlung, pair production and photo-nuclear interactions become the dominating processes, scaling linearly with the muon energy.

along the muon track, instead of the calorimetric approach of a cascade. As can be seen in Figure 5.4, the dominating energy loss from bremsstrahlung, pair production and photo-nuclear interactions, increases linearly with the muon energy above a few 100 GeV. One algorithm here is called MuE [122].

MuE

MuE is based on the reconstruction of the number of photons per unit length along the muon track using a maximum likelihood approach and taking into account the absorption and scattering in the ice, assuming a bulk ice model [123]. This total number of photons per unit length can be described with

$$N_c = 3 \cdot 10^4 \mathrm{m}^{-1} (1.22 + 1.36 \cdot 10^{-3} \frac{E}{\mathrm{GeV}}) \tag{5.8}$$

[124] At higher energies, the energy resolution is getting better compared to lower energies and for more than 10 TeV the MuE energy estimate is in approximation scaling linearly with the muon energy. Since at low energies most muons pass through the instrumented volume of the detector, MuE leads to an overestimate of the energy in that region [125]. Also for large stochastic losses, MuE has sizeable errors, since the distribution of energy losses (dE/dx) has a long high-energy tail that shifts the mean and enlarges the errors.

MuEX

MuEX is the derivative of MuE and uses a more sophisticated likelihood function, that incorporates the systematic (model) error term, and allows it to be skewed in order to adopt to the high-energy tail. As a result high variations in energy losses are not penalized as much as low. Additionally, it implements the ice properties as a function of depth [126].

Truncated Mean Energy

Alternatively to MuEX the truncated mean energy estimator [127] can be used. The method divides the track into 120 m bins which are bordered by planes perpendicular to the track. The dE/dx value is determined by finding the ratio of the observed photoelectrons to the expected photoelectrons, but a separate ratio is determined for each bin instead of the event as a whole. Then a fraction of the bins with the highest ratios are discarded, and the truncated dE/dx is calculated by summing the remaining observed photoelectrons and expected photoelectrons and creating a new ratio.

5.1.4 Simulation

Simulation by using Monte Carlo methods is a fundamental process in order to determine the performance of the detector. It is not only used in describing cosmic ray interactions in the atmosphere (see Sec. 3) or the light propagation in the ice, but also for optimizing the event selection and for sensitivity calculations. The simulation chain in IceCube can be divided into the following steps:

1. Event generation
2. Lepton propagation
3. Photon propagation
4. Detector response

The first step consists in the generation of the primary particle, which is in IceCube done by a neutrino generator based on the ANIS (All Neutrino Interaction Simulation) [128] package. It is able to simulate all three neutrino flavours and propagate them from the Earth's atmosphere to the detector, while undergoing CC and NC-interactions. The neutrinos are simulated with a certain power-law spectrum, where all values for the detection probability and volume are stored in a variable called OneWeight (OW). The events can later get re-weighted in using

$$w = \Phi \cdot OW \cdot T/n \tag{5.9}$$

with the according flux Φ, lifetime T and the number of generated events n. The atmospheric muon background is simulated in using the CORSIKA [129] program, which can fully simulate atmospheric air showers produced by a cosmic ray primary.

In order to discriminate also the atmospheric neutrino flux from possible signal neutrinos, the atmospheric component needs to be simulated in detail. However, the simulation of complete air showers with CORSIKA in order to calculate the atmospheric neutrino flux is quite elaborated and requires a lot of computing resources. In IceCube, a tool called NeutrinoFlux [130] is used to evaluate the neutrino flux, which reads tables of parameters, extracted from fits of atmospheric neutrino flux tables and can be adjusted to the different models. In IceCube cosmic rays are usually simulated in following the poly-gonato [131] model.

The second step consists of the muon propagation through the ice and is based on Muon Monte Carlo (MMC) [123]. It evaluates the stochastic energy loss along the muon track at different levels of accuracy.

The photon propagation simulates the Cherenkov light yield, taking the ice properties into account. Two different approaches exist in IceCube: Lookup tables (Photonics) [110] and direct photon propagation (PPC) [132]. Photonics uses predefined tables of photon arrival probabilities, produced on standard CPUs for all possible configurations, yielding a high processing speed in simulations. PPC computes the propagation of photons inside the detector directly with the use of GPUs, allowing a parallelized computation. Both propagators take the optical properties of the ice into account. Photonics however, suffers from binning effects, while the direct propagation is more exact and will be the standard propagation module in future simulations. The last step in the simulation chain is the detector response, where typical types of noise are added using NoiseGenerator and the waveforms and their processing is simulated by the DOMLauncher. From then, the same trigger conditions are applied as for the real data.

5.1.5 Event Selection

The background rejection performed by the online filter is not sufficient for high-level data analyses. In the northern hemisphere, high-energy neutrino candidates can be selected from the data by rejecting events with a poor reconstruction, since they are more likely to be down-going muons. This is done in removing such mis-reconstructed events with multiple muon tracks and by suppressing events with very low energies [18]. In the southern sky, it is not possible to suppress the muon background based on the reconstruction quality of the events. Therefore, the most energetic events are chosen instead of improving the ratio of signal to background events [133]. An overview of the different steps involved in the event selction is shown in Fig. 5.5.

The possibility to observe a neutrino point source depends not only on the expected background and the observed neutrino flux, but also on the energy and angular resolution of these events. The discovery potential, as defined in Sec. 5.6.1 is connected with all these elements and is used as the main parameter in the optimization of the event samples. As described in [134], Fermi acceleration favours a spectral index of ∼2 and therefore in point source studies a E^{-2} spectrum is usually used as a benchmark scenario. However, also the idea of cutoff or softer spectra is supported by several galactic

Figure 5.5.: Sketch of the different steps involved in the event selection, starting with the triggers and filters performed at the South Pole up to the final point source sample selection in using BDTs at Level 4.

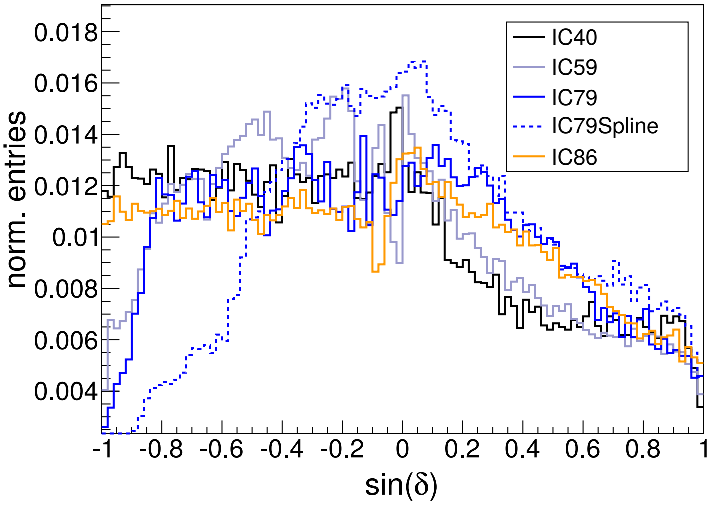

Figure 5.6.: Experimental declination distribution for the different datasamples used in this work.

gamma ray sources revealing a cutoff in their spectra. Thus, also softer spectra, such as $E^{-2.7}$ and E^{-3} are taken into account [18].

5.1.6 Experimental Sample

All data used here is based on muon tracks, which have an excellent angular resolution of $< 1^\circ$ and are therefore pointing back to the original source. In order to reflect the different detector geometries and the general improvement in the muon track reconstruction and identification of muon background events, different event selections for each of the year of data was used. In the next section the event selection for each year will be described briefly, since the event selection of the data sample was not part of this work. More detailed information can be found in [18].

IC40 Data Sample

The IC40 data sample contains data taken in the 40-string configuration from April 2008 to May 2009, with an uptime of 375.5 days. The event selection for the point source analysis is mainly based on cuts on different well-understood and powerful variables, as described in [135]. In the southern sky, a cut on the reconstructed energy of the event was performed, which was parameterized as a function of the reconstructed declination. The final sample consists of 36900 events, of which 14 121 are reconstructed as upgoing and 22 779 as downgoing, see also Tab. 5.1. The distribution of the declination is shown in Fig. 5.6.

IC59 Data Sample

The IC59 data sample uses data from May 2009 to May 2010 having an uptime of 348.1 days. For the event selection Boosted Decision Trees (BDTs) [136, 137, 138] are used instead of straight cuts. The cuts were based on twelve variables with a high discriminating power between signal and background. For the training of the BDTs 10% of the atmospheric muon dominated data was used as a background model and the signal was modelled with MC simulation based on a E^{-2} and a $E^{-2.7}$ spectrum to account for softer neutrino spectra. For computational reasons, the observables were split in two sets of eight and four variables, with a BDT each. In the final selection a combination of both BDT scores was used. Additionally, a veto of the surface array IceTop was used to reduce the muon background. Since atmospheric neutrinos are produced by extensive air showers, they are always accompanied by other particles, which are registered as early hits in IceTop. The veto rejects events in counting the photons observed in a time window around the expected arrival time of the shower front and is used for declinations between -90° and -40°. It yields a background rejection efficiency of 99 % in the vertically down-going region. The final sample has 107 569 events in total, of which 43 312 are reconstructed upgoing and 64 257 downgoing [18]. The declination distribution of this datasample is shown in Fig. 5.6. The lower event rate below sine declination -0.8 is due to the IceTop veto, introduced in this year of data taking.

IC79 Data Sample

For the IC79 data sample [18] data was taken from June 2010 until May 2011 with an uptime of 316.2 days. As for IC59 the event selection is based on BDTs. For that, the sample is divided in two sub-samples according to the events reconstructed zenith. One declination band uses mainly horizontal events (90° - 130°), where the signal is dominated by higher energy events and the other vertical events (130° - 180°). For both regions a separate BDT was applied using nine variables in the vertical region and fifteen variables in the horizontal region. Taking again E^{-2} and $E^{-2.7}$ spectra each, this results in eight BDTs in the northern hemisphere, which are again combined afterwards. In the southern hemisphere however neutrinos can not be isolated from the high-energy atmospheric muon bundles, coming from an air shower, mimicking neutrinos. Therefore, only one BDT is trained for the entire region using data for the description of the background and a E^{-2} signal model. For having a smooth transition in the event rate in the different declination regions, an energy cut depending on the declination was applied to select a constant number of events per solid angle. As in IC59 the IceTop veto was used to reject down-going atmospheric muon background at vertical zenith angles. The final data sample contains then 109 866 events, with 50 855 reconstructed on the northern hemisphere and 59 011 on the southern hemisphere.

In addition, based on the IC79 sample, a second sample based on the event selection of the standard IC79 sample was produced, using the SplineMPE instead of standard MPE [101]. The final data sample includes 93 842 events, with 48 904 reconstructed on the northern hemisphere and 44 938 on the southern hemisphere. It will be called IC79Spline in this work. The declination distribution for both samples is shown in Fig. 5.6 and displays a different distribution for the original IC79 and the IC79Spline sample. This is due to a strong additional background rejection of the IC79Spline sample of up to a factor of 3 in the downgoing region below sine declination values of -0.4, while the signal efficiency is retained. This improvement is mainly caused by the optimized BDT configuration and possibly better discrimination of atmospheric muon bundles by the Spline based variables [101].

IC86 Data Sample

This is the first year of data from the complete 86-string detector configuration, collected between May 2011 and May 2012 with an uptime of 333 days [139]. For the event selection in the northern hemisphere extending 5° above the horiozn, four BDTs in two zenith bands are used, to separate astrophysical neutrino signal from the atmospheric muon background. They are optimized for both, E^{-2} and $E^{-2.7}$ spectra, since the Earth and glacial ice still provide a shield from the cosmic ray background and use eleven variables in total. In the southern hemisphere only one BDT is trained for the entire region using data for the description of the background and a E^{-2} signal model, as described above. One main goal here is to separate single muons from muon bundles in using information on event topology and energy loss. The large muon bundles consist mainly of low energy muons that typically lose energy at a constant rate while traversing the detector. Highly energetic muons induced by a neutrino have instead a stochastic energy loss profile. Likelihood ratios are constructed to sort the events after these criteria into signal and background and are included into the BDT. The final data sample consists of 138 322 events, of which 69 227 are reconstructed upgoing and 69 059 downgoing [139]. The distribution of the declination is shown in Fig. 5.6.

In this work three experimental samples combining different years of data taking are used in the different analyses and are shown in Tab. 5.2. The first analysis, a two-point correlation (2-pt) function of the full sky was applied on a three year data sample consisting of IC40, IC59 and IC79 data. The second analysis, a multi point source

Data Sample	data period	uptime	total events	upgoing	downgoing
IC40	April 2008 - May 2009	375.5d	36 900	14 121	22 779
IC59	May 2009 - May 2010	348.1d	107 569	43 312	64 257
IC79	June 2010 - May 2011	316.2d	109 866	50 855	59 011
IC79Spline	June 2010 - May 2011	316.2d	93 842	48 904	44 938
IC86	May 2011 - May 2012	333 d	138 322	69 227	69 059

Table 5.1.: Data Samples taken on different years of IceCube. Shown are the periods in which the data was taken and the according detector uptimes for each year of data. Additionally, the total number of events and the number of events for each hemisphere is illustrated.

	2-year sample	3-year sample	4-year sample
IC40		x	x
IC59		x	x
IC79		x	
IC79Spline	x		x
IC86	x		x
Analysis	STFS	2-pt	MPS

Table 5.2.: Combined Data Samples taken for the different analyses.

(MPS) search, used a four year sample adding a year of IC86 data to the previous sample. In addition, it used the IC79Spline sample, in which the event selection is based on the Spline reconstruction. The third analysis, a self-triggered flare search (STFS) used only IC79Spline and IC86 data, since it is strongly connected to the results of the High Energy Starting Events (HESE) analysis, which was performed on data from the 79 and 86-string configuration.

5.1.7 Monte Carlo Samples

Simulated Monte-Carlo (MC) [140] data is used in many ways in IceCube, especially for optimizing the event selection and for getting an accurate description of the atmospheric muon background. In this work, however, MC data is used only for simulation of the astrophysical signal in sensitivity and limit calculations, since the background estimation is based on experimental data. Background MC simulations by CORSIKA are used only as an additional cross-check to verify the understanding of the detector. This makes the analysis more robust against systematic discrepancies between data and MC simulations. The MC data is simulated for each year separately taking the different detector configurations into account. Afterwards, it is selected in the same way as the experimental data, e.g. the same cuts and BDTs are applied. The simulated

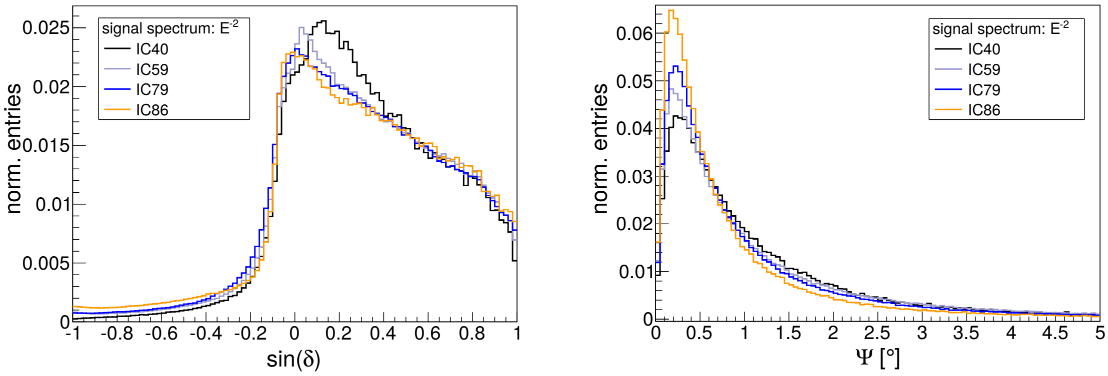

(a) Declination

(b) Point Spread Function

Figure 5.7.: (a) Declination distribution δ and (b) Point Spread Function Ψ for the different MC datasamples showing an E^{-2} spectrum.

spectra are relatively hard E^{-1} spectra with forced interaction in the detector. The events are then re-weighted to E^{-2} or E^{-3} spectra. Due to the effect of the forced interaction, the E^{-1} generated spectrum is adequate for this and ensures sufficient statistics at high energies. The declination distribution of the MC-samples for a E^{-2} spectrum are shown in Fig. 5.7(a) for the IC40, IC59, IC79 and IC86 datasample. For the northern hemisphere the neutrino shadow of the earth is visible in an increasing structure towards the horizon in all samples. For the southern hemisphere the detector acceptance is in general smaller, due to strong cuts and the large background.

Point Spread Function

From full detector MC simulation the angular resolution of signal events can be estimated. Since the angular resolution of the detector depends on the energy spectrum, the distribution of the angular reconstruction error Ψ, i.e. the Point Spread Function (PSF), is obtained for different energy spectra (E^{-2}, $E^{-2.25}$ and E^{-3}) and for each detector configuration. As an example, for an E^{-2} spectrum, the PSFs for IC40, IC59, IC79 and IC86 are shown in Fig. 5.7(b). It can be seen, that the angular reconstruction improves with the development of the datasamples.

Effective Area

MC data can also be used for evaluating the detector's efficiency. This efficiency is a function of the energy and zenith angle of an incoming neutrino. It can be characterized by the effective area $A_{\text{eff}}(E, \theta)$, which is the corresponding area of a hypothetical detector that has 100 % efficiency for detecting neutrinos of the given energy E and incident zenith angle θ. For a neutrino source at a given declination in the sky, the number of detected neutrinos is proportional to a convolution of the energy-dependent

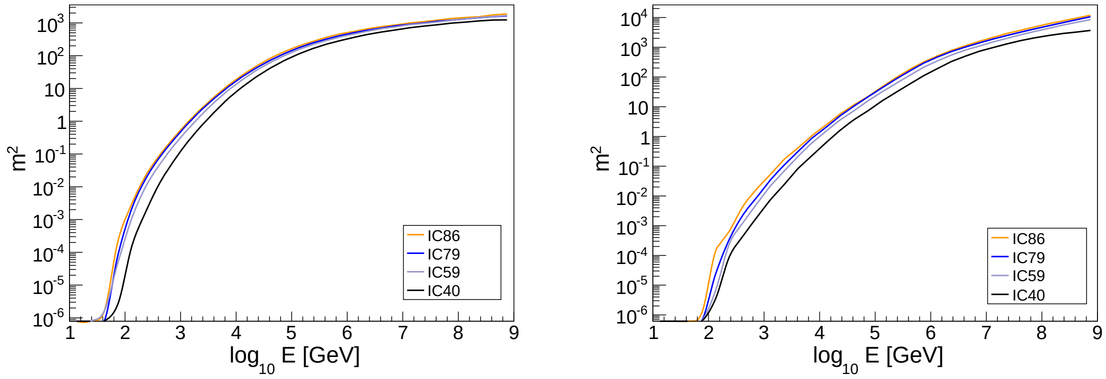

(a) A_{eff} for the northern hemisphere

(b) A_{eff} for the southern hemisphere

Figure 5.8.: Effective Area A_{eff} for the different data samples as a function of the energy for (a) the northern hemisphere and (b) the southern hemisphere.

effective area (evaluated at the appropriate zenith angle) and the energy spectrum of the source. As an illustration, the solid-angle-averaged effective area $A_{\text{eff}}(E)$ for the northern and southern sky are shown in Fig. 5.8 for the final event selection.

5.2 Likelihood Point Source Searches in IceCube

Identifying point-like sources of neutrinos and thus cosmic rays, is one of the main tasks of IceCube. This is done by searching for clusters of events that are significantly incompatible with the atmospheric muon and neutrino background. The method used is an unbinned maximum likelihood ratio test, as described in [141]. It uses not only the spatial clustering of events but includes also the energy, since astrophysical signal is expected to have a harder energy spectrum as atmospheric muons and neutrinos. An assumed source with location x needs then a source pdf $S(x, E, \gamma)$, describing the spatial and energetic distribution of signal events with a given spectrum γ and a background pdf $B(x, E)$, describing the spatial and energetic distribution of background events. The source pdf, which is modelled with a two-dimensional Gaussian and the background pdf are then combined in the likelihood $\mathcal{L}$

$$\mathcal{L}(\mathbf{x}_s, \gamma, n_s) = \prod_{n_{tot}}^{i=1} \frac{n_s}{n_{\text{tot}}} S_i(|\mathbf{x}_i - \mathbf{x}_s|, E_i, \gamma) + \left(1 - \frac{n_s}{n_{\text{tot}}}\right) B(\mathbf{x}_i, E_i) \tag{5.10}$$

with n_s as the hypothesized mean number of signal events, and n_{tot} as the observed total number of events in the final data sample. The best estimate for the number of signal events $\hat{n}_s$ and the best source spectrum $\hat{\gamma}$ is found by maximizing the log likelihood ratio λ with respect to the null hypothesis:

$$\log \lambda = \log \left(\frac{L(\mathbf{x}_s, \hat{\gamma}, \hat{n}_s)}{L(n_s = 0)} \right) . \tag{5.11}$$

In an allsky search, the source location is varied on a grid of points much finer than the experimental angular resolution. Since just by chance spots on the sky can look signal-like, the search is repeated several times on background data which is randomized in right ascension (r.a.). Each repetition here is called trial and results in a most-significant hottest spot. Out of these distributions the p-value of the actual hottest spot is obtained.

5.3 Two-Point Correlation Function

The strength of the likelihood method test lies in identifying a single strong source over background. However, if the signal is dominated by various weak sources instead of a single strong source, the likelihood test looses sensitivity and autocorrelation functions as the two-point (2-pt) correlation functions get more favourable. 2-pt correlation functions were first described in the late 70s by Peebles [142] and co-workers [143, 144] studying the large-scale structure of galaxies. It is a powerful statistical method in measuring the clustering strength on different scales. It is applied widely in high energy astrophysics for detecting anisotropies in the spatial distribution of cosmic rays [145, 146] and neutrinos [147]. The autocorrelation test is based on the distribution of pairwise calculated spatial distances (Ψ_{ij}) between events i and j, which are compared to the background expectation. It is designed to detect an event clustering at angular scales, θ, comparable to the detector resolution. Since it is a non-parametric test, no prior information of the potential sources, such as the spatial morphology or the spectral shape, is required. The amount of clustering is then obtained from scanning simultaneously over θ and different bins for the minimum energy E_{min} that optimizes the sensitivity.
With Ψ being the spatial distance between two events, the test statistic of the 2-pt analysis can be defined as a function of θ by

$$TS(\theta, E_{\mathrm{min}}) = \frac{\text{obs. no. pairs with } \Psi_{\mathrm{i,j}} \leq \theta, E_{\mathrm{i,j}} \geq E_{\mathrm{min}}}{\text{avg. no. bg. pairs with } \Psi_{\mathrm{i,j}} \leq \theta, E_{\mathrm{i,j}} \geq E_{\mathrm{min}}} , \tag{5.12}$$

or, more precisely, by

$$TS(\theta, E_{\mathrm{min}}) = \frac{\sum_{i,j \in H, i>j} \Theta(\theta - \Psi_{ij}) \cdot \Theta(E_{i,j} - E_{\mathrm{min}})}{\langle \sum_{m,n \in H, m>n} \Theta(\theta - \Psi_{mn}) \cdot \Theta(E_{m,n} - E_{\mathrm{min}}) \rangle_{bg}} , \tag{5.13}$$

where E_i is the reconstructed muon energy of event i (see [122] for details on the energy reconstruction), which is a lower bound of the primary neutrino energy and $E_{i,j} = \min(E_{\mathrm{i}}, E_{\mathrm{j}})$. The pairs of events i and j inside the hemisphere, H, are counted, with Θ being the Heaviside function. The background expectation enters in the denominator and is obtained by averaging over a large number of pseudo-experiments using a uniform

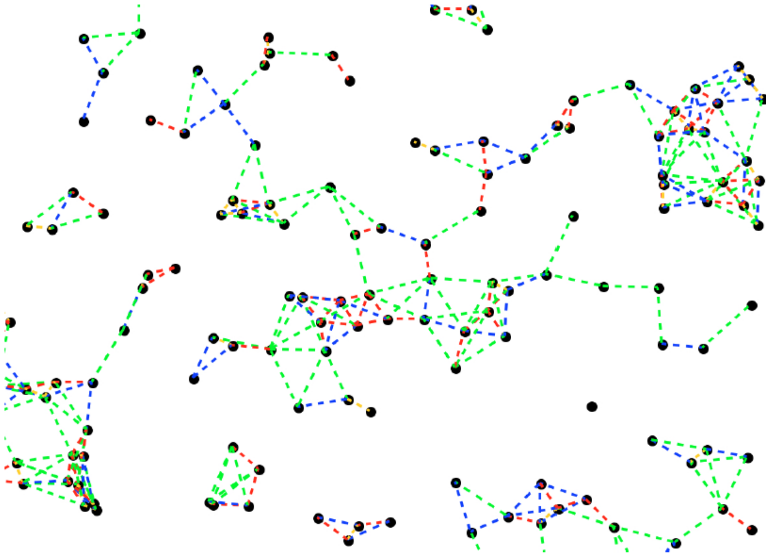

Figure 5.9.: Sketch of the autocorrelation method and counting pairs algorithm. The dotted lines represent counted pairs with four different θ bins symbolized by the colors green, blue red and orange, going from the largest θ to the smallest [148].

right ascension distribution. E_{min} is the minimum energy defining each energy bin. From this pseudo-experiments on pure background a range of probabilities P_{Bg} for the number of pairs in every energy- and θ-bin is acquired. The probability $\mathcal{P}(\theta, E_{min})$ of finding an excess over random background is then given by

$$\mathcal{P}(\theta, E_{min}) = \sum_{n=n_p}^{\infty} P_{Bg}(\theta, E_{min}, n) = 1 - \sum_{i=0}^{n_p} P_{Bg}(\theta, E_{min}, n) \tag{5.14}$$

with n_p being the number of pairs obtained in a measurement. The minimum of $\mathcal{P}(\theta, E_{min})$ is called the strongest potential clustering signal.

GPU Implementation

The evaluation of the clustering function and thus, the calculation of distances of these events and the execution time scales with the order $\mathcal{O}(n^2)$. A sketch of the autocorrelation method in counting pairs is shown in Fig. 5.9. In future applications will be a need for more statistics, which could lead to problems with the CPU time and the limited computing resources. In order to avoid these problems, a GPU-based version of the 2-pt method was developed in collaboration with a Bachelor work [148]. For that a 2-year data sample of IC79 and IC86 data was used.
The method of the 2-pt is highly suitable for a GPU-version, since individual operations can be executed separately and the access to the memory is predictable and linear. In parallelizing the outer loop, N threads can be started in parallel, while iterating over the sum of events. All data, as the specific angles can be kept in the local registers of the threads. Additionally, a method for copying the necessary data to and from the

	Original	Zenith sorting	Improved Binning	Pre-computing
CPU	1530	324	292	22
GPU	45	3.5	2.9	0.7

Table 5.3.: Overview of the execution times in seconds for one trial of the 2-pt for CPU and GPU versions. The different code optimizations lead to an even further increase in speed [148].

GPU machine was developed. Comparing a single 3.3 GHz Intel Ivy Bridge CPU to a nVidia Geforce GTX Titan, this approach yields a speed advantage of 70x, bringing the execution for one trial time down to 22 seconds from an original 25 minutes, see Tab. 5.3. The results in CPU and GPU machines are slightly different, due to rounding effects and effects in the implementation of the trigonometric functions. However, this effect is in the order of 10^{-5} and marginal. Furthermore, different improvements in the code have been carried out, to increase the execution time even further. As an example, the pre-computing of the trigonometric functions leads to a speed-up of ∼6x. An improved binning and a sorting in zenith are additional improvements. A detailed description can be found in [148].

5.4 Energy-Weighted Multi Point Source Analysis

The Multi Point Source (MPS) Analysis was first developed in 2009 [149] and is based on the evaluation of the spatial event pattern in a certain search region, using again the 2-pt clustering function. It was developed to search for multiple (neutrino) sources inside a specific search region that is larger than the angular resolution of the detector. It was applied to IceCube data in [150] to search for astrophysical neutrinos inside the Cygnus region. Since astrophysical neutrinos are often expected to have harder spectra than the atmospheric neutrino background, the method has now been extended to include energy-weights [151] and is called energy-weighted multi point source analysis (eMPS).
With Ψ_{ij} being defined as the spatial distance between two events i and j the test statistic of the eMPS is defined correspondingly to the 2-pt as a function of the clustering scale θ by

$$TS(\theta) = \frac{\text{obs. weighted no. pairs with } \Psi \leq \theta}{\text{avg. weighted no. bg. pairs with } \Psi \leq \theta}\,, \tag{5.15}$$

and more precisely by

$$TS(\theta) = \frac{\sum_{i\in P}\sum_{j\in S, i\neq j} W(E_i)\cdot W(E_j)\cdot \Theta(\theta-\Psi_{ij})}{\langle \sum_{m\in P}\sum_{n\in S, m\neq n} W(E_m)\cdot W(E_n)\cdot \Theta(\theta-\Psi_{mn})\rangle_{bg}}\,. \tag{5.16}$$

Here, P is the set of events i that are inside the search region, while S is the set of all events j, located anywhere. Thus, only event pairs with at least one event inside the search region are counted. The background expectation $\langle ... \rangle_{bg}$ enters in the denominator and is obtained by averaging over a large number of pseudo-experiments performed on background-only data, with Θ being the Heaviside function. $W(E_i)$ is the energy weight for event i.

The energy weights $W(E_i)$ are obtained from the pdf $\mathcal{P}(E)$ of the reconstructed energies in the background by using the probability to observe an event with equal or higher energy in the background. $W(E_i)$ is given by

$$W(E_i) = 1 - \int_{E_i}^{\infty} \mathcal{P}(E) dE = \int_{0}^{E_i} \mathcal{P}(E) dE \,. \tag{5.17}$$

In taking the energy weights from distributions of data, they are independent from specific signal models and hold down the systematics in the test. Events with higher energies get larger weights, while events with lower energies get lower weights. This ensures the benefit of the test from events with energies above the average atmospheric background.

The test is sensitive to any neutrino emission in the tested area, which can be a small number of point sources as well as some extended sources. Also, an additional diffuse component, which could emerge from neutrinos interacting with matter inside the search region, could be a potential source scenario.

5.5 Self-Triggered Flare Search

The self-triggered flare search is an advancement of the eMPS search and was developed in the light of the first measurements of astrophysical neutrinos in the High Energy Starting Events (HESE) Analysis. It is designed to search for flaring point sources, that can be attributed to the events found in the HESE search. For that, different event selections are combined in taking the HESE events as a trigger for the point source sample and search for an excess in time and in space in coincidence to the HESE events. As a base, the eMPS method is used and extended by a search for time clustering and a stacking approach in evaluating the cumulative signal of several HESE events. With τ being defined as the time of a point source event and $\Delta\tau_k$ the flare interval around the time of a HESE event k and Ψ_{ij} being again defined as the spatial distance between two events i and j, the test statistic can be defined as

$$TS(\theta, \tau) = \frac{\text{obs. weighted no. pairs with } \Psi \leq \theta, \tau \leq \Delta\tau}{\text{avg. weighted no. bg. pairs with } \Psi \leq \theta, \tau \leq \Delta\tau} \,, \tag{5.18}$$

and more precisely by

$$TS(\theta, \tau) = \frac{\sum_{k \in R} \sum_{i \in P} \sum_{j \in S, i \neq j} W(E_i) \cdot W(E_j) \cdot \Theta(\theta - \Psi_{ij}) \cdot \Theta(\Delta\tau_k - \tau_{i,j})}{\langle \sum_{k \in R} \sum_{m \in P} \sum_{n \in S, m \neq n} W(E_m) \cdot W(E_n) \cdot \Theta(\theta - \Psi_{mn}) \cdot \Theta(\Delta\tau_k - \tau_{m,n}) \rangle_{bg}} \,.$$

Here, R is the set of HESE events used as a trigger in the search, while P is the set of point source events inside the search region, and S is the set of all events. Again, the background expectation $\langle ... \rangle_{bg}$ enters in the denominator and is obtained by averaging over a large number of pseudo-experiments performed on background-only data, with Θ being the Heaviside function. The energy weights $W(E_i)$ are obtained as described above.

5.6 Methods in Evaluating the Significance

In order to estimate the significance of an analysis and to be able to do comparisons to other analyses and collaborations, different statistical methods are commonly applied. The two most important concepts here are the sensitivity and the discovery potential, outlined in the following sections.

5.6.1 Discovery Potential

The discovery potential gives, as the name reveals, the probability of a discovery with respect to the null hypothesis. In the case of autocorrelation functions it evaluates the test statistic of isotropic background and the test statistic of different signal hypotheses introducing an event clustering. It is defined as the required number of signal neutrinos, where 50 % of the cases give a $5\,\sigma$ deviation from the observed background. The $5\,\sigma$ deviation corresponds to a quantile of $2.87 \cdot 10^{-7}$ of the background distribution. Applying the solid-angle-averaged effective area ($A_{\mathrm{eff}}(E)$ - see section 5.1.6) of the detector for the different samples, the resulting discovery potential in terms of n_{sig} can be converted to fluxes. This is done using

$$E^{\gamma}\frac{\mathrm{d}\phi}{\mathrm{d}E} = \frac{n_{\mathrm{sig}}}{T_{\mathrm{up}}\int\limits_{0}^{\infty}\mathrm{d}E\, A_{\mathrm{eff}}(E)E^{-\gamma}}\,, \tag{5.19}$$

where n_{sig} is the number of signal neutrinos fixed by the signal parameters with the number of sources N_{Sou}, the sources strength μ, the spectral index γ and T_{up} is the detector uptime.

5.6.2 Sensitivity

The sensitivity defines the amount of signal needed to shift the median of the test statistic beyond the 90 %-quantile of the background distribution. It corresponds to a σ value of $\sigma = 1.29$ and can be converted into fluxes, correspondingly to the discovery potential, using Eq. 5.19. The smaller the amount of signal events needed, the more sensitive is an analysis and can in this way be compared to other analyses.

IceCube has completed different point source searches, including an energy-dependent likelihood point source search scanning the full sky [18, 139], as well as searches for flaring and periodic neutrino emission [19]. Additionally there are searches for diffuse neutrino emission looking for deviations in the two dimensional distribution of energy and zenith angle [20]. Point source searches are most sensitive for finding individual sources of astrophysical neutrinos among the background of atmospheric events (neutrinos and muons from cosmic ray interactions at Earth). Diffuse searches, on the other hand, are most sensitive for detecting within this background the presence of high-energy astrophysical neutrinos throughout the sky, without identifying individual sources. In between these two scenarios is the possibility that many weak sources exist. These could contribute to the detected diffuse signal and create a small number of events clustering on the background event distribution, while the individual clusters remain too weak to be detected by the point source searches.

In the following chapters several searches for such a small-scale clustering using autocorrelation functions are presented. Chapter 6 describes a generic allsky search using a 2-pt correlation function including a specific search on higher energies. The second search aims at the Cygnus region (see Chapter 7) and uses the eMPS method. The third analysis extends the eMPS method in triggering with the positions and times of the HESE events and is discussed in Chapter 8.

6

Analyses using a Two-Point Correlation Function

As described in Sec. 5.3 the 2-pt correlation function aims on the detection of many weak sources with unknown energy spectra. This chapter describes two autocorrelation tests, the first one applied on a 3-year data sample on the full sky, while the second test is a refinement on high energies and investigates the 100 highest energetic events in the IC79 sample.

6.1 All-Sky Two-Point Correlation Search

In this analysis the angular scale θ is varied from 0° to 5° using a step size of 0.25°. In addition, four energy bins are used, that contain: all events, the 10 %, 1 % and 0.1 % of the most energetic events observed in data, in order to have a better background suppression. The 0.1 % sample for the northern hemisphere, for example, contains only the 100 highest-energy events. By using different energy thresholds, the discovery potential for high energy signals is improved while the sensitivity to sources with soft energy spectra is retained. By varying the step size, the scan itself can determine the best energy and θ binnings that maximize the signal [145].

The autocorrelation analysis is performed on a three year datasample, consisting of IC40, IC59 and IC79 data, see Sec. 5.1.6, which is divided into the northern and southern hemisphere at a declination of 0°. The reconstruction methods used are the MPE for the angular reconstruction and MuE as energy estimator, see Sec. 5.1.2 for details. In the data sample of the northern hemisphere, events have neutrino energies between 240 GeV and 1.2 PeV. For the 10 % sample, the lower energy bound increases to 6.3 TeV, while for the 1 % and 0.1 % samples the lower threshold is 31.6 TeV and

Data Sample	fraction	lower threshold	upper threshold
northern hemisphere	100 %	240 GeV	1.2 PeV
	10 %	6.3 TeV	1.2 PeV
	1 %	31.6 TeV	1.2 PeV
	0.1%	120 TeV	1.2 PeV
southern hemisphere	100 %	490 GeV	8 PeV
	10 %	630 TeV	8 PeV
	1 %	1.3 PeV	8 PeV
	0.1%	2.7 PeV	8 PeV

Table 6.1.: Ranges of the neutrino energies for the two hemipsheres and the four different energy samples.

120 TeV, respectively [122], illustrated in Tab. 6.1. For the southern hemisphere, the energies range from 490 GeV to 8 PeV. For the 10 % sample this range increases to 630 TeV and for the 1 % and 0.1 % samples the lower threshold lies at 1.3 PeV and 2.7 PeV. Using toy MC simulations, pure atmospheric background sky maps, sky maps of pure point source signal and mixed sky maps are generated. These pseudo-experiments are used to develop the analysis method and to quantify the analysis performance (discovery potential). The generation of signal and background neutrinos is described in the following.

6.1.1 Background Estimation

Since atmospheric background events are expected to be isotropic, they can be used as a base for the background generation. Due to IceCube's location at the South Pole and the Earth's rotation the resulting right ascension acceptance is approximately uniform and can therefore be filled with randomly generated values. Repeating this process of randomization many times is called scrambling. However, the declination acceptance is not uniform (see Fig. 5.6) and needs to be kept as measured in data. The background test statistics is generated by performing over 20 000 pseudo-experiments on data using a uniform right ascension distribution. Since the production of more than 10^7 pseudo-experiments sufficient for the calculation of the discovery potential is too CPU-consuming, the data gets fit with two different distributions. The two highest energy bins, which contain the 1 % and 0.1 % of the events with the highest energy are fit with a Gamma distribution, while the two lowest energy bin, containing all events and the 10 % of events with the highest energy are fit with a Gaussian. An example for the two different Fits used in the analysis, is shown in Fig. 6.1(a) for the 10 % energy bin using Gaussian Function and in Fig. 6.1(b) in the 0.1 % energy bin using a Gamma Function. Both show an angular scale of $\theta = 0.25°$. Using this data driven approach, no additional systematic effects due to Monte-Carlo simulation are introduced. The

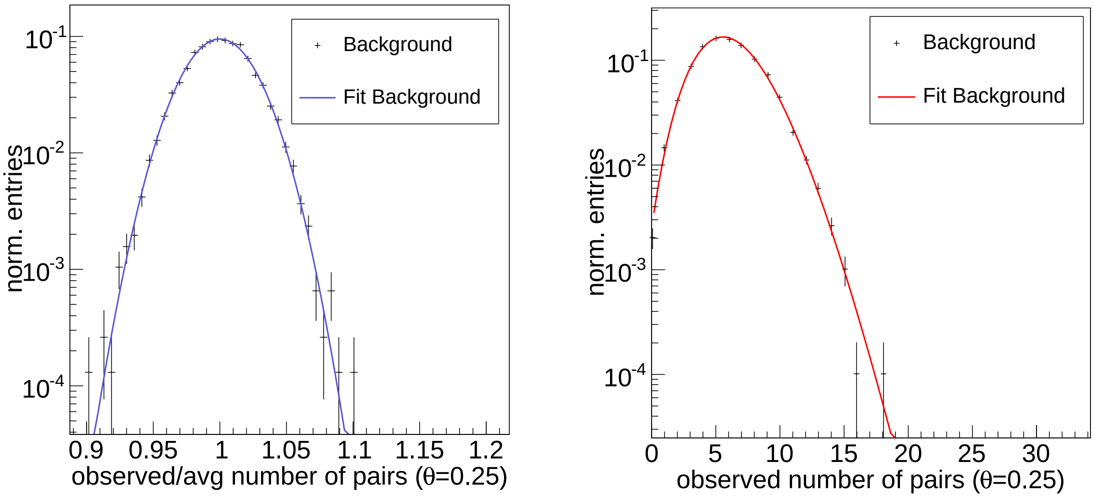

(a) Gaussian Function (b) Gamma Function

Figure 6.1.: Example for the Fits used in the extrapolation of the background. (a) TS averaged over the background expectation with a Gaussian Fit (blue) in the 10 % energy bin. (b) Background TS fitted with a Gamma Function (red). Both show an angular scale of $\theta = 0.25°$.

background test statistic can then be used to evaluate the significance of the test using different signal simulations.

6.1.2 Signal Simulation

For the signal simulation, maps containing simulated signal, e.g. distributions of point sources are produced. The signal maps depend on three parameters defining the signal: the mean number of neutrinos per source (μ), the number of sources (N_{sou}) in the sky (for the corresponding hemisphere) and the spectral index (γ) of the signal energy spectrum. In this analysis three different energy spectra of candidate neutrinos are investigated, a E^{-2}, $E^{-2.25}$ and E^{-3} spectrum. The choice of spectra is mainly motivated by Fermi acceleration [134] and is assumed to follow a power law of E with different spectral indices (γ). Additionally, the number of sources (N_{Sou}) is varied between one and several hundred sources with respect to the wide range of possible source candidates.

A signal skymap depending on the specific energy spectrum and the number of sources and signal events can be generated by applying the following steps:

1. The true source position is determined by randomly choosing its declination and right ascension.

2. Assign a random number of events produced by each source. This is taken from a Poisson distribution with a mean source strength of μ.

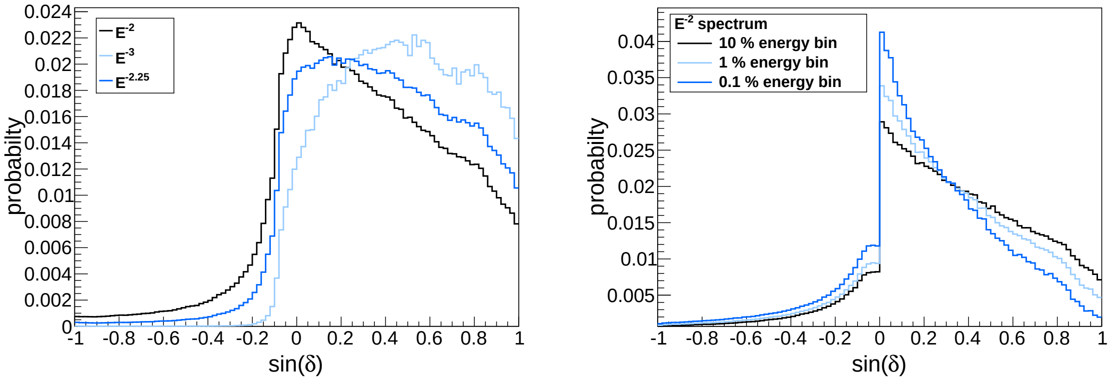

(a) For different energy spectra

(b) For different energy bins of E^{-2}

Figure 6.2.: Declination distribution δ for (a) different energy spectra and (b) different energy bins of an E^{-2} spectrum used as detector acceptance for the signal simulation. All histograms are obtained from MC simulation of isotropic signal events.

3. Distribute the signal events around the true source position according to the PSF of the specified energy spectrum, see Sec. 5.1.7 to take the detector's angular resolution into account.

4. Spread the signal events over the hemisphere, considering the detector's declination-dependent acceptance. This acceptance is derived from simulations, taking the normalized MC declination distribution for the specified energy spectrum. In using a hit-and-miss procedure [152], each generated event is rejected from or accepted to the simulated skymap, following the detector acceptance.

The expected number of neutrinos per source (μ_{eff}) in the simulated map depends then on Poissonian fluctuations and the declination of the source, such that μ_{eff} is given by the product of μ and the detector acceptance at the source's declination. In a next step, the simulated signal maps are inserted into the background maps, while for each inserted signal events on background events gets erased. This ensures, that the total number of events, n_{tot}, is fixed to the experimental dataset.
The declination-dependent detector acceptance, as obtained from MC simulation, is shown in Fig. 6.2(a) for E^{-2}, $E^{-2.25}$ and E^{-3} energy spectra. Additionally, the detector acceptance for the top 10%, 1% and 0.1% high-energy events of an E^{-2} energy spectrum is shown in Fig. 6.2(b). For the northern hemisphere, the expected neutrino flux from the pole region decreases at high energies which is due to the Earth's declining transparency to neutrinos. Therefore, for hard energy spectra and the highest-energy bins the signal is dominated by the horizon region, while for soft energy spectra and low-energy bins, the expected number of signal neutrinos from an isotropic signal is largely the same at all declinations. In addition, the declination-acceptance is influenced by declination-dependent cuts, applied to the data sample in [18]. In the southern hemisphere, the detector acceptance is comparatively much smaller due to

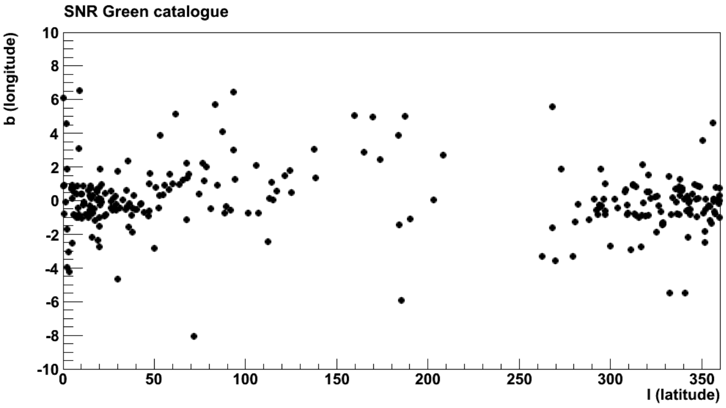

Figure 6.3.: Distribution of the 274 SNRs of the Green catalogue used in the Galactic Plane scenario in galactic coordinates.

strong cuts applied in [18] to reduce the atmospheric muon background. The observed smooth transition is due to the decrease of atmospheric muons at the horizon and the corresponding increase in signal efficiency.
In this analysis two different signal scenarios are simulated:

- a uniform distribution of sources on the hemisphere
- a distribution of sources following the Galactic Plane

The first signal model considered here contains sources with equal strength and a uniform distribution in the northern or southern sky. The second scenario is a spatial distribution according to the Green catalogue [153] of SNRs in the Milky Way, and contains 274 SNRs, as illustrated in Fig. 6.3. Thus, sources are distributed according to randomly chosen positions of SNRs of the catalogue and can vary from 50 to 200 sources. Since the sources are distributed only inside the Galactic Plane, this scenario exhibits a larger clustering between the sources compared to the first one.

6.1.3 Application to the Data: Discovery Potential

The test statistic for background and signal can be evaluated for each θ and energy bin separately. Figure 6.4 shows the distribution of the test statistic for the background events and the fit with a Gaussian for a clustering scale of 0.25° and in the energy bin containing 1 % of the data. Two signal scenarios, with a uniform distribution of sources in the northern sky, are also shown. The fit describes the data well and the signal is clearly distinguishable from the background expectation.
In order to evaluate which energy and theta bin is the most sensitive for the different spectra, the best clustering bin is estimated. This is done in counting for each trial how often the global p-value falls into the specific energy and θ bin and is shown in Fig. 6.5. It shows the best clustering bin for a E^{-2} spectrum and $E^{-2} \cdot e^{E/10TeV}$ spectrum, as a function of θ and the energy bins for the northern hemisphere. The colour bar displays

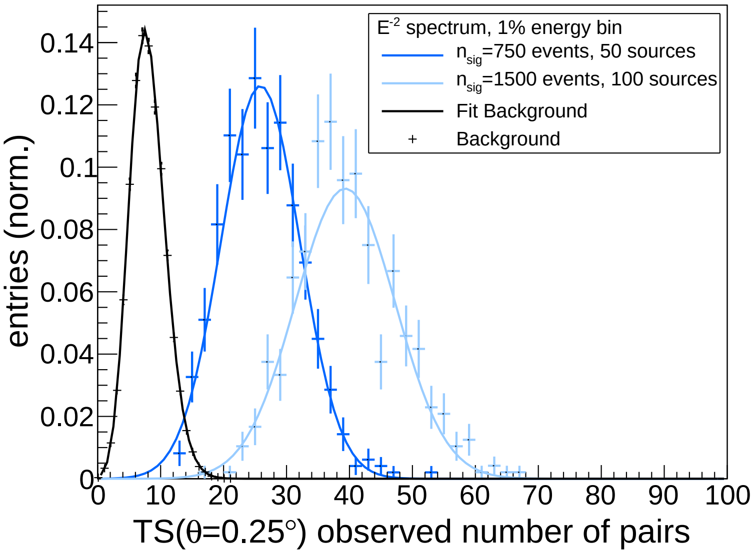

Figure 6.4.: Example test statistic for the autocorrelation analysis, showing the observed number of pairs for simulated data sets with and without signal. The case for the angular scale $\theta = 0.25°$ and the energy bin that contains the 1 % highest energy events is shown. The randomized data is fitted with a Gaussian and two signal scenarios with a uniform distribution of E^{-2} sources in the northern sky are shown. For $N_{\mathrm{Sou}} = 50$, the mean number of neutrinos per source μ was adjusted until the total number of signal events added to the full data sample (and replacing randomized data events at the corresponding declinations) was $n_{\mathrm{sig}} = 750$. Similarly for $N_{\mathrm{Sou}} = 100$, the example shown was constructed by adjusting μ per source until the number of signal events inserted in the full data sample was $n_{\mathrm{sig}} = 1500$

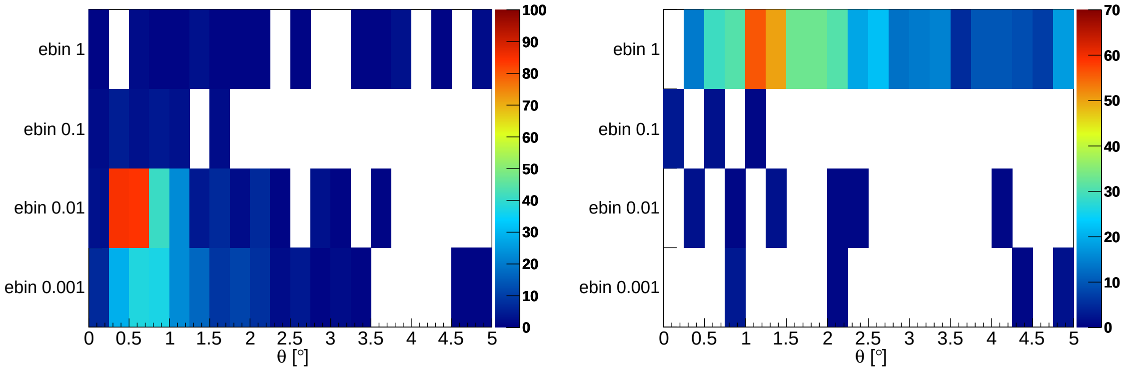

(a) Best clustering bin E^{-2} spectrum (b) Best clustering bin $E^{-2} \cdot e^{E/10TeV}$ spectrum

Figure 6.5.: Best clustering bin for a (a) E^{-2} spectrum and (b) $E^{-2} \cdot e^{E/10TeV}$ spectrum as a function of θ and the energy bins for the northern hemisphere. The colour bar displays the entries of global p-values in each bin.

the entries of global p-values in each bin. For a rather hard E^{-2} spectrum the most sensitive bin is in the 1% energy bin at small θ angles. For a spectrum with exponential cutoff the clustering takes mainly place in the 100% energy bin. These plots show, that the sensitivity of the analysis is not dependent on the spectrum of the possible sources, but could help in the interpretation of a potential signal. The best clustering bin for the southern hemisphere can be found in Fig. A.1 of the appendix.

The discovery potential is estimated as described in Sec. 6.1.3, in varying the number of signal events for different number of sources and comparing to the test statistic distribution for the background. Furthermore, the thresholds for the energy bins are re-calculated in order to keep the number of events fixed in every energy bin. The number of signal neutrinos can then be converted into fluxes using Eq 5.19. In each simulation of a given number of sources, the sources were simulated with the same individual source strength μ. The discovery potential includes also the correction for trial factors that come from testing different angular scales θ and different energy thresholds $E_{\min}$. This is done using $P_{global} = 1 - (1 - P_{local})^{N_{trials}=80}$, with P_{local} as the best p-value in each one of the 80 bins, P_{global} as the final trial-corrected p-value of each trial and $N_{trials} = 80$ as the trial factor incurred in scanning the 80 bins. Since the bins are mainly correlated, the effective trial factor is somehow lower, in the order of ∼25.

The $5\,\sigma$ discovery significance for the analysis is shown in Fig. 6.6(a) and Fig. 6.6(b) for the northern and southern hemisphere, respectively, assuming an E^{-2} neutrino spectrum and a uniform source distribution. The significances are compared to the discovery flux of the time-integrated point source likelihood search [18] averaged for each hemisphere, a multipole analysis [21] and to the recently found diffuse flux of astrophysical sources [16]. This is achieved by evaluating the best fit astrophysical flux for each spectral index which is converted into a flux per source by dividing the diffuse flux by the number of sources, assuming sources of equal flux at Earth. One should note that the point source discovery flux is shown for a single source and does not include trial factors for searching many locations which, over the whole sky, would increase the discovery flux by a factor of 2. For a E^{-2} spectrum, and more than ∼ 20 sources on the northern sky, the autocorrelation analysis is able to identify a signal that the point source likelihood search would not observe, while for the multipole analysis this is the case for more than ∼ 45 sources. The large difference between these two analyses is due to the hard energy spectrum, which is easier to extract with the autocorrelation analysis since it uses energy as an additional observable. For the southern hemisphere, the autocorrelation analysis is performing better than the point source likelihood analysis for more than ∼ 10 sources, while the multipole analysis is not shown, because it was only performed on the northern hemisphere.

Additionally, the $5\,\sigma$ discovery flux assuming a E^{-2} energy spectrum and a galactic source distribution is shown in Fig. 6.7(a) and Fig. 6.7(b) for the northern and southern hemisphere, respectively. As described above, it is also compared to the average discovery flux of the point source likelihood search.

In Fig. 6.8(a) the $5\,\sigma$ discovery flux for a E^{-3} neutrino spectrum with uniformly distributed sources is shown and compared to the discovery flux of the point source likelihood search for that spectrum. Above $\sim$ 20 sources, the autocorrelation analysis performs better than the point source likelihood analysis. For this energy spectrum, the discovery potential of both, the autocorrelation and the multipole analysis is similar, since the energy observable that is used by the autocorrelation analysis carries only little separation power between astrophysical and atmospheric neutrinos. Figure 6.8(b) illustrates the discovery flux for sources with a $E^{-2.25}$ neutrino spectrum for uniformly distributed sources. Again, the performance of the 2-pt analysis and the multipole analysis is similar, while a discovery potential for the point source likelihood analysis is not available.

6.1.4 Results

The autocorrelation test was applied to the presented data sample of the IC40, IC59 and IC79 configurations. In Fig. 6.9 the observed number of pairs for the northern hemisphere are shown as a function of the clustering scale θ and compared to the background expectation. For the lower energy bins and therefore high statistics the observed number of pairs follows very closely the background expectation, while for the highest energy bin, an underfluctuation is visible. This is due to the limited statistic in the last energy bin. The same plots are shown for the southern hemisphere in Fig. 6.10. Since the data sample contains more events in the southern part of the sky, the fluctuations for the highest energy bin are smaller.
The ratios of the observed number of pairs and the background expectation of this analysis are shown in Fig. 6.11 for the northern hemisphere and Fig. 6.12 for the southern hemisphere. In both hemispheres fewer pairs than expected were observed and a small underfluctuation is visible. The background distribution is used for the evaluation of the local p-values. The best pre-trial p-values are 0.16 for the northern and 0.055 for the southern hemisphere. Taking the trials for the different angular and energy bins into account results in a post-trial p-value of 0.84 for the northern hemisphere and 0.73 for the southern hemisphere. All results are consistent with fluctuations of the background.

6.1.5 Neutrino Upper Limits

From the results obtained, upper limits on the neutrino flux for the northern and southern hemisphere can be derived. The calculations for these limits at the 90% confidence level are based on the classical (frequentist) approach [154]. Using Eq. 5.19, the experimental value of the test statistic for the analyses can be converted into upper limits on n_{sig} and thus on the physical flux normalizations ($\Phi_0 = E^{\gamma}\frac{\mathrm{d}\Phi}{\mathrm{d}E}$) for different spectral indices (γ). Since the full clustering function is used in the calculation, the limits also need to be corrected for trials. This is done in the same way as for the discovery potential. The resulting limits on the flux normalization for the northern hemisphere and uniformly distributed E^{-2} neutrino sources are shown in Fig. 6.6(a).

For comparison, additional lines are drawn for the limit of the point source likelihood analysis [18], the multipole analysis [21] and for the converted flux of the HESE analysis. The average upper limit of the point source likelihood analysis is $2.7 \cdot 10^{-9}\mathrm{GeV/cm^{-2}s^{-1}}$. Figure 6.6(b) shows the limit for the southern hemisphere and uniformly distributed E^{-2} neutrino sources for the autocorrelation analysis. Again, the limit for the point source likelihood analysis and the converted HESE flux are shown for comparison and the average upper limits of the point source likelihood analysis is $5.5 \cdot 10^{-9}\mathrm{GeV/cm^{-2}s^{-1}}$.
In Fig. 6.7(a) and Fig. 6.7(b), the limits are shown for the northern and southern hemisphere for a E^{-2} neutrino spectrum in the galactic plane scenario. Both are compared to the converted HESE flux and the limits from the point source likelihood analysis.
In Fig. 6.8(a) and Fig. 6.8(b), the limits of the analysis are shown for a E^{-3} and a $E^{-2.25}$ spectrum, respectively. They are compared to the converted HESE flux, the multipole analysis and to the limit of the point source likelihood analysis for E^{-3}, while for $E^{-2.25}$ no limit from the point source likelihood analysis is available. The $E^{-2.25}$ spectrum is motivated by the HESE best fit of the spectral index.

6.2 Comparison to the HESE Flux

For a fit of an E^{-2} spectrum to the HESE data, the analysis is not able to detect the underlying source population except in the case that it consists of very few sources (the scenario for a detection in the previous point source likelihood searches). However, for fits of softer spectral indices to the HESE data like E^{-3} or $E^{-2.25}$, there are a range of source populations compatible with the HESE flux that could be detected by the autocorrelation analysis, but not by the point source likelihood analysis. For all tested signal hypotheses, the declination-dependent detector acceptance was correctly taken into account. However, it should be noted that in case of a non-isotropic signal, the given discovery potential is not valid since different declinations contribute differently to the total significances (s. Fig. 6.2). Additionally, large-scale structures in the source distribution would increase the clustering of events, allowing both methods to detect even smaller fluxes. Thus, the sensitivity depends strongly on the source distribution and can not simply be applied to model predictions.

6.3 Two-Point IC79 High Energy Study

This search is motivated by the stronger evidence for an astrophysical excess among the very highest energy events in the upgoing muon neutrino data of IC79. The 2-pt study presented above still has more than 100 events in the highest energy bin and could not have seen any clustering in this energy regime. In order to study the high energy events in more detail an additional test (2-pt HE) for the 100 most energetic events in the IC79 data sample was performed. A smaller energy binning in steps of 10 events is applied up to the most energetic 10 events observed in this sample, while

	Event 1	Event 2
RA [°]	285.68	287.15
Dec [°]	3.1	3.6
Energy [$\log_{10}$(GeV)]	5.507	5.59

Table 6.2.: Results of the high energy autocorrelation test in IC79 data. The best p-value was found at 1.75° in the 10 events energy bin showing one pair. The properties of the two events are shown.

the binning in θ stays the same. The background production and signal simulation is done in the same way as described above. Since the number of events and therefore the execution time for the background scrambling is low, 10^7 trials can easily be produced and no fitting functions are needed.

6.3.1 Results

The results of the additional high energy test of IC79 data only are shown in Fig. 6.13 as a function of the clustering scale θ and the energy bins. The best pre-trial p-value results in 0.035, one pair with a distance of 1.57° inside the 10 events energy bin. After taking the trial correction into account this turns into a post-trial p-value of 0.38. The pair of events has reconstructed parameters (right ascension, declination) of (285.7°,+3.1°) and (287.2°,+3.6°), see Tab. 6.2. The result is consistent with background fluctuations. Figure 6.14 shows the event views of the obtained pair inside the IceCube detector. The colour indicates the time, going from green to blue, while the size of the spheres illustrates the deposited charge.

6.4 Discussion

A 2-pt correlation function was applied to a three-year datasample. The results of this search are consistent with background expectations with a small underfluctuation. Depending on the number of assumed sources, the resulting upper limits range from 10^{-8} GeV/cm^{2}s^{-1} for one source to 10^{-9} GeV/cm^{2}s^{-1} for 200 E^{-2} neutrino sources in the northern hemisphere. Limits were also set for other assumed energy spectra, including E^{-3} and $E^{-2.25}$ in the northern hemisphere. Since the analysis uses a data-driven background estimation is more robust against systematic uncertainties than estimations from MC simulations.
Considering the astrophysical flux previously observed in IceCube [16], a small number ($\leq$ 10) of isotropically distributed sources in the northern hemisphere of very hard energy spectra, like E^{-2}, is excluded as it was by former IceCube analyses [18]. For softer energy spectra, the analysis presented here disfavours the observed flux to come from less than $\sim$ 20 sources for $E^{-2.25}$ and from less than $\sim$ 5000 sources for E^{-3}.

Additionally, for sources distributed along the galactic plane in the northern hemisphere the autocorrelation limit is close to the flux predicted by HESE. In the southern hemisphere, the data sample contains predominantly atmospheric muons from cosmic ray air showers above the detector. Due to this background the autocorrelation analysis is not sensitive to a population of sources at the HESE flux level. For all these tests, the sources are assumed to have the same flux at Earth, since the true spatial flux distribution is not known for the observed astrophysical flux. For hard energy spectra, the 2-pt correlation analysis is more sensitive than the multipole analysis since it uses the energy information as an additional variable.

In addition a 2-pt analysis is applied to the 100 most energetic events in the IC79 sample to study the highest energetic events in more detail. The results yielded one high-energetic pair of events just above the horizon. However, the p-value for this observation is not significant.

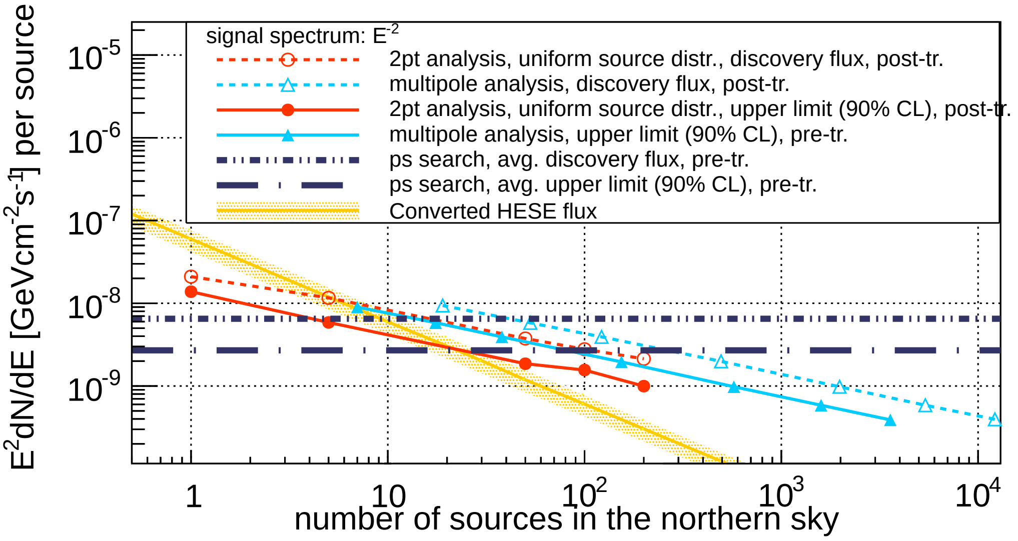

(a) Discovery potential and limits for the northern sky

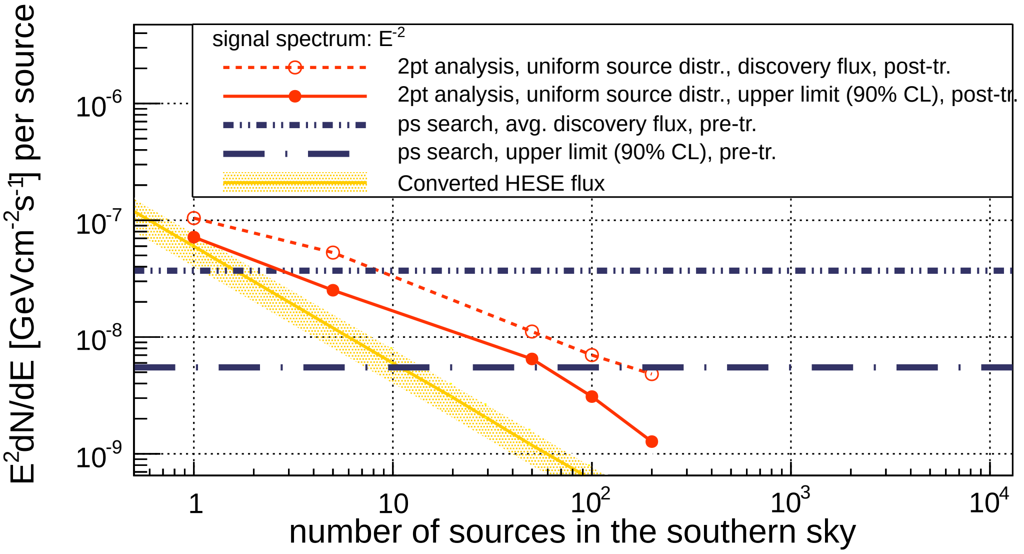

(b) Discovery potential and limits for the southern sky

Figure 6.6.: Discovery potential and upper limits for uniform E^{-2} neutrino sources for the autocorrelation analysis and the multipole analysis (a) on the northern hemisphere and (b) on the southern hemisphere. They are compared to the discovery potential of the point source search [18]. The yellow band corresponds to the converted flux of the HESE analysis [16].

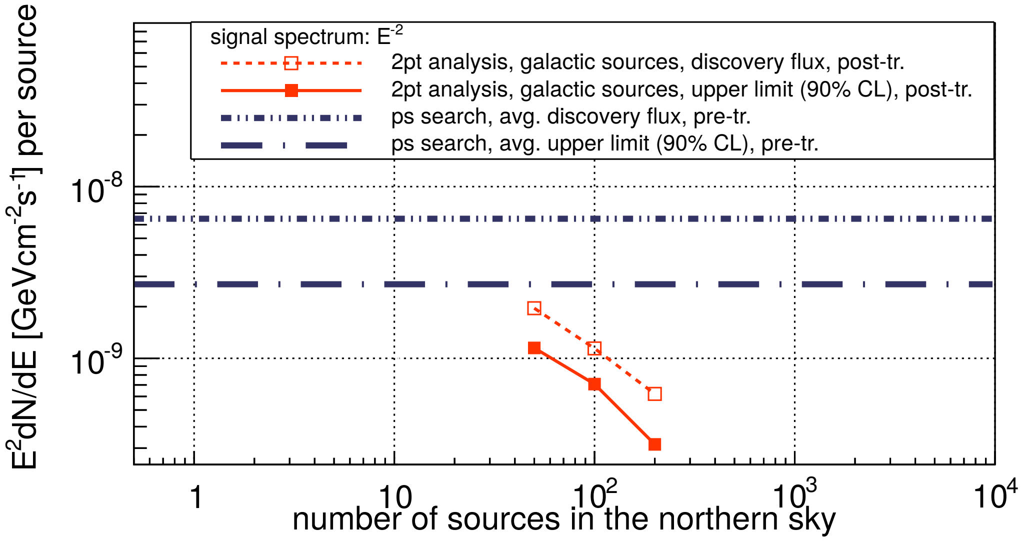

(a) Discovery potential and limits for the northern sky

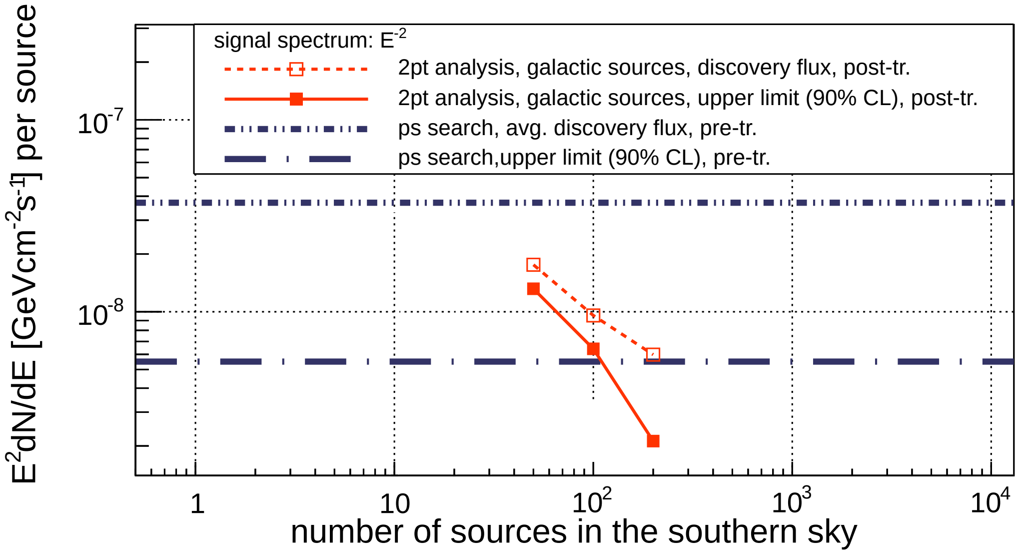

(b) Discovery potentials and limits for the southern sky

Figure 6.7.: (a) The discovery potential and the upper limits for E^{-2} neutrino sources, distributed in the galactic plane with the autocorrelation analysis (a) for the northern hemisphere and (b) for the southern hemisphere. They are compared to the discovery potential of the point source search [18].

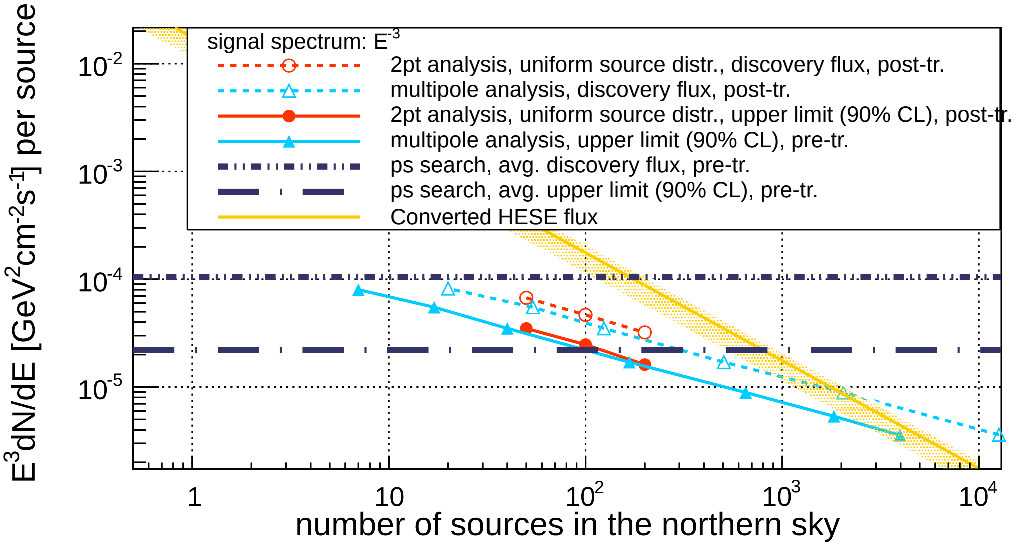

(a) Discovery potential and limits for E^{-3}

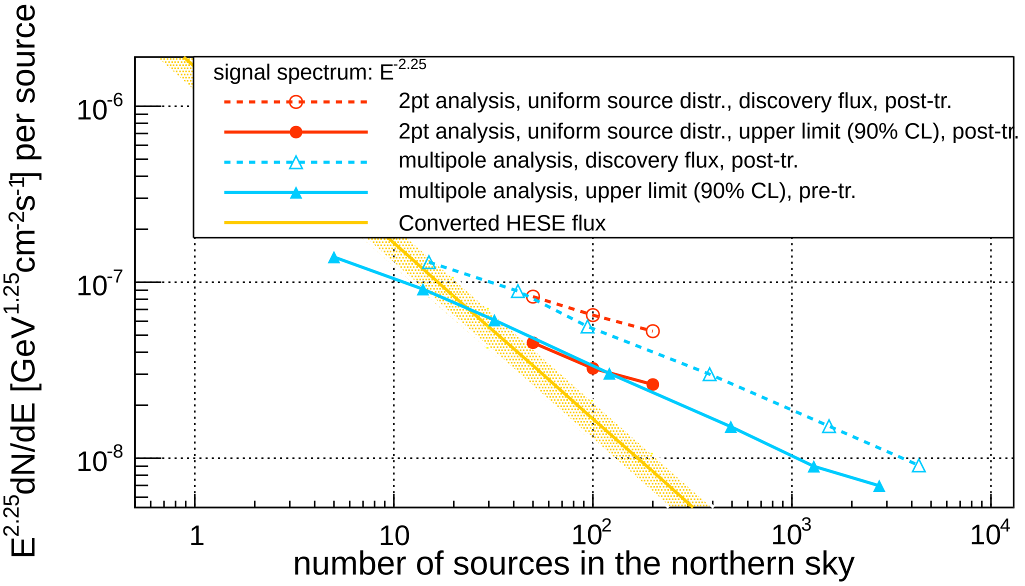

(b) Discovery potential and limits for $E^{-2.25}$

Figure 6.8.: (a) The discovery potential and upper limits (a) for E^{-3} neutrino sources and (b) for $E^{-2.25}$ neutrino sources with the autocorrelation analysis and the multipole analysis for the northern hemisphere. They are compared to the discovery potential and the upper limit of the point source search [18]. Additionally, the converted flux from the HESE analysis is shown [16].

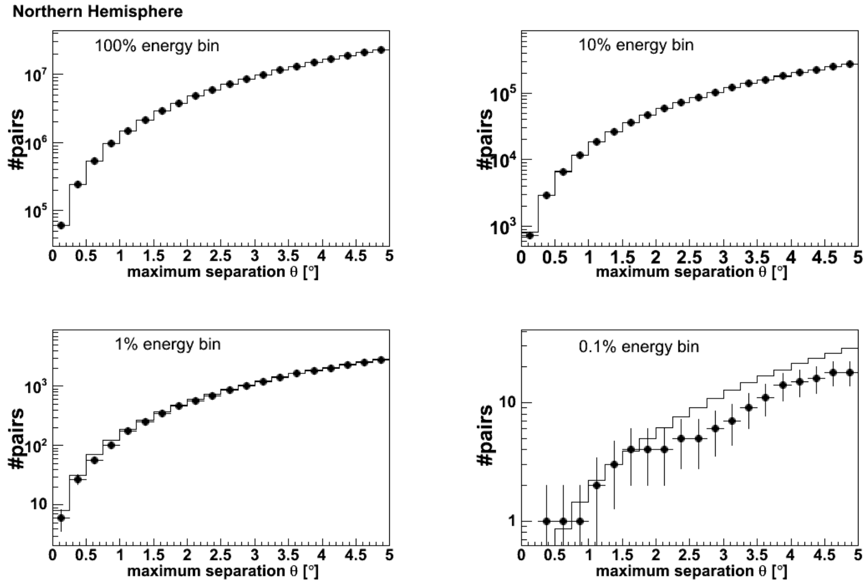

Figure 6.9.: Result for the 2-pt analysis for the northern hemisphere as a function of the clustering scale θ. The black points refer to the observed number of pairs, while the black line represents the average number of background pairs.

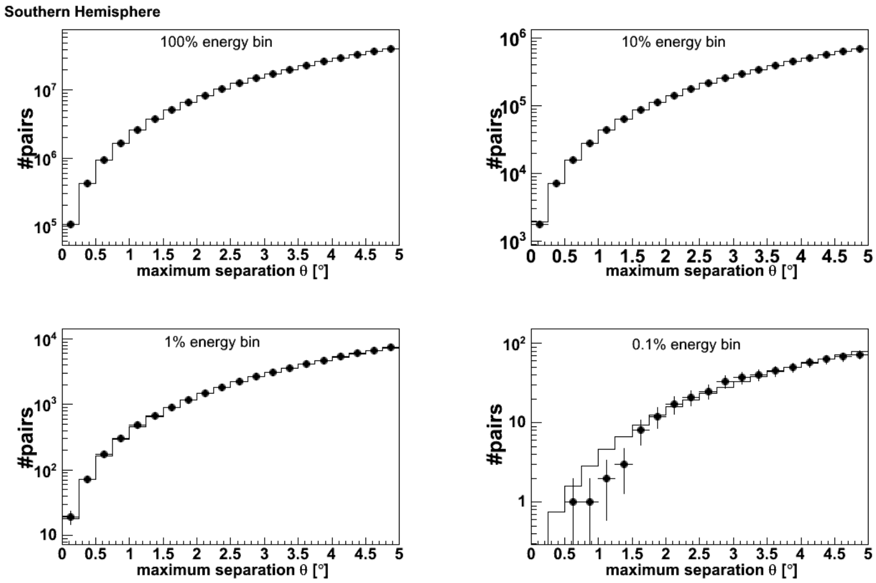

Figure 6.10.: Result for the 2-pt analysis for the southern hemisphere as a function of the clustering scale θ. The black points refer to the observed number of pairs, while the black line represents the average number of background pairs.

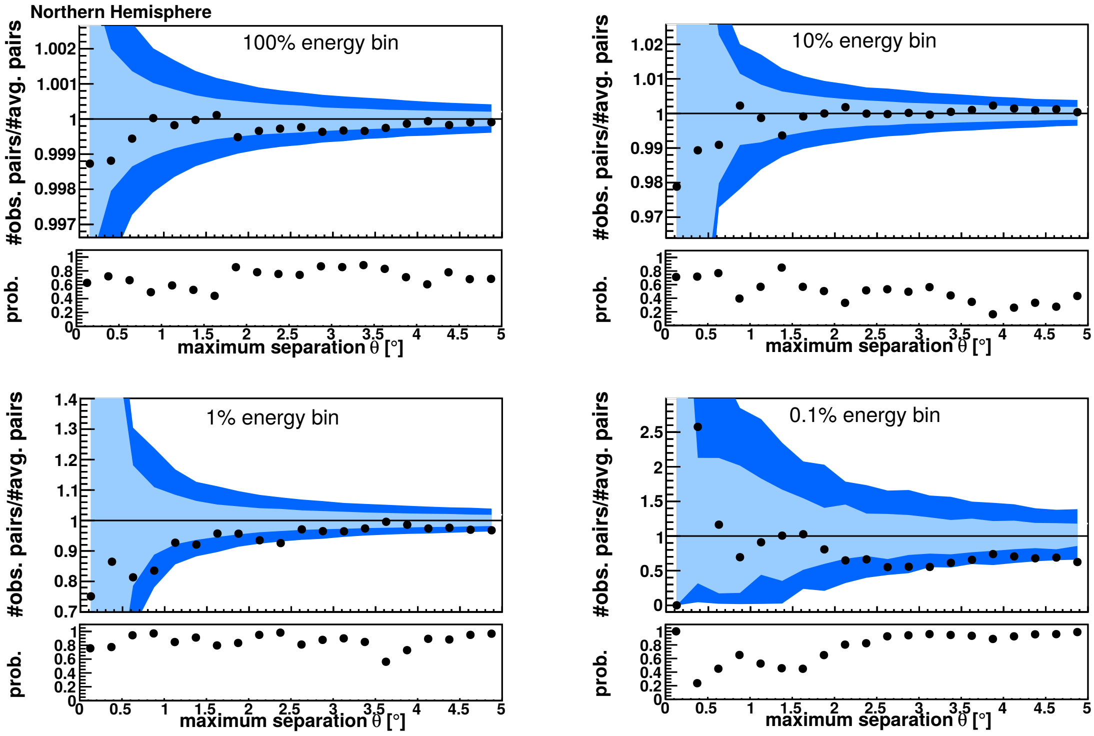

Figure 6.11.: Results for the 2-pt analysis on the northern hemisphere. In each plot, the upper panel shows the ratio of the number of observed pairs and the average number of background pairs, with the $+1\sigma$ and -1 σ (light blue), as well as the $+2\sigma$ and -2σ (dark blue) contours as a function of the clustering scale θ. The lower panel shows the probability before trials. The best p-value for the northern hemisphere is 0.16 and is found at $\theta < 4°$ in the highest-energy 10 % selection. The final p-value after correcting for trials is 0.84.

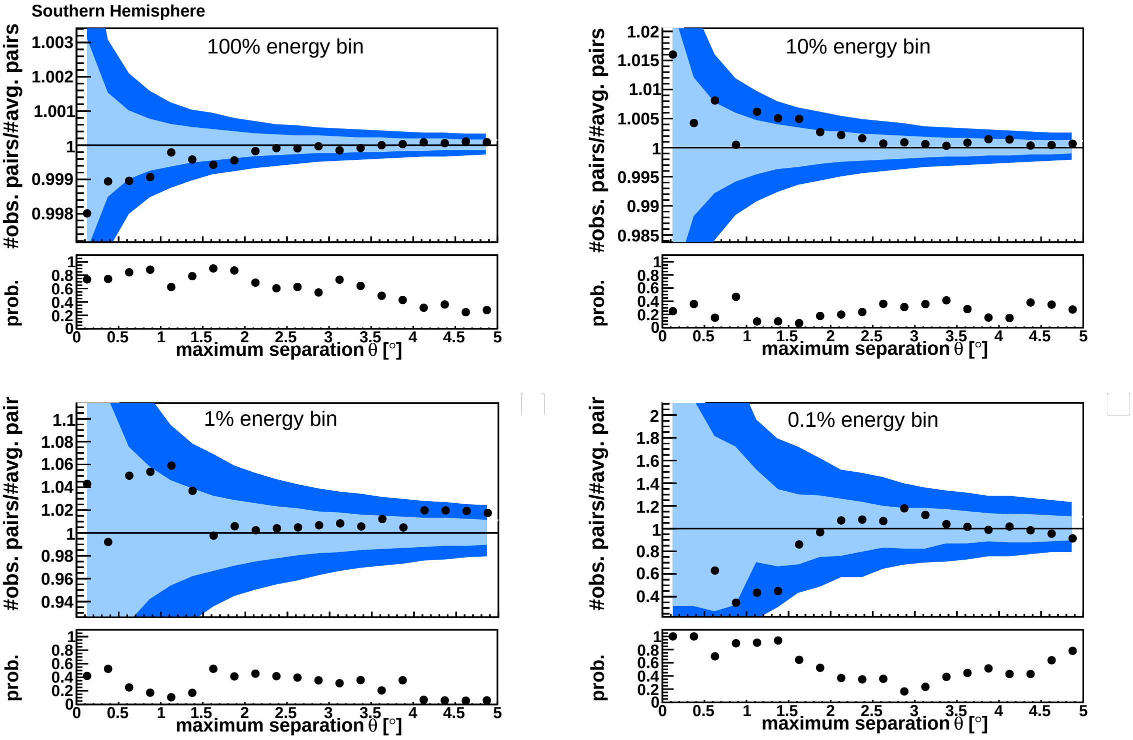

Figure 6.12.: Results for the 2-pt analysis for the southern hemisphere. For each plot, the upper panel shows the ratio of the number of observed pairs and the average number of background pairs, with the $+1\sigma$ and -1σ (light blue), as well as the $+2\sigma$ and -2σ (dark blue) contours for the clustering scale θ. The lower panel shows the probability before trials. The best p-value for the southern hemisphere is 0.055 and is found at $\theta < 4.75°$ in the highest-energy 1 % selection. The final p-value after correcting for trials is 0.73.

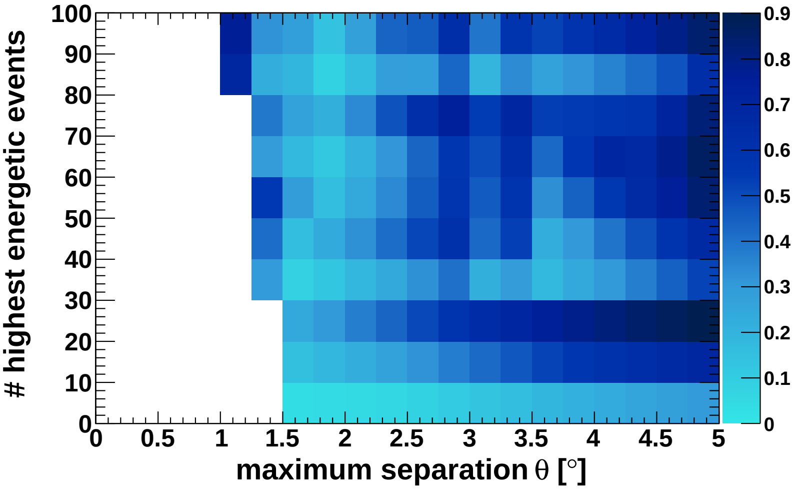

Figure 6.13.: Results of the additional high energy test of IC79 data. Shown are the pre-trial p-values as a function of the clustering scale θ and the number of highest energy events. The best pre-trial p-value of 0.035 is found at a distance of 1.57° inside the 10 events energy bin.

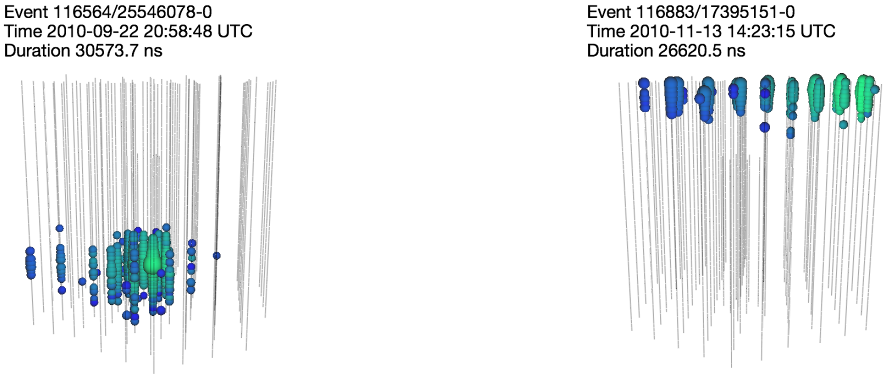

(a) Event 1

(b) Event 2

Figure 6.14.: Event views of the pair of events found in the IC79 High Energy Study. The colour indicates the time, going from green to blue, while the size of the spheres illustrates the deposited charge.

7

Energy-Weighted Multi Point Source Analysis of the Cygnus Region

The energy-weighted Multi Point Source (eMPS) method is an important addition to the standard search methods. It is applied to a 7° x 11° region of the Galactic Plane, which includes the most active parts of the Cygnus region. The method, as described in Sec. 5.4, aims to detect spatial clustering of events inside the region, in considering the energy of each event. It is sensitive not only to point sources, but also extended sources and can detect a possibly additional diffuse emission inside the region. The Cygnus region as a possible source for cosmic ray acceleration is motivated in detail in Sec. 2.4.1. The search was already performed several times on IceCube data. While in IC22 + AMANDA data [149] an overfluctuation of $2.3\,\sigma$ was observed, a strong underfluctuation of more than $-1\,\sigma$ was visible in IC40+AMANDA data [150] and in IC40+IC59+IC79 data [151]. This provided interest in performing the test on a even more sensitive 4-year datasample, consisting of IC40+IC59+IC79Spline+IC86 data. The tested region stayed the same, covering an area of 72° to 83° in galactic longitude and $-3°$ to 4° in galactic latitude, as indicated in Fig. 7.1 with an orange square. The angular scale goes from 0° to 5°, using a step size of 0.25°. The final p-value is obtained by taking the smallest observed p-value in any of the θ-bins, which gets corrected for the trials incurred by testing multiple values of θ. Since the test statistic is cumulative, the bins are highly correlated and the effective number of trials is less than the number of bins.

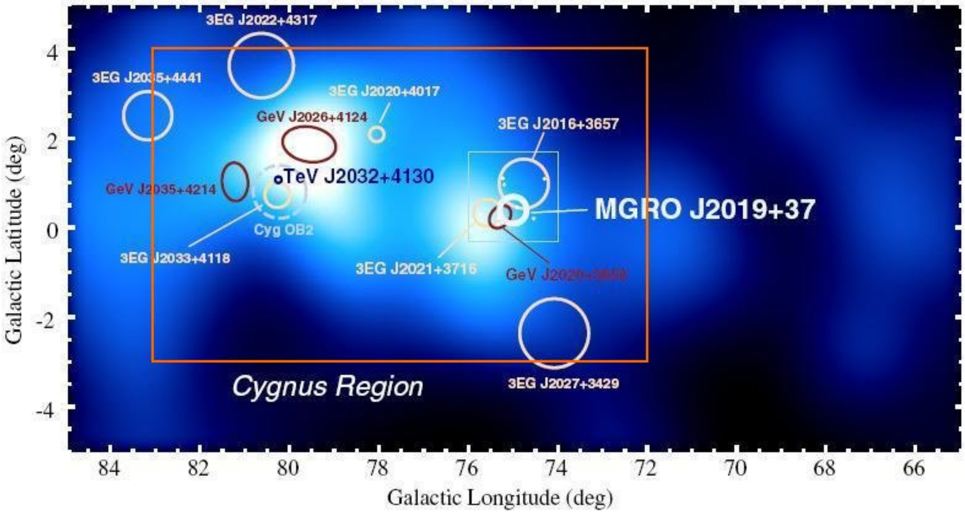

Figure 7.1.: Diffuse emission and point sources in the Cygnus region measured by EGRET. The orange square represents the search area for the eMPS. Picture taken from [155]

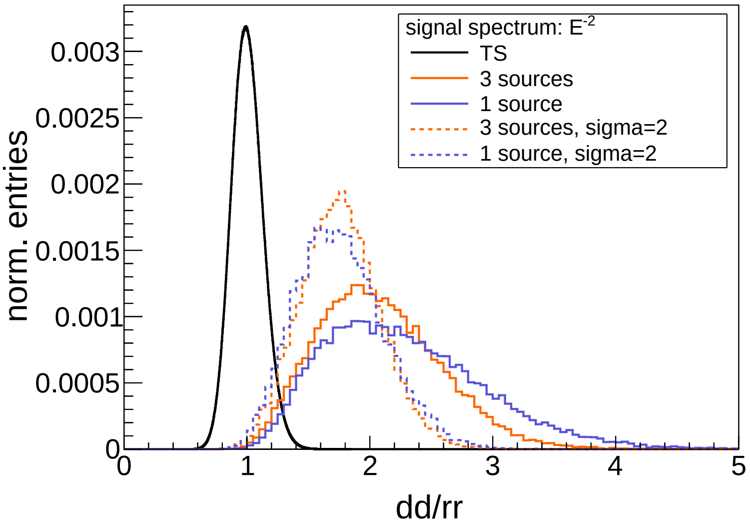

Figure 7.2.: Test statistic for background (black) and different signal models with $\theta = 0.25°$ considering a E^{-2} neutrino spectrum. The blue line indicates one additional point source, the orange line three point sources. The dashed blue and orange lines show the test statistic for one and three extended sources with a width of $\sigma = 2$.

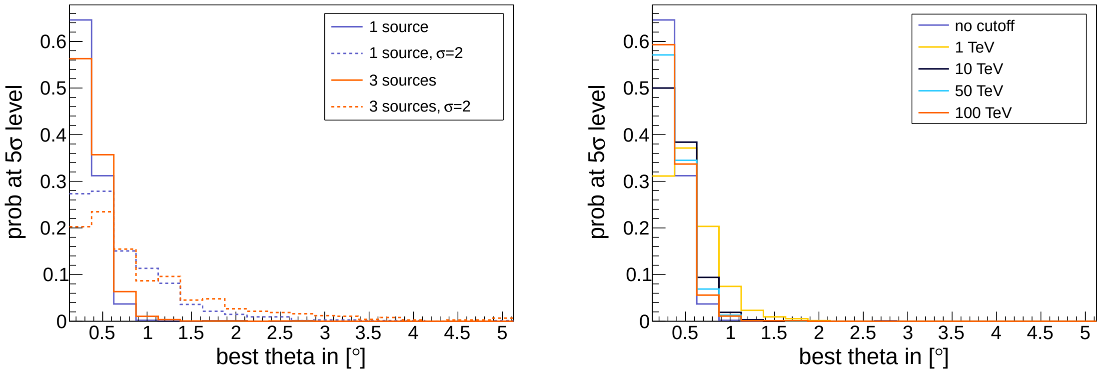

(a) Best clustering bin E^{-2} spectrum

(b) Best clustering bin E^{-2} spectrum with different cutoffs

Figure 7.3.: (a) Preferred clustering bin for different number of point (straight) and extended (dashed) sources for a E^{-2} spectrum. (b) Preferred clustering bin for point sources for a E^{-2} spectrum with different cutoffs.

7.1 Application to the Data: Discovery Potential

The eMPS was applied to the 4-year datasample in performing 10^7 pseudo-experiments on randomized experimental data from the same declination band as the search region. The randomization is done in assigning a random right ascension to each event, while the declination and energy are taken from data. The event energy weights $W(E_i)$ are derived from the observed data. In dividing the data into five declination bands, the energy-dependence of the background is ensured.
Figure 7.2 shows the test statistic for background and different signal models with $\theta = 0.25°$ considering a E^{-2} neutrino spectrum. The blue line represent one additional point source, while the orange line indicates three injected point sources. The dashed blue

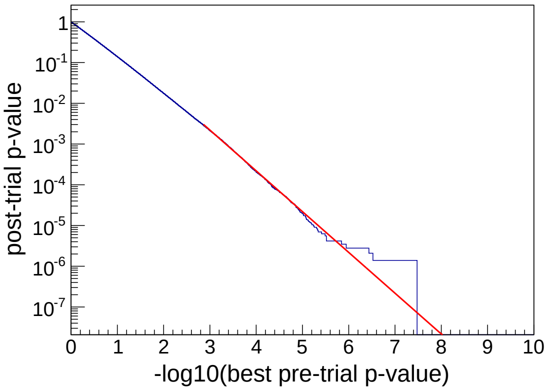

Figure 7.4.: Distribution of scrambled trials including an exponential fit for small p-values.

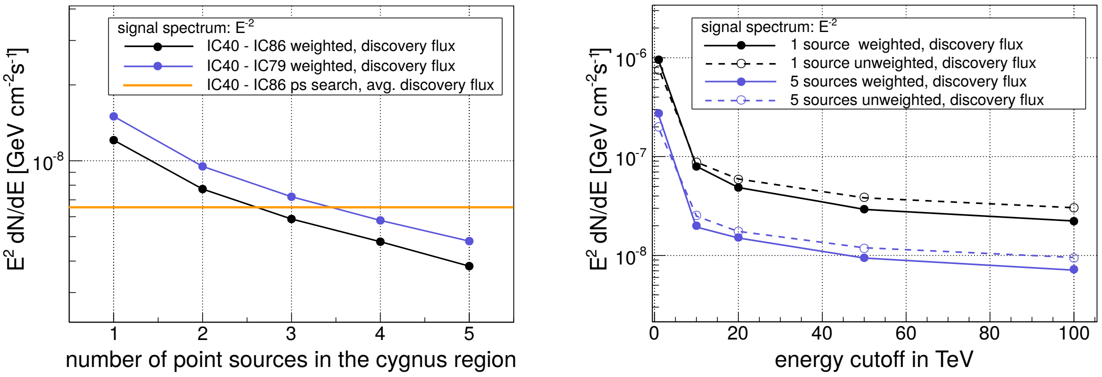

(a) Discovery potential

(b) Discovery potential

Figure 7.5.: (a) Discovery potential as a function of the number of point sources in the search region for a E^{-2} neutrino energy spectrum. For comparison the eMPS analysis on the three year data sample (blue) and the average discovery flux of the four year point source search (orange) are shown. (b) Discovery potential as a function of an additional exponential cutoff ($e^{E/TeV}$) in the E^{-2} neutrino energy spectrum for one (black) and five (blue) sources. The dashed lines show the discovery potential without energy weights.

and orange lines show the test statistic for one and three extended sources with a width of $\sigma = 2$, respectively. For point sources the best clustering is seen at small clustering scales, while for extended sources the effect increases on larger scales. Additional material showing the best clustering bins for different numbers of sources and additional diffuse events can be found in Fig. A.2 of the appendix.

For evaluating the best clustering bin, i.e. the bin that is most sensitive to a certain signal scenario, it is counted for each trial, how often the global p-value falls into the specific θ bin. This is shown in Fig. 7.3(a) for different number of point and extended sources for a E^{-2} spectrum. It can be seen that for point sources smaller θ bins are preferred, while for extended sources the peak is shifting to larger values of θ. In Fig. 7.3(b), the same distribution is shown for a $E^{-2} \cdot e^{E/TeV}$ spectrum with different exponential energy cutoffs in TeV. For an unbroken E^{-2} spectrum and high cutoffs the clustering favours again small values of θ, while for softer spectra the larger θ are preferred. This shows that the analysis is sensitive to all kind of spectra and can simplify the interpretation of a possible signal.

The correction for trials in the analysis is done via the scrambled trials approach. For that, the probability of obtaining a p-value larger than the p-value from the distribution of p-values from 10^7 pseudo-experiments on background-only data is evaluated. However, for the estimation of the discovery potential p-values in the order $\sim 10^{-7}$ are needed. To avoid problems with the low statistics at that level, a fit is applied to the data, as can be seen on Fig. 7.4. With this construction the trial-correction can be done. Instead of correcting each p-value itself, the probability value for the $5\,\sigma$ discovery potential ($10^{-6.5}$) is corrected once to $10^{-7.04}$ and used in each discovery potential calculation.

The $5\,\sigma$ discovery potential for the eMPS is calculated correspondingly to the 2-pt, as described in Sec. 5.6.1. Figure 7.5(a) shows the discovery potential as a function of the number of neutrino point sources inside the search region. It is compared to the discovery flux of the three year eMPS analysis and the average discovery flux of the standard point source search in the same datasample. As expected, the discovery flux per source decreases with the number of sources inside the region. The improvement with respect to the three year analysis lies at ~20% and more than 45% compared to the original MPS. At three sources the discovery flux of the eMPS crosses the average discovery flux in that declination band of the standard point source search. However, the discovery fluxes for the eMPS are fully corrected for the trials, while the point source search is not corrected for trials, induced by testing a grid of locations on the whole northern hemisphere. Since there was no significant result *obtained* from the standard point source search, it excludes that the analysis of the Cygnus region observes a single E^{-2} source at a flux of $1.2 \cdot 10^{-8}\mathrm{GeV cm^{-2} s^{-1}}$. Since the eMPS is also sensitive to multiple point or extended sources or even diffuse emission, it is able to identify neutrino signal that the standard point source search can not detect.

In Fig. 7.5(b) the discovery potential of the eMPS is shown as a function of an additional exponential energy cutoff in the E^{-2} neutrino energy spectrum for one and five point sources. All sources were simulated with the same strength. The filled points show the additional improvement in using energy weights, while the open points do not use any energy-weighting. Up to a cutoff of ~5 TeV, the energy weighting improves the sensitivity, only for very soft spectra the discovery potential without weighting gets better. Accordingly, the discovery potential for five point sources is better than for only one injected source. Supplementary scenarios of the discovery potential for different source extensions and additional diffuse events were tested and can be found in the appendix, see Fig. A.3.

7.2 Results

The eMPS was applied on the four year dataset. The best p-value of 0.68 was found in $\theta < 4.75°$. After trial correction the final p-value results in 0.72. The results are shown in Fig. 7.6 as a function of the clustering scale θ. The upper panel shows the ratio of the number of observed pairs and the average number of background pairs, together with the $+1\sigma$ and -1σ, as well as the $+2\sigma$ and -2σ contours. The lower panel shows the probability before trial correction. Less events than expected have been observed in this region, meaning that the events are less clustered than on average in the background. The values for the ratio of the measured results to the average background lie all below one at all clustering scales θ. The results are consistent with background and with the results of a stacking analysis of neutrinos events near Milagro sources [139].

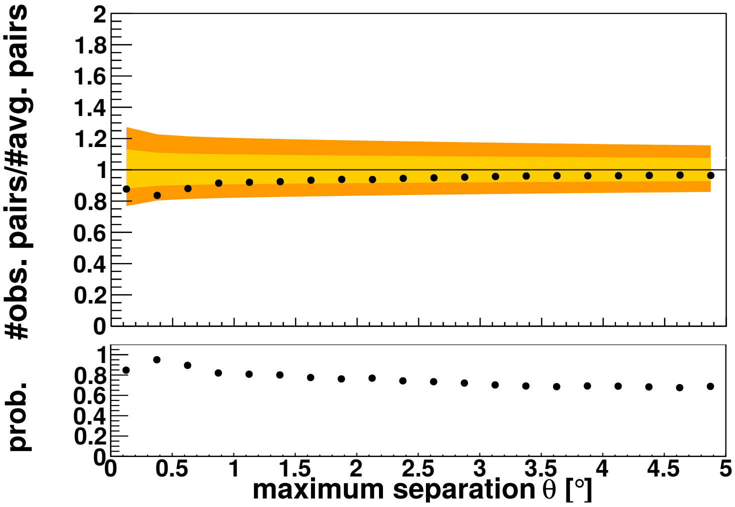

Figure 7.6.: Results of the eMPS search on the Cygnus region. The upper panel shows the ratio of the number of observed pairs and the average number of background pairs, with the $+1\sigma$ and -1σ (yellow), as well as the $+2\sigma$ and -2σ (orange) contours for the clustering scale θ. The lower panel shows the probability before trials. The best p-value is 0.68 and is found at $\theta < 4.75°$. The final p-value after correcting for trials is 0.72.

7.3 Neutrino Upper Limits

The eMPS method can profit from different kinds of neutrino emission. As discussed in Sec. 2.4.1, the matter distribution follows strongly the clustering of star clusters and associations. High-energy protons can produce neutrinos in interacting close to their source or they diffuse into the medium until they interact, where the resulting neutrinos can not be associated to their source of origin and can be assumed as diffuse. The sensitivity of the eMPS ranges between a purely diffuse case and a maximum clustered case, where all events are coming from one point source [156]. From gamma-ray observations of Milagro it can be considered that the most likely case is probably a combination of a few point sources and a diffuse component.

As a result of the underfluctuation, strong limits can be derived using the 90% Neyman approach [154]. In this case, limits are calculated for different numbers of point sources and an additional diffuse component. They are estimated for an E^{-2} and $E^{-2.6}$ neutrino spectrum at 1 TeV, corresponding to the measured flux inside the region. The resulting limits for one, two and four sources are shown in Fig. 7.7(a) and 7.7(b). They are compared to the flux of the two strongest objects MGRO J2019+37 and MGRO J2031+41 inside the region measured by Milagro [68, 67].

7.4 Discussion

The eMPS method was applied to a four year data sample of IceCube data. With respect to the three year analysis an improvement of 20% in discovery potential was achieved. The final p-value results in a pre-trial p-value of 0.68 and is found at $\theta < 4.75°$. The final p-value after correcting for trials is 0.72, meaning that less pairs are observes than on average in the background. Due to the observed underfluctuation strong limits can be set. They range from E^2 dN/dE = 4 $\cdot 10^{-12}$TeVcm^{-2}s^{-1} for one source without additional diffuse flux to E^2 dN/dE = 3 $\cdot 10^{-10}$TeVcm^{-2}s^{-1}sr^{-1} for four sources with a diffuse component. For a $E^{-2.6}$ spectrum the values go from $E^{2.6}$ dN/dE = 1.8 $\cdot 10^{-11}$TeV$^{1.6}$cm^{-2}s^{-1} for one source and $E^{2.6}$ dN/dE = 2.5 $\cdot 10^{-11}$TeV$^{1.6}$cm^{-2}s^{-1}sr^{-1} for four sources with a diffuse component. In order to compare these limits to gamma ray measurements different assumptions need to be considered.

Assuming the gamma ray Milagro flux comes from pp interactions, it can be transferred into neutrinos fluxes with a conversion factor of ~3.4 for a $E^{-2.6}$ spectrum, according to [55]. In taking the average of the two Milagro sources the final limit results in $E^{2.6}$ dN/dE = 3.8 $\cdot 10^{-12}$TeV$^{-1.6}$cm^{-2}s^{-1}. For the diffuse flux the limit results in $E^{2.6}$ dN/dE = 5.56 $\cdot 10^{-10}$TeV$^{1.6}$cm^{-2}s^{-1}sr^{-1}. The combined value of two sources plus a diffuse component lies approximately in the same range as the limit by the eMPS analysis, but not above. However, the diffuse flux of the Cygnus region taken from [67] suffers large uncertainties. Other calculations [157] suggest a much lower diffuse flux from pp interactions of background cosmic rays in the order of $\sim 1 \cdot 10^{-10}$TeV$^{-1.6}$cm^{-2}s^{-1}sr^{-1}, in which the eMPS limits are still far from constraining.

In future applications of the eMPS test, more statistics in terms of more years of IceCube data will be available and it might be possible to constrain the gamma ray flux of the Cygnus region. However, HAWC, the successor of Milagro, may be able to provide more detailed information about the processes and objects inside the Cygnus region and produce more exact values for the gamma ray fluxes.

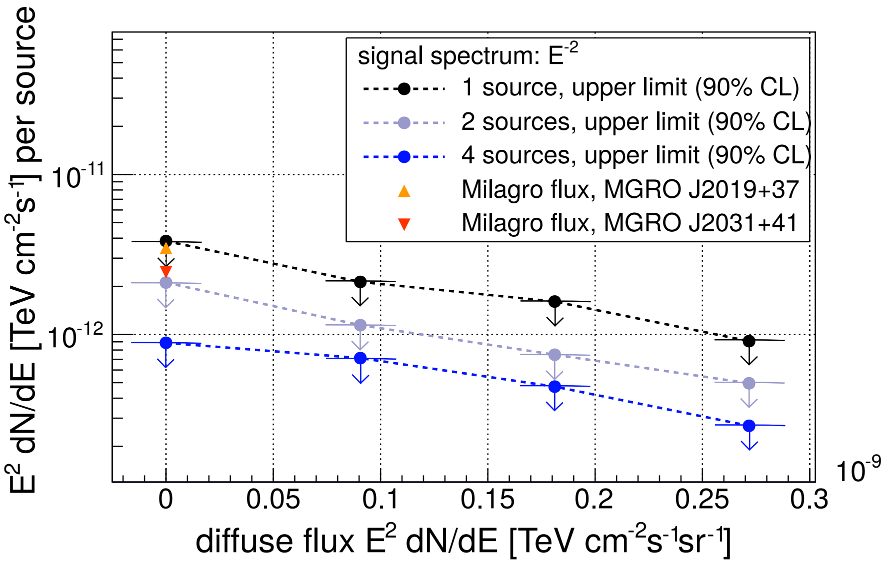

(a) Limits for a E^{-2} spectrum

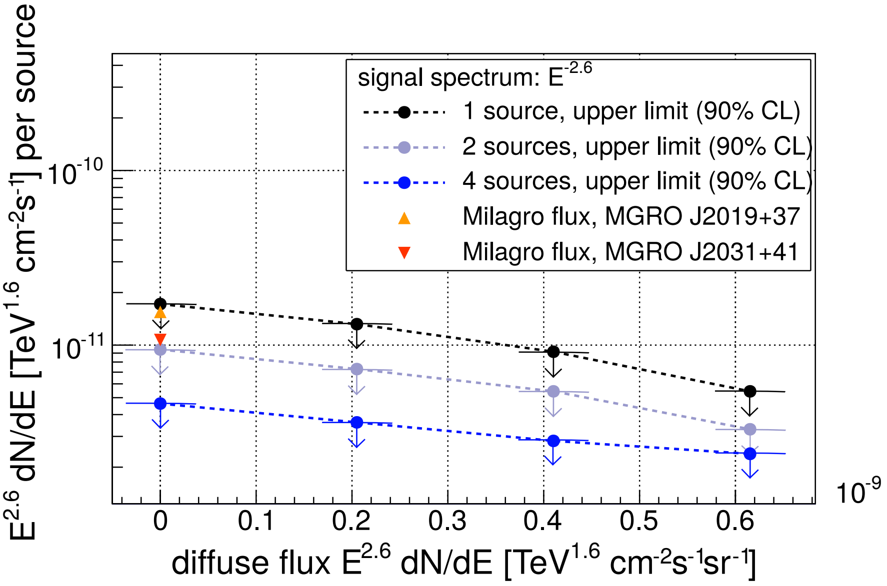

(b) Limits for a $E^{-2.6}$ spectrum

Figure 7.7.: (a) Limits of the eMPS search for a E^{-2} spectrum at 1 TeV. Shown are one, two and four point sources without and with additional diffuse component. The fluxes are compared to the fluxes of the two strongest objects inside the region, MGRO J2019+37 and MGRO J2031+41, measured by Milagro [68, 67]. (b) Limits of the eMPS search for a $E^{-2.6}$ spectrum at 1 TeV. Shown are one, two and four point sources without and with additional diffuse component. The fluxes are compared to the fluxes of the two strongest objects inside the region, MGRO J2019+37 and MGRO J2031+41.

8

Self Triggered Flare Search

The high energy neutrinos detected by IceCube in the High Energy Starting Events (HESE) analysis [15] could provide valuable information about potential astrophysical cosmic ray sources and motivate additional searches for their origin. Since the flux from this analysis is assumed to be diffuse, it is not clear if these events can be resolved into point sources. A likelihood point source search on the HESE events showed no significant clustering 8.1. The self-triggered flare search uses the events obtained in the HESE analysis to trigger a search for flaring point sources, that can be attributed to those events. In that search, different event selections are combined, taking advantage of both, the large effective area of the point source sample and the high signal rate in the HESE sample. In this approach the HESE events are used as a trigger for the point source sample and a search for an excess in temporal and in spatial coincidence to the HESE events is performed.

Each of the HESE event functions thereby as a seed, constructing a search region, centred around the reconstructed position of the event, which is defined by the median of the angular reconstruction error of each individual HESE event. In this way, both, tracks and cascades of the HESE search can be used as a seed. An overview of the 28 events obtained in the HESE search is shown in galactic coordinates in Fig. 8.1. Cascades are represented as circles with their individual median angular reconstruction error ($\Psi_{0.5}$) shown as a black line, while tracks are shown as squares with small errors. As discussed in section 5.1.1, cascades have large errors on their angular reconstruction, but a good energy resolution. Tracks, however, have a good pointing, but the energy reconstruction is worse than for cascades, since not all energy is deposited inside the detector. Since a bad median angular resolution $\Psi_{0.5}$ seems to add more background than signal, cascades with errors $> 20°$ are not considered in the search and reduces the events from the HESE search that are used in this analysis to 24. The obtained parameters of the events of the HESE search are shown in detail in Tab. 8.1. Events 2,

7, 21 and 25 are not considered in this analysis, due to their large angular reconstruction errors.
The method applied in this search is the extended eMPS method, described in Sec. 5.5. Here, the eMPS is used as a base and extended by a search for time clustering and a stacking approach in evaluating the cumulative signal of several HESE events. The binning of the angular scale goes up to 2.5° in steps of 0.5° and is done accordingly to the eMPS analysis, as well as the energy weights are included. The time-dependency is achieved in using five additional time bins, similar to the energy bins in the 2-pt analysis. The bins used here consider flare durations of 1, 2, 6, 12 and 20 days. The stacking of several similar sources is a widely used technique in gamma ray and optical astronomy and was applied already several times on IceCube data [139]. In using the cumulative signal of sources from the same source class the sensitivity can be enhanced.

8.1 Background Estimation

In the analyses presented before, the background estimation is done in using isotropic background from data, which is filled with randomly generated values in right ascension. Since the self-triggered flare analysis is searching not only for spatial clustering, but also temporal, the events need to be randomized in their arrival times. This is done in drawing randomized arrival times during the uptime of the detector, while the detector uptime for each year is used separately. In a second step, the randomized times get transformed into equatorial coordinates, producing random values for the right ascension. The declination is taken from data.

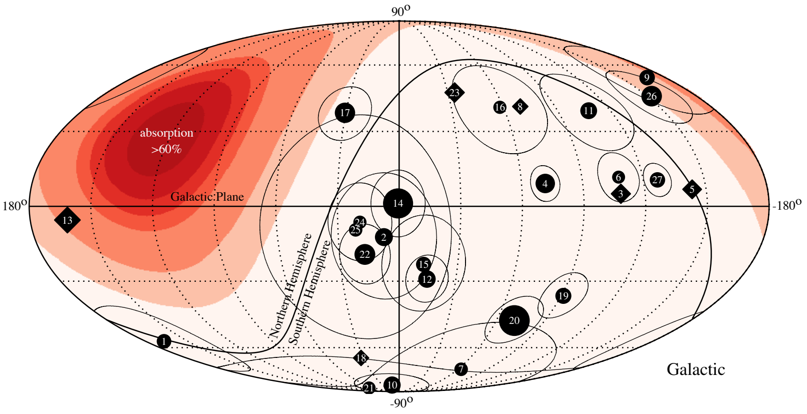

Figure 8.1.: The HESE events found in the 2-year analysis, shown as tracks (squares) and cascades (circles) in galactic coordinates. In addition, the median of the individual reconstruction error of the cascades is shown as a circle around each position, while the size of each symbol represents the energy. The red-shaded area symbolizes the earth absorption. Plot from M. Ahlers.

Event	Time [MJD]	Dec [°]	RA [°]	$\Psi_{0.5}$	Dep. Energy [TeV]	Topology
1	55351.3222110	−1.8	35.2	16.31	$47.6^{+6.5}_{-6.4}$	Shower
(2)	55351.4659612	−27.9	282.6	25.4	$117.0^{+15.4}_{-14.6}$	Shower
3	55451.0707415	−31.2	127.9	$\lesssim 1.38$	$78.7^{+10.8}_{-8.6}$	Track
4	55477.3930911	−51.2	169.5	7.10	$165.4^{+19.8}_{-14.9}$	Shower
5	55512.5516214	−0.4	110.6	$\lesssim 1.17$	$71.4^{+9.0}_{-9.0}$	Track
6	55567.6388084	−27.2	133.9	9.78	$28.4^{+2.7}_{-2.5}$	Shower
(7)	55571.2585307	−45.1	15.6	24.05	$34.3^{+3.5}_{-4.3}$	Shower
8	55608.8201277	−21.2	182.4	$\lesssim 1.31$	$32.6^{+10.3}_{-11.1}$	Track
9	55685.6629638	33.6	151.3	16.52	$63.2^{+7.1}_{-8.0}$	Shower
10	55695.2730442	−29.4	4.9	8.07	$97.2^{+10.4}_{-12.4}$	Shower
11	55714.5909268	−8.9	155.3	16.67	$88.4^{+12.5}_{-10.7}$	Shower
12	55739.4411227	−52.8	296.1	9.82	$104.1^{+12.5}_{-13.2}$	Shower
13	55756.1129755	40.3	67.9	$\lesssim 1.20$	$252.7^{+25.9}_{-21.6}$	Track
14	55782.5161816	−27.9	265.6	13.23	$1040.7^{+131.6}_{-144.4}$	Shower
15	55783.1854172	−49.7	287.3	19.69	$57.5^{+8.3}_{-7.8}$	Shower
16	55798.6271191	−22.6	192.1	19.45	$30.6^{+3.6}_{-3.5}$	Shower
17	55800.3755444	14.5	247.4	11.56	$199.7^{+27.2}_{-26.8}$	Shower
18	55923.5318175	−24.8	345.6	$\lesssim 1.31$	$31.5^{+4.6}_{-3.3}$	Track
19	55925.7958570	−59.7	76.9	9.71	$71.5^{+7.0}_{-7.2}$	Shower
20	55929.3986232	−67.2	38.3	10.70	$1140.8^{+142.8}_{-132.8}$	Shower
(21)	55936.5416440	−24	8.9	20.93	$30.2^{+3.5}_{-3.3}$	Shower
22	55941.9757760	−22	293.7	12.10	$219.5^{+21.2}_{-24.4}$	Shower
23	55949.5693177	−13.2	208.7	$\lesssim 1.94$	$82.2^{+8.6}_{-8.4}$	Track
24	55950.8474887	−15.1	282.2	15.52	$30.5^{+3.2}_{-2.6}$	Shower
(25)	55966.7422457	−14.5	286	46.28	$33.5^{+4.9}_{-5.0}$	Shower
26	55979.2551738	22.7	143.4	11.85	$210.0^{+29.0}_{-25.8}$	Shower
27	56008.6845606	−12.6	121.7	6.62	$60.2^{+5.6}_{-5.6}$	Shower
28	56048.5704171	−71.5	164.8	$\lesssim 1.30$	$46.1^{+5.7}_{-4.4}$	Track

Table 8.1.: Events obtained in the HESE analysis and their individual reconstruction parameters [15]. Considered in the self-triggered flare search are only events with a median angular resolution $\Psi_{0.5} > 20°$, i.e. event 2, 7, 21 and 25 are not used.

For the background test statistic 100 000 pseudo-experiments are performed on the randomized data. For the evaluation of the discovery potential, the background test statistic is extrapolated in fitting a Gamma function to the data. The background test statistic and the Gamma function are shown on Fig. 8.2 for an angular scale $\theta = 2°$ and different flare durations, varying between 2 and 20 days.

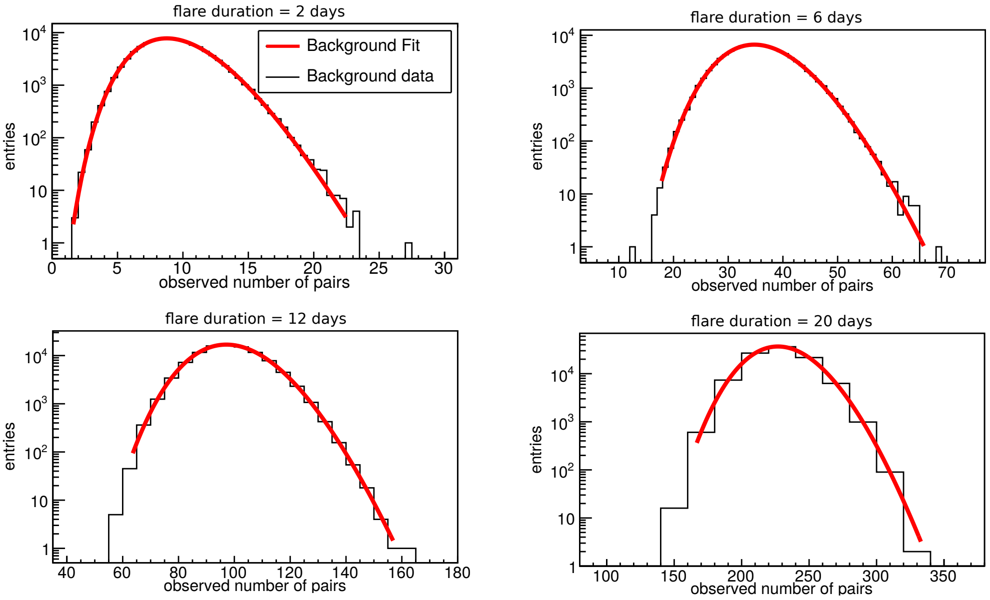

Figure 8.2.: Background test statistic fitted by a Gamma function for an angular scale $\theta = 2°$ and different flare durations.

8.2 Signal Simulation

For simulating the signal, it is assumed that a fraction of the HESE events is caused by short-duration flares. This fraction with respect to the total astrophysical flux of events gets parametrized with a variable called signal fraction (f_{sig}). This signal fraction f_{sig} defines the fraction of the HESE events attributed to flaring point sources, e.g. if $f_{sig} = 0.3$, $0.3 \cdot 24 \sim 7$ HESE events (allsky) are assumed to be related to a flaring point source. The signal skymaps produced for simulating the signal, depend on the signal fraction f_{sig}, the flare duration (τ_{flare}) and the spectral index (γ) of the simulated signal energy spectrum. In this search, two energy spectra are considered: a E^{-2} spectrum and a $E^{-2.3}$ spectrum , which is motivated by the HESE best fit with a $\gamma \sim 2.3$.
A skymap consisting of signal, depending on f_{sig}, τ_{flare} and γ, combined with background can then be generated by applying the following steps:

1. Decide in a hit-and-miss procedure, which HESE event is attributed to a flaring source, taking f_{sig} into account. For various iterations of the signal, the events which are attributed to a point source are not constant.

2. Draw the assumed true source location from a radial Gaussian $p \sim re^{-r^2/\sigma^2}$ centred at the measured HESE direction. The σ of that Gaussian is chosen in a way that its median agrees with the quoted resolution of the corresponding HESE event.

3. Assign a flare time according to τ_{flare} to the true source and weight it equally for

each source with 1/24 of the measured HESE flux ($\sim 0.95 \cdot 10^{-8} \mathrm{GeV cm^{-2} s^{-1} sr^{-1}}$). The flux is then concentrated in the assumed on-time of the flare.

4. Around each source, fill signal events from the same declination band, coming from MC simulation, until the flux is satisfied. The expectation value of the number of signal events injected at each source is then determined by folding the detector acceptance at the corresponding source declination by the assumed flux.
5. Merge data and signal events, while for each inserted signal event, a background event similar in declination and energy is erased. To ensure that not always the same background event is erased, all events get shuffled before.

For each signal scenario, 100 different true source positions according to the above mentioned parameters (f_{sig} and $\Psi_{0.5}$) are drawn. For each source, signal events according to Poissonian fluctuations are drawn 100 times for the assumed flux. By this a statistics of 10 000 for each considered scenario can be achieved.
While for a E^{-2} spectrum the flux obtained from the HESE best fit is $E^2\Phi(E) = 1 \cdot 10^{-8} \mathrm{TeV cm^{-2} s^{-1} sr^{-1}}$ at 100 TeV, it changes for an $E^{-2.3}$ spectrum to $E^{2.3}\Phi(E) = 1.5 \cdot 10^{-8} \mathrm{TeV^1 cm^{-2} s^{-1} sr^{-1}}$ at 100 TeV. This needs to be considered in the signal simulation, since the spectrum is then steeply falling and less signal is needed for discovery. To account for that, a lower flux assumption is used.

8.3 Performance and Discovery Potential

The test statistic is evaluated separately for each θ and τ_{flare} bin. As an example, Fig. 8.3 shows the observed number of pairs for $\theta = 2°$ and $\tau_{flare} = 2$ days with and without signal. The background test statistic is fitted with a Gamma function and compared to two signal models, with flux strengths of $f_{sig} = 0.2$ and $f_{sig} = 0.4$, considering a E^{-2} neutrino spectrum. In both cases the signal is clearly distinguishable from the background expectation.
However, the most sensitive bin i.e. which obtains the best clustering, varies with the simulated signal. In Fig. 8.4 the best clustering bin for different simulated τ_{flare} is shown for a E^{-2} neutrino spectrum. The simulated τ_{flare} are varied between 2, 10 and 20 days and are shown as functions of the angular scale θ and the flare bins. It can be seen, that short flares cluster in the shorter flare bins, while longer flares cluster in the long flares bin, which can be nicely distinguished by the analysis. All prefer small angular bins, which is due to the rather hard E^{-2} spectrum.
In order to find the optimal (i.e. most sensitive) configuration of the analysis, different scenarios are tested and their significance is calculated. Figure 8.5(a) shows the ratio of the events rate of events in the HESE and PS sample for a E^{-2} spectrum. It illustrates how many PS events can be expected for one HESE event. This ratio is high up to a declination of -20°, below that it decreases. From that considerations, two different cases were tested, the one covering the full sky, the second taking only the northern hemisphere plus the horizon region up to -20° into account. Figure 8.5(b) shows the

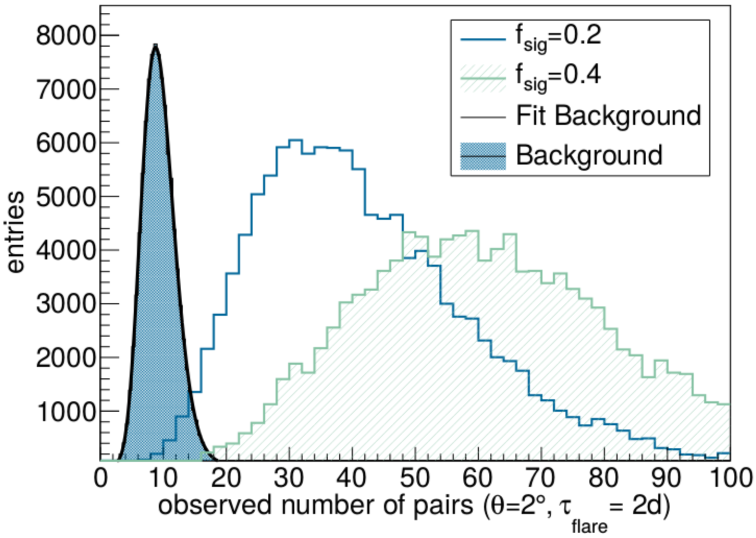

Figure 8.3.: Example test statistic, showing the observed number of pairs for simulated data sets with and without signal. The background test statistic is fitted with a Gamma function. The two signal models follow a distribution of E^{-2} neutrino sources and have flux strengths of $f_{sig} = 0.2$ and $f_{sig} = 0.4$.

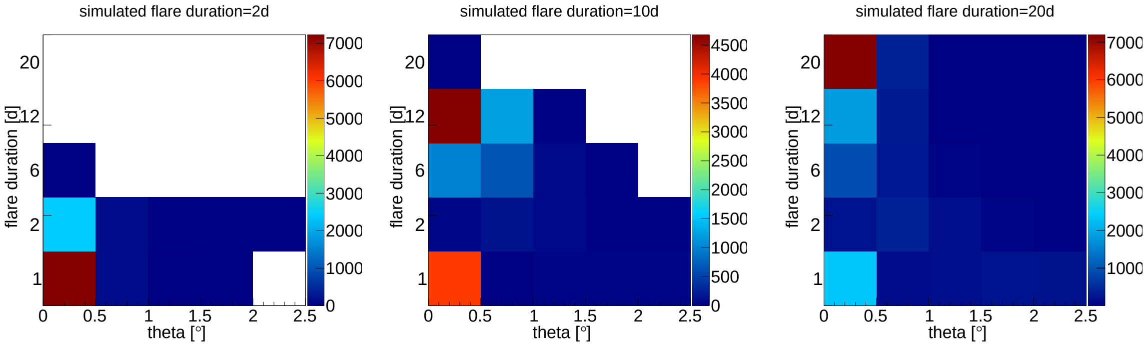

(a) $\tau_{flare} = 2$ days (b) $\tau_{flare} = 10$ days (c) $\tau_{flare} = 20$ days

Figure 8.4.: Best clustering bin for simulated flare durations τ_{flare} of (a) 2 days, (b) 10 days and (c) 20 days as functions of the angular scale θ and the flare bins, considering a E^{-2} neutrino spectrum. As expected, short flares cluster in the short flare bins, while longer flares cluster in the long flares bin.

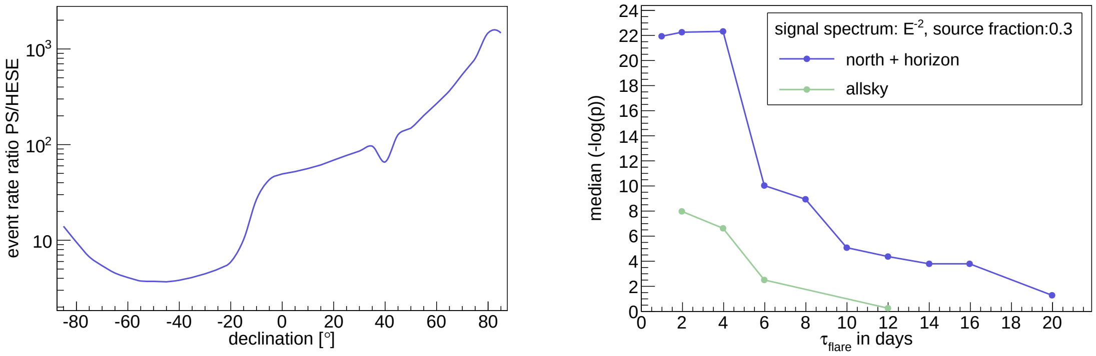

(a) Event rate ratio of HESE and PS sample

(b) Significances for the two senarios

Figure 8.5.: (a) Ratio of the event rate for the HESE and the PS sample as a function of the declination. In order to test a second scenario, a cut is made at a declination of -20°. (b) Significances of the allsky scenario and the second scenario, taking only the northern hemisphere plus the horizon region up to -20° into account.

significances as a function of τ_{flare} for both cases, considering a E^{-2} neutrino spectrum. The significance is given in the median of the log(p-value) distribution. For the allsky scenario the significance is much worse than for the second scenario. This is due to the high energy threshold in the southern hemisphere and the high rate of background.

Since most low energetic HESE events are assumed to consist of atmospheric muons or neutrinos, a better signal to background ratio is expected at higher energies. In order to test this assumption, a second optimization scenario cuts on the energy of the HESE events below 60 TeV. Again, 10 000 trials are produced for comparing the significance of this scenario with energy cut to the standard scenario without additional energy cut. It turned out, that the cut in energy does not increase the significance, but rather decreases it for low flare durations, where probably more signal than background is cut. The resulting graphs can be found in the appendix in Fig. A.4 and Fig. A.5(a).

The last scenario, which was tested in this work, is a slightly enlarged search radius for tracks. Since cascades have much larger search regions than tracks, it is likely they add more background than signal. To account for that, a scenario with an enlarged search region of +0.5° around each track-like event was tested and the significances compared, which can be found in Fig. A.5(b) of the appendix. Also this measure does not increase the significance of the analysis. In the end, the first tested scenario with an angular range up to -20° was used for the calculation the discovery potential and in the analysis.

Discovery Potential

The discovery potential is estimated as described in the previous searches. For that, the number of HESE sources contributing is varied in reducing or enlarging f_{sig} and thus, to reduce or enlarge the total flux. The test statistics for the different signal models is

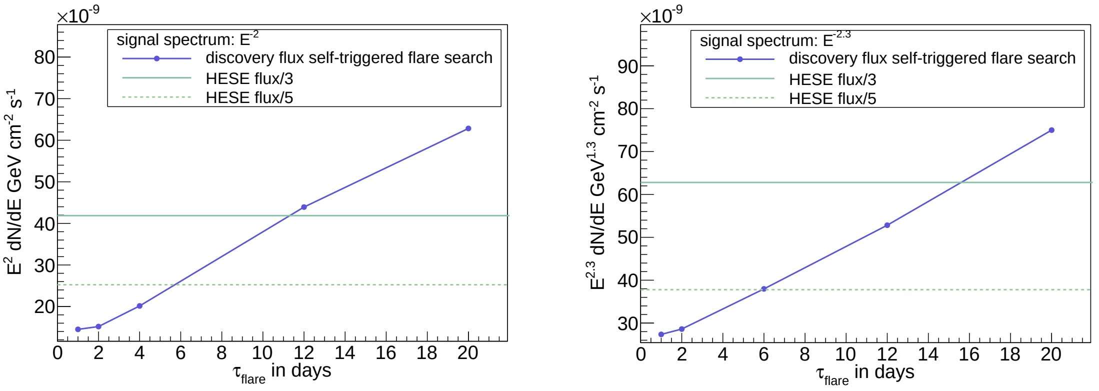

(a) Discovery potential E^{-2} spectrum

(b) Discovery potential $E^{-2.3}$ spectrum

Figure 8.6.: (a) Discovery potential of the self-triggered flare search for a E^{-2} spectrum as a function of τ_{flare} integrated over all sources. (b) Discovery potential of the self-triggered flare search for a $E^{-2.3}$ spectrum as a function of τ_{flare} integrated over all sources.

then compared to the background test statistic, in order to evaluate a significance. A correction for trials is included in using 100 000 scrambled background trials, which are extrapolated with an exponential Fit, correspondingly to the eMPS search, see Sec. 7. The discovery potential (50%, 5σ) for the scenario taking only the northern hemisphere until a declination of -20° into account is shown in Fig. 8.6(a) for a E^{-2} spectrum and in 8.6(b) for a $E^{-2.3}$ spectrum as a function of τ_{flare}. As expected, the flux needed for a discovery increases with the duration of the simulated flare.

For a better comparison with other point source analyses, a second signal simulation model is studied. In this second scenario, the flux per source is varied instead of a variation of the number of contributing sources. In this way, all sources contribute to the total flux and the flux per source is lowered. Figure 8.7 shows the resulting discovery flux per source for the self-triggered flare search for a E^{-2} spectrum as a function of τ_{flare} in comparison to the standard point source search and the untriggered flare search at a declination of $\delta = 16°$ [158]. Since the stacking approach adds more background for long flare durations, the discovery flux for the self-triggered flare search increases for longer simulated flares and becomes worse than the untriggered flare search. However, the discovery flux for the self-triggered flare search is approximately at the same level as the untriggered flare search and becomes even better for short flares. For almost all considered flare durations the discovery flux of the self-triggered flare search is much better than the standard point source search.

8.4 Results

The self-triggered flare search was applied to the presented data sample of IC79/IC86 data. The results for the different flare bins are shown in Fig. 8.8 with the ratio of

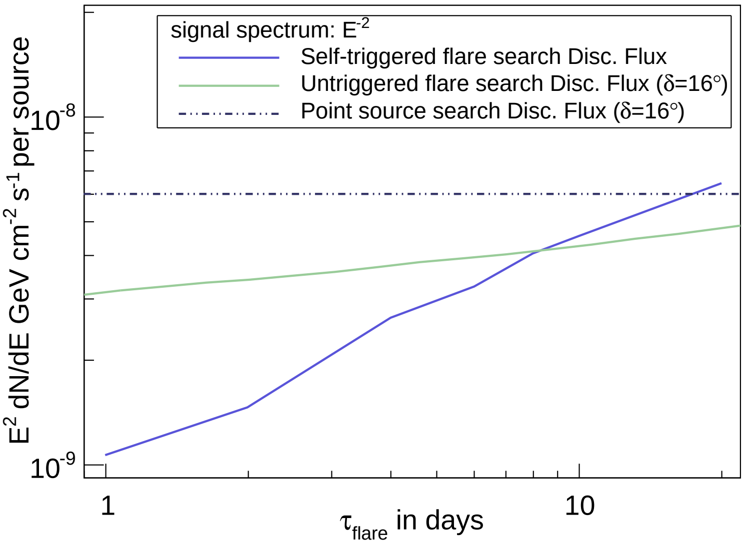

Figure 8.7.: Discovery potential of the self-triggered flare search for a E^{-2} spectrum as a function of τ_{flare} as flux per source (blue) in comparison to the discovery flux of the untriggered flare search (green) and the standard point source search (dashed line) on IC86 data at a declination of $\delta = 16°$.

the observed number of pairs over the average number of pairs in the background as a function of the clustering scale θ shown in the upper panel. The 1σ and 2σ contours are shown in green colour. The lower panel shows the pre-tial p-value in dependence of the clustering scale θ. The best pre-trial p-value was found in the one day flare bin and results in 0.15. After taking the trials for the different angular and time bins into account, this value reduces to 0.6. The p-value corresponds to one pair in correlation to HESE event 1 within a time interval of two days. Their reconstructed declinations are -9° and 8.5° and the right ascensions are 20.6° and 20.4°, respectively. The energies of both events are 4.6 TeV and 1.8 TeV, see Tab. 8.2. Their angular distance is less than half a degree. Figure 8.9(a) shows the location of the resulting event pair in correspondence to the HESE event 1 and the other events in that specific segment of the sky. Additionally, the events in correspondence to the HESE event 1 inside a time window of ±1 day are shown in black, but indicate no significant clustering. In Fig. 8.9(b) the time window around the HESE event 1 with the resulting pair is shown. Figure 8.10 shows the event views of both events inside the IceCube detector. As they are reconstructed down-going with relatively low energy it is probable that they correspond to atmospheric muons induced by a cosmic ray shower in the atmosphere. Event 1 could still be a neutrinos which is entering the dust layer, where less signal is visible in the DOMs. Event 2 seems to correspond to an atmospheric muon.

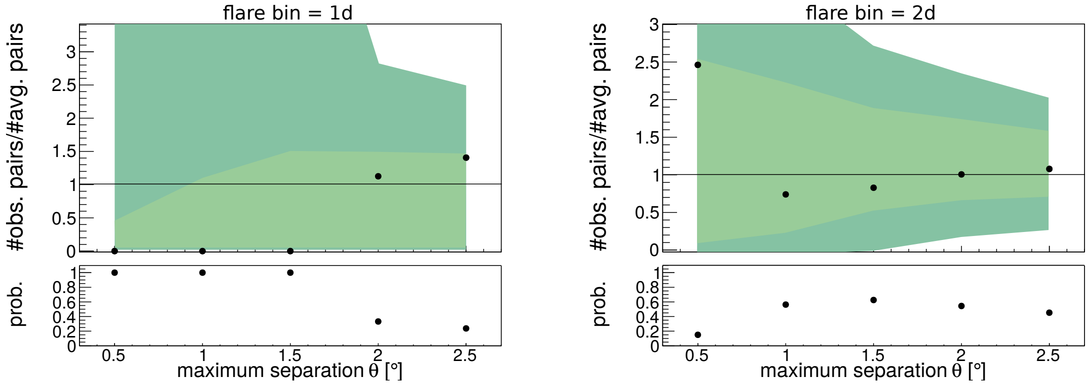

(a) flare bin=1d

(b) flare bin=2d

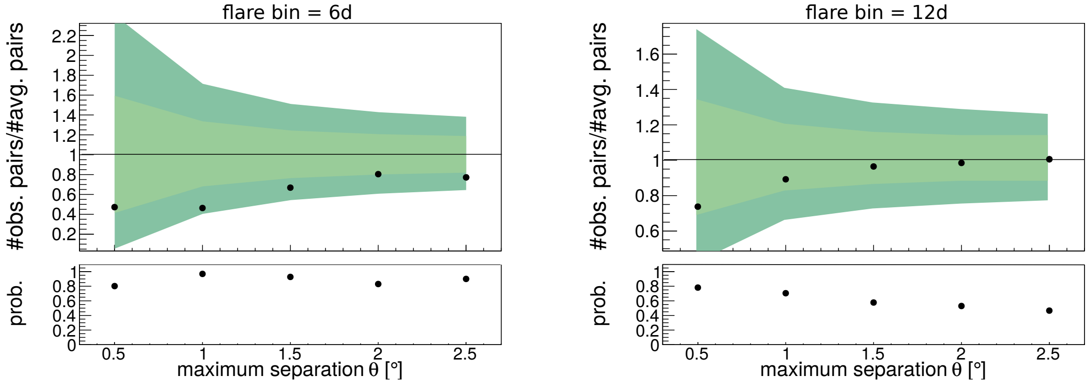

(c) flare bin=6d

(d) flare bin=12d

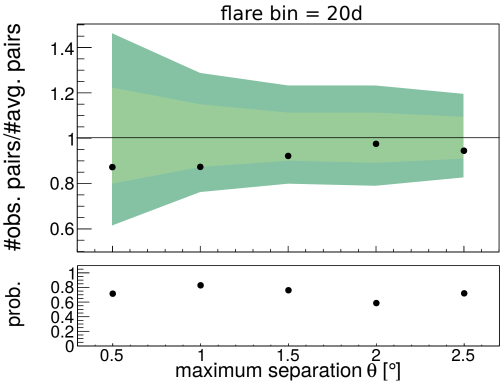

(e) flare bin=20d

Figure 8.8.: Results of the self triggered flare search in the (a) one, (b) two (c) six, (d) twelve and (e) 20 days flare bin as a function of θ. In the upper panel the number of observed pairs over the number of average background pairs is shown, with the 1σ and 2σ contours in green. The lower panel shows the pre-trial p-value.

	Event 1	Event 2	HESE Event 1
RA [°]	20.4	20.6	35.2
Dec [°]	−8.7	−9	−1.8
Energy [TeV]	1.8	4.7	47.6
Time [MJD]	55 350.909 48	55 351.982 46	55 351.322 21

Table 8.2.: Results of the self-triggered flare search in IC79/IC86 data. The best p-value was found at 0.5° in the two day time interval showing one pair. The properties of the two events in correspondence to the HESE event 1 are shown.

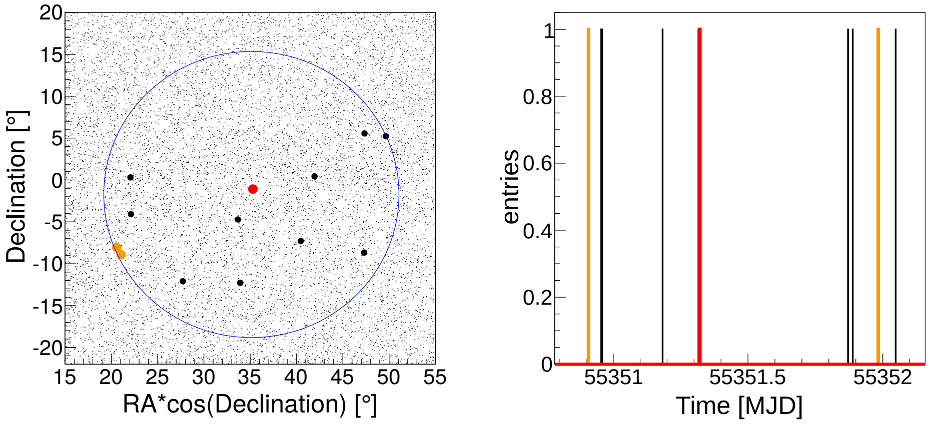

(a) Event 1

(b) Event 1

Figure 8.9.: (a) Segment of the sky showing the locations of the events of the self triggered flare search corresponding to the HESE event 1 (red). The resulting event pair of the self triggered flare search (orange) matches also in time. The black dots show additional twelve events matching in time, but showing no spatial clustering. (b) Times of the events in correspondence to the HESE event 1 (red) and the pair of events with an additional spatial clustering (orange).

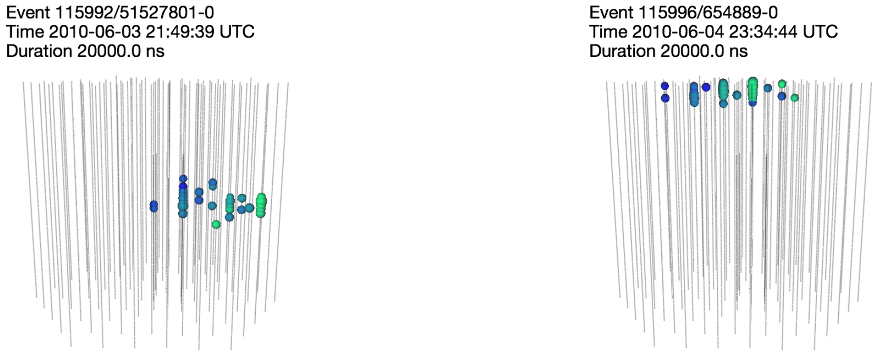

(a) Event 1

(b) Event 2

Figure 8.10.: Event views of the pair of events corresponding to the best p-value of 0.6 found in the self-triggered flare search in the time interval of two days and an angular scale of 0.5°.

8.5 Discussion

A self-triggered flare search was applied for the first time to IceCube data, using a two-year datasample with the 28 events found in [15] as a trigger. The results of this search are consistent with background expectations with a small underfluctuation. The best p-value is 0.6 after trial correction and was found in a time interval of two days at less than 0.5° angular distance. The corresponding pair of events is found in coincidence with HESE event 1, but seems to be dominated by background and no connection to astrophysical sources can be made. However, the search proved to be robust and well-working and covers an important addition to the conventional point source searches.

9

Systematic Uncertainties

All analyses presented in this work are affected by only few systematic uncertainties due to uncertainties in the background estimation and in the signal efficiency. Since the background estimation is based on randomized experimental data, the p-values are unaffected by uncertainties in the calculation of atmospheric neutrino or muon fluxes, that use assumptions about the hadronic models of shower development in the atmosphere or on the composition of cosmic rays. Unlike for diffuse searches, they are also independent of the poorly known prompt neutrino flux. However, the point spread function used in the signal simulation depends on MC-data and is therefore affected by systematic uncertainties. Moreover, systematic effects in the background can result from pre-existing large-scale anisotropies in the experimental sample.

In order to estimate the systematic influences on the different data samples used in this work, only IC79 and IC86 data samples will be considered, since they contain most of the events in the combined samples, while assuming that all samples suffer the same systematic effects. Since the low-energy range is affected more by systematic uncertainties and the IC79/IC86 data sample contains most of the low-energy events, this assumption can be seen as conservative. The argumentation and the estimation of the systematic uncertainties follows here closely [18]. However, the numbers quoted in [18] differ from the numbers in this work, since they are calculated on a different IC79 sample and do a full propagation to the sensitivity level. In this work, effective systematics are used in considering the effect on the flux normalization.

The two main uncertainties in the signal efficiency arise from the DOM-efficiency and optical properties of the ice. In the following the systematics for the two data samples will be discussed in detail.

9.1 IC79 Systematics

Systematic uncertainties in the signal efficiency arise mainly from the DOM-efficiency and optical properties of the ice. In this context the DOM-efficiency describes the absolute light detection efficiency of the optical modules. The variation of the ice parameters refers to the optical properties of the ice, including absorption and scattering, see Sec. 4.3.

To estimate the systematic errors for IC79, the following three uncertainties are considered in the calculation of the flux normalization used for the estimation of the discovery potential:

1. Variation of the DOM-efficiency by ±10%
2. Variation of the ice parameters by ±10%
3. Influence of a large-scale anisotropy in the background estimation.

These uncertainties affect mainly the 2-pt analysis, but since IC79 is used also in the other two samples the estimation is also important for the other two analyses. For the evaluation five different systematic data samples were available, two in which the absorption and scattering was varied by ±10% and three for the DOM Efficiency, setting the efficiency to 90 %, 110 % and 120 %. Additionally, these three sets used a different photon propagation model, which is called photon propagation code (ppc) [132], see Sec. 5.1.4. It computes the propagation of photons inside the detector directly, i.e. without the use of binning and tables as it is done in the standard simulation sample due to limited computing power. At trigger level ppc and photonics have the same amount of hits. However, the time residual distribution for photonics are slightly more distorted leading to more direct hits. In general, events with more direct hits pass the event selection cuts more easily resulting in an over-prediction of the event rate at final level for photonics, which gives a similar effect as a higher DOM efficiency.

As described in [18], the difference between the two methods is most relevant for energies below ∼1 TeV and decreases with energy. The resulting difference in terms of sensitivity is 7.2% for the northern hemisphere and can be accounted for by the uncertainty in the optical efficiency and is therefore not considered as an additional systematic uncertainty. Additionally, a dedicated study [122] based on ppc data showed that the DOM-efficiency is 10 % higher than the previous default value. For this reason, the standard value for systematic comparisons for ppc is 110 % and is used here as a baseline. Since no systematic data sample with 100 % DOM-efficiency is available, the uncertainty is interpolated using a linear model. In future applications, it is expected to use direct photon propagation and increase the nominal optical efficiency by 10% in order to account for the higher photon rate, as described above.

In Fig. 9.1(a) the zenith distribution of the standard simulation set and the five systematic datasets are shown for the northern hemisphere for a E^{-2} spectrum. For the set with an absorption and scattering lowered by 10% and the DOM-efficiency 90 % the rates are much lower than for the standard set.

	northern hemisphere		
spectrum	E^{-2}	E^{-3}	$\mathrm{E}^{-2.25}$
Abs and Scatt +10%	+3 %	+5.1%	+3.4%
Abs and Scatt -10%	−5.6%	−11.2%	−6.5%
DOM Efficiency 110/120	−3.8%	−7.8%	−4.5%
DOM Efficiency 110/100*	+7.2%	+14.7%	+8.1%
IT Veto Random coinc.		<1%	
Rel. DOM Effiency		<1%	
Muon energy losses, ν-N cross-section and rock density		±4%	
total effect	**+8.8%/-7.8%**	**+16.1%/-14.2%**	**+9.6%/-8.9%**

*estimated using a linear model.

Table 9.1.: Systematic errors on the flux normalization for the IC79 sample for the northern hemisphere while varying the DOM-efficiency and absorption and scattering of the ice.

Figure 9.1(b) shows the distribution of the angular difference of the reconstructed and true angular direction (Ψ) for the same datasets, again for a E^{-2} spectrum. In Fig. 9.1(c) the energy distribution of the different samples is shown for a E^{-2} spectrum. In Fig. 9.1(d) the median of the PSF distribution is shown for different energies for the different systematic samples and is compared to the standard sample. All graphs show a good agreement of the systematic data samples with the standard data sample.
The resulting effects on the sensitivities in varying the DOM-efficiency and the ice parameters are shown in Tab. 9.1 for the different spectra used in the limit calculations of the 2-pt analysis in the northern hemisphere. For a variation of ±10% of the absorption and scattering the uncertainty is +3%/-5.6% for a E^{-2} spectrum. The effect in the DOM Efficiency scales to -3.8%/+7.2% in the same spectrum. In addition to the presented systematic uncertainties, other contributions like random coincidences in the IceTop veto and the relative DOM-efficiency were studied. They show all a negligible impact and are not considered here. In [135] it was shown, that the uncertainty arising from muon energy losses, neutrino cross sections and the rock density is considered to be ±4%. For a E^{-2} spectrum the overall systematic uncertainty results in +8.8%/-7.8% for the IC79 data sample. The corresponding values for the southern hemisphere are shown in Tab. 9.2 and result in an overall systematic uncertainty of +6.1%/-9.2% for a E^{-2} spectrum.

Effect of a Large-Scale Anisotropy in the Two-Point Analysis

Point source searches looking for small-scale anisotropies must be distinguishable from possible large-scale structures in the data sample, which could have an effect on the test

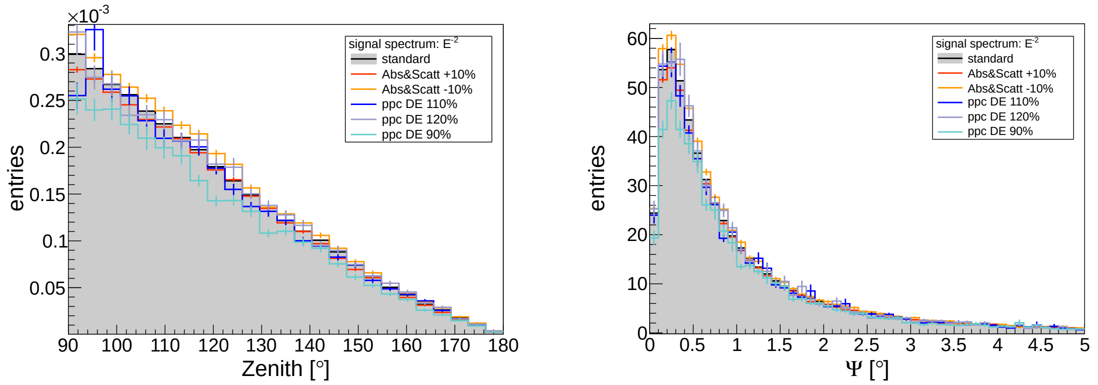

(a) Zenith distribution

(b) PSF distribution

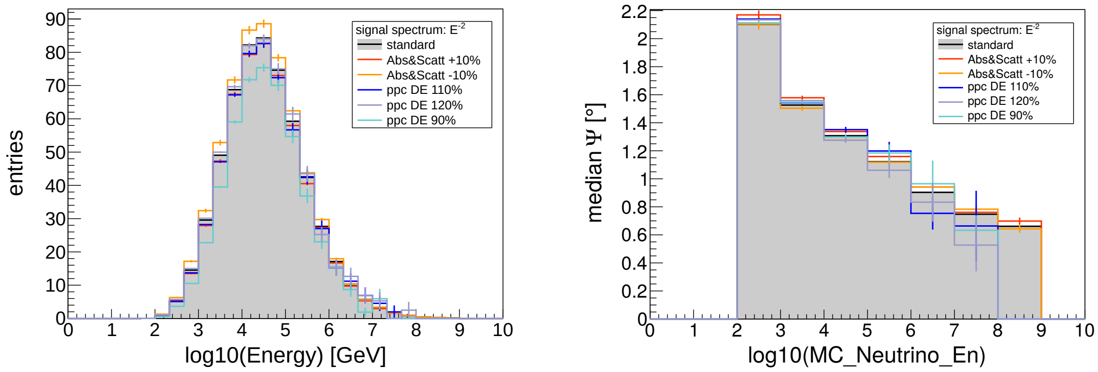

(c) Energy distribution

(d) PSF vs energy distribution

Figure 9.1.: (a) Zenith distribution of the standard simulation set (grey) and the five systematic datasets for the northern hemisphere for a E^{-2} spectrum. (b) PSF of the standard simulation set (grey) and the five systematic datasets for the northern hemisphere for a E^{-2} spectrum. (c) Energy distribution for the standard simulation set (grey) and the five systematic datasets using a E^{-2} spectrum. (d) median of the PSF distribution for different energies for the standard simulation set (grey) and the five systematic datasets using a E^{-2} spectrum.

spectrum	southern hemisphere E^{-2}
Absorption and Scattering +10%	+4.2%
Absorption and Scattering -10%	−7.4%
DOM Efficiency 110/120	−3.7%
DOM Efficiency 110/100*	+1.7%
IT Veto Random coinc.	<1%
Rel. DOM Effiency	<1%
Muon energy losses, ν-N cross-section and rock density	±4%
total effect	**+6.1%/-9.2%**

*estimated using a linear model.

Table 9.2.: Systematic errors on the flux normalization for the IC79 sample for the southern hemisphere while varying the DOM-efficiency and absorption and scattering of the ice.

statistic and thus influence the sensitivity. To investigate the effect of a pre-existing large-scale anisotropy in the background, the 2-pt analysis is repeated including a large-scale anisotropy in the background of atmospheric neutrinos and muons for the mixed sky maps, while keeping the test statistic of the null hypothesis fixed. This procedure was applied first to a multipole analysis in [159] and is done accordingly. The large-scale anisotropy is simulated according to a measurement at TeV energies by Milagro [160]. The normalized cosmic ray anisotropy is in the order of $\sim 10^{-3}$ and is shown in Fig. 9.2. Since the Milagro anisotropy is an anisotropy in cosmic rays, a possible anisotropy of atmospheric muons and neutrinos is expected of about the same order of magnitude. The corresponding systematic errors are given by the resulting shift in the sensitivity of the 2-pt analysis in the northern hemisphere and is shown in Tab. 9.3 for the three different spectra used in the analysis. While it was simulated for different numbers of sources, the table shows only the maximum deviation for each spectrum. For all spectra, the sensitivity is increasing slighty compared to the standard isotropic background, as clustering might be enhanced in using this additional structure in the background.

spectrum	E^{-2}	E^{-3}	$E^{-2.25}$
Large Scale Anisotropy	−4%	−6%	−8%

Table 9.3.: The uncertainty of the sensitivity in the northern hemisphere due to a large-scale anisotropy in the background estimation of the 2-pt analysis for the different spectra.

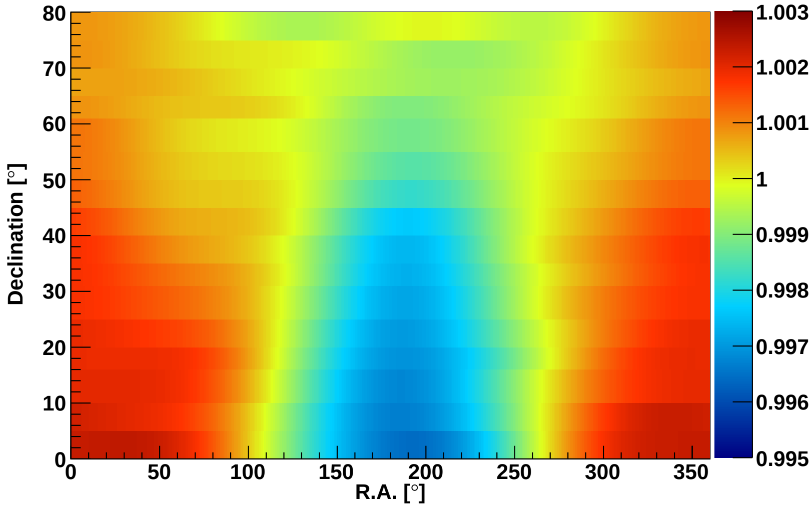

Figure 9.2.: Cosmic ray anisotropy in the northern hemisphere as obtained by Milagro [160] at TeV energies. The bin entries are normalized to the all-sky average.

IC79 Spline Sample

For the eMPS analysis and the self-triggered flare search, the IC79Spline sample is used. The spline reconstruction is assumed to be more sensitive on the optical properties of the ice. However, for the IC79 spline sample alone, no systematic samples are available and no systematic studies were performed. The impact from the spline reconstruction can be evaluated by the study done on the IC86 sample, which uses also the spline reconstruction method and is described in the next section.

9.2 IC86 Systematics

For the IC86 data sample the event selection and the reconstruction methods are similar to the ones used in IC79, yielding about the same systematic effects [139]. However, a different muon reconstruction method, using spline tables [101] was implemented. This reconstruction could be more sensitive to uncertainties in the optical properties of the ice. To evaluate the effects of the ice properties two systematic datasets were used, varying the absorption +10% and scattering +10%. All sets use the same ice model as the standard set (SpiceMie) and the same photon propagator (ppc). Since no systematic dataset with absorption or scattering -10% was available, the uncertainties are again approximated using a linear model, giving symmetric results.
The zenith distribution for the standard and the three systematic datasets is shown in Fig. 9.3(a) for a E^{-2} spectrum. The angular reconstruction error (Ψ) is illustrated in Fig. 9.3(b). The energy for the different samples is shown in Fig. 9.3(c). The median of the angular reconstruction error is plotted against the energy in Fig. 9.3(d). The changes in all distributions is small, the rate of events varies however by a factor

	northern hemisphere		
spectrum	E^{-2}	E^{-3}	$E^{-2.25}$
Absorption +10%	+8.2%	+15.6%	+10.8%
Scattering +10%	+7.4%	+14.6%	+10.2%
Absorption -10%*	−8.2%	−15.6%	−10.8%
Scattering -10%*	−7.4%	−14.6%	−10.2%
total effect	**+11%/-11%**	**+21.3%/-21.3%**	**+14.8%/-14.8%**

*estimated using a linear model.

Table 9.4.: Systematic errors on the flux normalization for the IC86 sample for the northern hemisphere while varying the absorption and scattering of the ice.

Analysis	2-pt	MPS	STFS
overall uncertainty	+9%/-8.9%	+14.1%/-13.4%	+14.1%/-13.4%

Table 9.5.: The overall uncertainties for the different analyses in the northern hemisphere and a E^{-2} spectrum.

+8.7%/-0.5% for a E^{-2} spectrum in the IC86 datasample. The DOM-efficiency is assumed to be the same as in the IC79 dataset and no systematic datasamples were provided. The resulting effects on the sensitivity are shown in Tab. 9.4 for three different spectra. For a E^{-2} spectrum the resulting uncertainty introduced by variation of the absorption and scattering and taking the IC79 DOM-efficiency into account is +13.1%/-11.6%.

9.3 Summary of the Systematic Uncertainties

For each of the three data samples used in the analyses, a different overall systematic effect has to be considered. For the 2-pt analysis the quadratic sum results in an uncertainty of +9%/-8.9% for a E^{-2} spectrum, including the large scale anisotropy. For the MPS and the self-triggered flare search the uncertainties are roughly the same, since the impact of IC40 and IC59 data is negligible and gives an uncertainty of +14.1%/-13.4% for a E^{-2} spectrum. Table 9.5 summarizes the uncertainties for all analyses. The resulting overall systematic uncertainties are in agreement with [18] and [139].

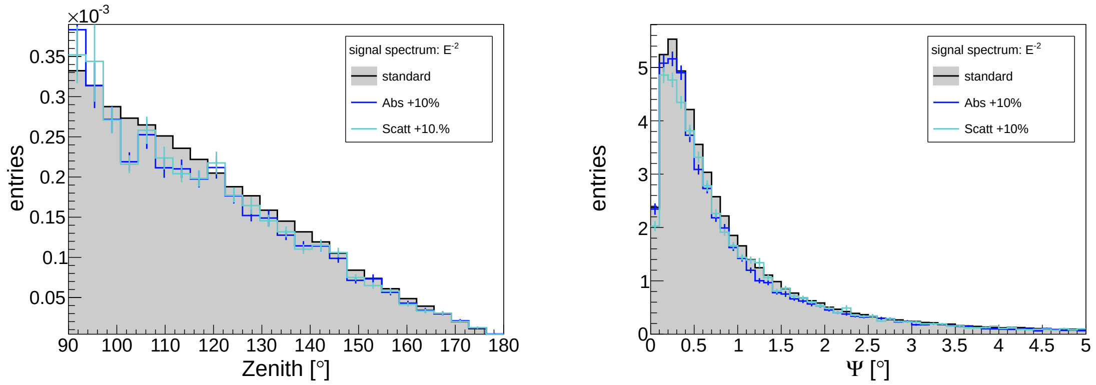

(a) Zenith distribution

(b) PSF distribution

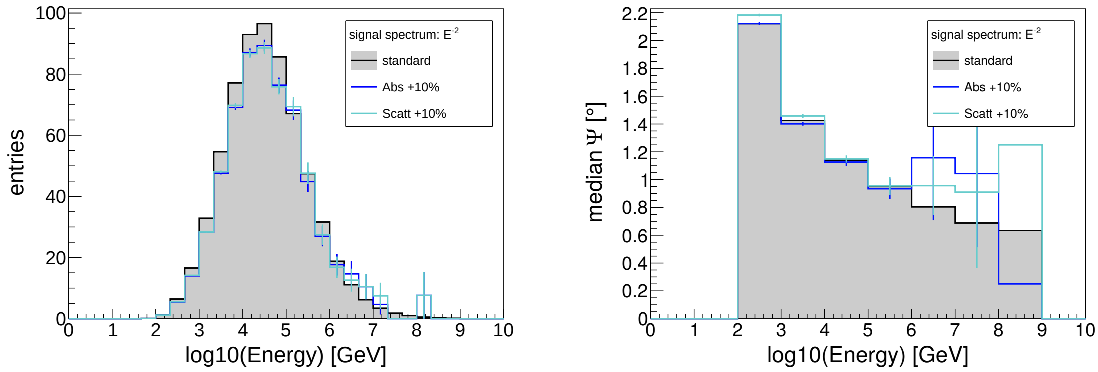

(c) Energy distribution

(d) PSF vs energy distribution

Figure 9.3.: (a) Zenith distribution of the standard simulation set (grey) and the five systematic datasets for the northern hemisphere for a E^{-2} spectrum. (b) PSF of the standard simulation set (grey) and the systematic datasets for the northern hemisphere for a E^{-2} spectrum. (c) Energy distribution for the standard simulation set (grey) and the systematic datasets using a E^{-2} spectrum. (d) median of the PSF distribution for different energies for the standard simulation set (grey) and the systematic datasets using a E^{-2} spectrum.

10

Conclusion

The detection of the first 28 astrophysical neutrinos by IceCube in 2013 has been a big success and proved the detector as a well-working and unique instrument for measuring high-energy neutrinos. However, this detection raised new questions: Where do these events come from? Are they truly diffuse or can they be resolved into point sources? Different kind of likelihood searches were applied on IceCube data to solve these questions and to search for neutrino point sources. However, none of these analyses were able to detect a neutrino point source. In this work three analyses for a small-scale clustering of neutrino events are presented. They are all based on a two-point correlation function and target a different scenario in searching not only for one strong point source, but several weaker sources, which can not be detected by the standard likelihood point source search.

The first search is a two-point correlation function applied on the full sky and the results are consistent with background fluctuations. Limits were calculated for both hemispheres and different spectra. For the astrophysical flux previously observed in IceCube no additional regions can be excluded, as it was by former IceCube analyses. For softer energy spectra the analysis presented here disfavours the observed flux to come from less than ~ 20 sources for $E^{-2.25}$ and from less than ~ 5000 sources for E^{-3} spectra. For the southern hemisphere the analysis is not competitive to the flux level observed by the HESE analysis, due to the high background of atmospheric muons from cosmic ray air showers.

The second search uses the multi point source method and targets the Cygnus region. No significant fluctuation above background was visible and limits were calculated for two different spectra. Both limits are compared to measurements of the gamma ray flux from Milagro assuming proton-proton interactions. The IceCube limits are able to reach the gamma ray fluxes, but are not yet able to constrain. However, the fluxes measured by Milagro suffer large uncertainties and new measurements by Veritas and

Hawc suggest even lower diffuse fluxes from that region.
The third analysis presented here is a self-triggered flare search which used for the first time IceCube events as a self-trigger. It is based on the multi point source method, which was extended for a time dependency and a stacking approach and searched for coincident events to the astrophysical events obtained in the HESE analysis. No significant clustering was found.
All three analyses are important additions to the standard analyses performed in IceCube, as they target different search hypotheses and are completely model-independent. Moreover, the suffer small systematic uncertainties and can be adapted easily to different signal scenarios. For future applications and increased statistics in IceCube it might be applicable to migrate to GPU computing units and even improve the performance further. In addition, the analyses will eventually provide first hints of a neutrino point source.
In conclusion, the high-energy starting events are the beginning of a new era in astronomy, as it was for gamma ray astronomy starting with 22 events in 1965 [161]. The methods developed here are at the frontier of a possible identification of the responsible sources. IceCube, as a unique scientific instrument is already significantly improving our understanding of the processes and mechanism of the Universe and might further contribute in the future.

A

Additional Figures

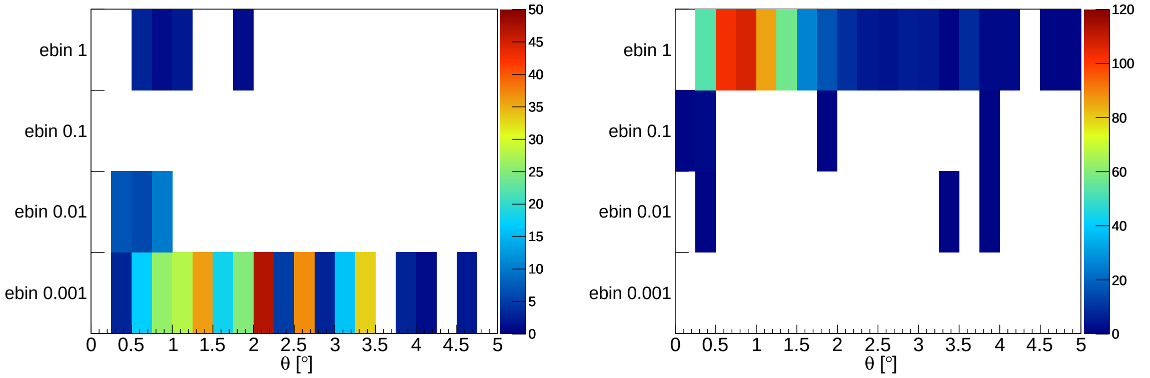

(a) Best clustering bin E^{-2} spectrum (b) Best clustering bin $E^{-2} \cdot e^{E/10TeV}$ spectrums

Figure A.1.: Best clustering bin for a (a) E^{-2} spectrum and (b) $E^{-2} \cdot e^{E/10TeV}$ spectrum as a function of θ and the energy bins for the southern hemisphere. The colour bar displays the entries of global p-values in each bin.

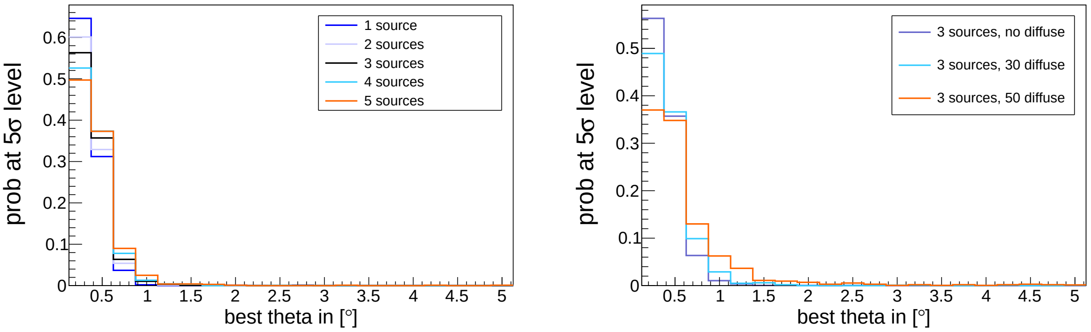

(a) Best clustering bin E^{-2} spectrum for different numbers of sources

(b) Best clustering bin E^{-2} spectrum for additional events

Figure A.2.: (a) Preferred clustering bin for different numbers of point sources for a E^{-2} spectrum. (b) Preferred clustering bin for three point sources with additional diffuse events for a E^{-2} spectrum.

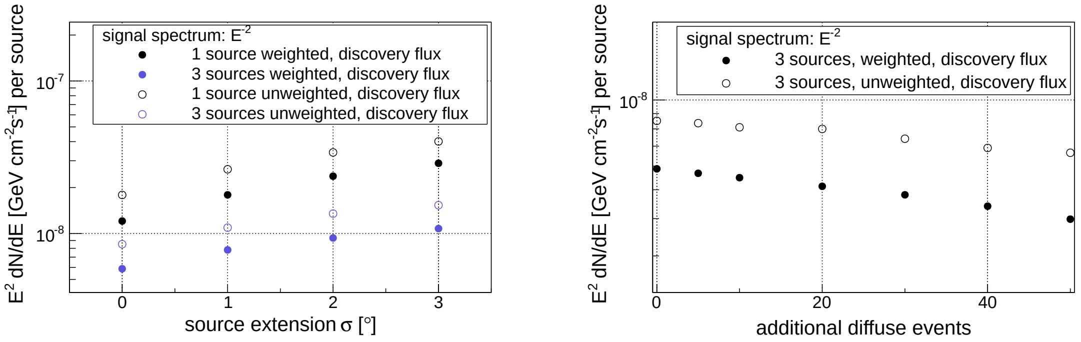

(a) Discovery flux for different source extensions σ

(b) Discovery flux for additional diffuse events

Figure A.3.: (a) Discovery potential as a function of the source extension σ in the search region for one (black) and three (blue) sources using a E^{-2} neutrino energy spectrum with and without additional energy weighting. (b) Discovery potential as a function of additional diffuse events in the search region for three point sources using a E^{-2} neutrino energy spectrum with and without additional energy weighting.

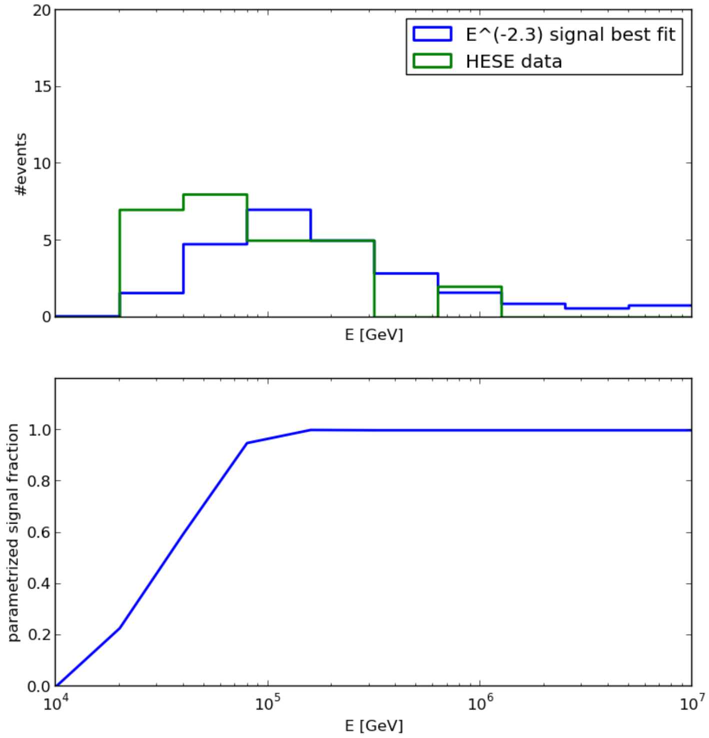

Figure A.4.: Events obtained in the HESE analysis with the expected events from the best fit considering a $E^{-2.3}$ spectrum (upper panel). The lower panel shows the ratio of both event rates as a probability depending on the energy.

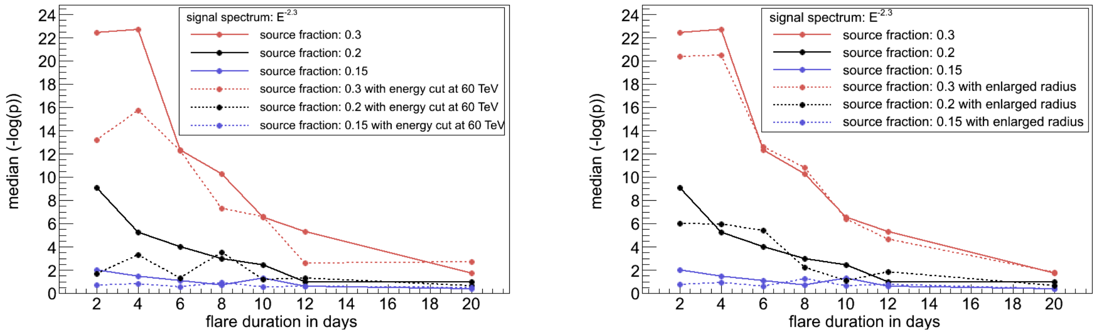

(a) Significances with energy cut at 60 TeV

(b) Significances with enlarged search radius

Figure A.5.: (a) Significances with energy cut at 60 TeV (dashed) compared to the scenario without energy cut (continuous) for a $E^{-2.3}$ spectrum, as a function of τ_{flare}. Shown are different values for f_{sig}. (b) Significances with enlarged search radius of +0.5° around tracks (dashed) compared to the scenario without enlarged regions (continuous) for a $E^{-2.3}$ spectrum, as a function of τ_{flare}. Shown are different values for f_{sig}.

References

[1] S. Chatrchyan et al. **Observation of a new boson at a mass of 125 GeV with the CMS experiment at the LHC**. *Physics Letters B* 716 (2012), arXiv: `1207.7235 [hep-ex]` (see p. 1).

[2] G. Aad et al. **Observation of a new particle in the search for the Standard Model Higgs boson with the ATLAS detector at the LHC**. *Physics Letters B* 716 (2012), arXiv: `1207.7214 [hep-ex]` (see p. 1).

[3] V. F. Hess. **Über Beobachtungen der durchdringenden Strahlung bei sieben Freiballonfahrten**. *Z. Phys.* 13 (1912), (see p. 1).

[4] P. Mészáros. **Gamma-ray bursts**. *Reports on Progress in Physics* 69.8 (2006), (see pp. 1, 26).

[5] E. Waxman. **Neutrino astronomy and gamma-ray bursts**. *Phil.Trans.R.Soc. A* 365.1854 (2007), eprint: `http://rsta.royalsocietypublishing.org/content/365/1854/1323.full.pdf+html` (see p. 1).

[6] F. W. Stecker et al. **High-energy neutrinos from active galactic nuclei**. *Phys. Rev. Lett.* 66 (21 1991), (see p. 1).

[7] E. Waxman and J. Bahcall. **High energy neutrinos from astrophysical sources: An upper bound**. *Phys.Rev. D* 59 (2 1998), (see p. 1).

[8] M. Doert et al. **Correlated neutrino and gamma-ray emission from Active Galactic Nuclei - an estimation**. *Journal of Physics: Conference Series* 355.1 (2012), (see p. 2).

[9] W. Atwood et al. **The Large Area Telescope on the Fermi Gamma-Ray Space Telescope Mission**. *ApJ* 697.2 (2009), (see p. 2).

[10] J. K. Becker. **High-energy neutrinos in the context of multimessenger astrophysics**. *Physics Reports* 458 (2008), arXiv: `0710.1557` (see p. 2).

[11] E. Waxman and J. Bahcall. **High Energy Neutrinos from Cosmological Gamma-Ray Burst Fireballs**. *Phys. Rev. Lett.* 78 (12 1997), (see p. 2).

[12] IceCube Collaboration. **The IceCube data acquisition system: Signal capture, digitization, and timestamping**. *Nuclear Instruments and Methods* A601.3 (2009), (see pp. 2, 37, 38).

[13] IceCube Collaboration. **Calibration and Characterization of the IceCube Photomultiplier Tube**. *Nuclear Instruments and Methods* (2010), arXiv: `1002.2442 [astro-ph.IM]` (see pp. 2, 37, 39).

[14] A. Achterberg et al. **First Year Performance of The IceCube Neutrino Telescope**. *Astroparticle Physics* 26 (2006), arXiv: `astro-ph/0604450 [astro-ph]` (see p. 2).

[15] Icecube Collaboration. **Evidence for High-Energy Extraterrestrial Neutrinos at the IceCube Detector**. *Science 342,* 1242856 (2013). arXiv: `1311.5238 [astro-ph.HE]` (see pp. 2, 3, 44, 91, 93, 102).

[16] Icecube Collaboration. **Observation of High-Energy Astrophysical Neutrinos in Three Years of IceCube Data**. *Phys. Rev. Lett.* 113.10, 101101 (2014), arXiv: `1405.5303 [astro-ph.HE]` (see pp. 2, 71, 74, 76, 78).

[17] P. Padovani and E. Resconi. **Are both BL Lacs and pulsar wind nebulae the astrophysical counterparts of IceCube neutrino events?** *Monthly Notices of the RAS* 443 (2014), arXiv: `1406.0376 [astro-ph.HE]` (see p. 2).

[18] Icecube Collaboration. **Search for Time-independent Neutrino Emission from Astrophysical Sources with 3 yr of IceCube Data**. *ApJ* 779, 132 (2013), (see pp. 3, 51–53, 62, 68, 69, 71, 73, 74, 76–78, 103, 104, 109).

[19] Icecube Collaboration. **The IceCube Neutrino Observatory Part I: Point Source Searches**. *arXiv eprint:1309.6979* (2013). arXiv: `1309.6979 [astro-ph.HE]` (see pp. 3, 62).

[20] Icecube Collaboration. **Search for a diffuse flux of astrophysical muon neutrinos with the IceCube 59-string configuration**. *Phys. Rev. D* 89.6, 062007 (2014), (see pp. 3, 63).

[21] IceCube Collaboration. **Searches for small-scale anisotropies from neutrino point sources with three years of IceCube data**. *ArXiv e-prints* (2014). arXiv: `1408.0634 [astro-ph.HE]` (see pp. 3, 71, 73).

[22] W. Bothe and W. Kolhörster. **Das Wesen der Höhenstrahlung**. *Zeitschrift für Physik* 56 (1929), (see p. 5).

[23] C. D. Anderson. **The Positive Electron**. *Physical Review* 43 (1933), (see p. 5).

[24] S. H. Neddermeyer and C. D. Anderson. **Note on the nature of cosmic-ray particles**. *Physical Review* 51.10 (1937), (see p. 5).

[25] R. Mewaldt. **Cosmic Rays**. *Macmillan Encyclopedia of Physics.* (1996) (see p. 5).

[26] T. Gaisser. **Cosmic Rays and Particle Physics**. Cambridge University Press, 1990 (see p. 6).

[27] J. Beringer et al. **Review of Particle Physics**. *Phys. Rev. D* 86 (1 2012), (see pp. 6, 27, 45, 48).

[28] ICECUBE COLLABORATION. **Measurement of the cosmic ray energy spectrum with IceTop-73**. *ArXiv e-prints* (2013). arXiv: `1307.3795 [astro-ph.HE]` (see p. 7).

[29] J. R. HÖRANDEL. **Models of the knee in the energy spectrum of cosmic rays**. *Astroparticle Physics* 21 (2004), eprint: `astro-ph/0402356` (see p. 7).

[30] J. BLÜMER, R. ENGEL, and J. R. HÖRANDEL. **Cosmic rays from the knee to the highest energies**. *Progress in Particle and Nuclear Physics* 63 (2009), arXiv: `0904.0725 [astro-ph.HE]` (see pp. 7, 8, 19).

[31] A. CASTELLINA and F. DONATO. **Astrophysics of Galactic charged cosmic rays**. *ArXiv e-prints* (2011). arXiv: `1110.2981 [astro-ph.GA]` (see p. 7).

[32] J. ABRAHAM et al. **Observation of the Suppression of the Flux of Cosmic Rays above $4{\cdot}10^{19}$eV**. *Phys. Rev. Lett.* 101.6, 061101 (2008), arXiv: `0806.4302` (see p. 7).

[33] R. ABBASI et al. **First Observation of the Greisen-Zatsepin-Kuzmin Suppression**. *Phys. Rev. Lett.* 100.10, 101101 (2008), eprint: `astro-ph/0703099` (see pp. 7, 8).

[34] A. A. WATSON. **Highlights from the Pierre Auger Obseervatory - the birth of the hybrid era**. *ArXiv e-prints* (2008). arXiv: `0801.2321` (see p. 8).

[35] O. ADRIANI et al. **PAMELA Measurements of Cosmic-Ray Proton and Helium Spectra**. *Science* 332 (2011), arXiv: `1103.4055 [astro-ph.HE]` (see p. 8).

[36] M. AGUILAR et al. **First Result from the Alpha Magnetic Spectrometer on the International Space Station: Precision Measurement of the Positron Fraction in Primary Cosmic Rays of $0.5 - 350\,$GeV**. *Phys. Rev. Lett.* 110 (14 2013), (see p. 8).

[37] S. HAINO et al. **Measurements of primary and atmospheric cosmic-ray spectra with the BESS-TeV spectrometer**. *Physics Letters B* 594 (2004), eprint: `astro-ph/0403704` (see p. 8).

[38] S. GEIER et al. **A search for the signature of microquasars in the cosmic ray iron spectrum measured by {TIGER}**. *Advances in Space Research* 37.10 (2006). Astrophysics, (see p. 8).

[39] K. SHINOZAKI and M. TESHIMA. **AGASA results**. *Nucl. Phys. Proc. Suppl.* 136 (2004), (see p. 9).

[40] H. O. KLAGES et al. **The KASCADE Experiment**. *Nuclear Physics B Proceedings Supplements* 52 (1997), (see p. 9).

[41] P. DESIATI. **Observation of TeV-PeV cosmic ray anisotropy with IceCube, IceTop and AMANDA**. *Nuclear Instruments and Methods* (2014), arXiv: `1308.0246 [astro-ph.HE]` (see p. 9).

[42] IceCube collaboration. **Observation of Anisotropy in the Arrival Directions of Galactic Cosmic Rays at Multiple Angular Scales with IceCube**. *ApJ* 740, 16 (2011), arXiv: `1105.2326 [astro-ph.HE]` (see pp. 9, 10).

[43] A. A. Abdo et al. **Discovery of Localized Regions of Excess 10-TeV Cosmic Rays**. *Phys. Rev. Lett.* 101 (22 2008), (see pp. 9, 10).

[44] V. S. Ptuskin et al. **Effect of random nature of cosmic ray sources - supernova remnants - on cosmic ray intensity fluctuations, anisotropy, and electron energy spectrum**. *35th COSPAR Scientific Assembly.* Ed. by J.-P. Paillé. Vol. 35. COSPAR Meeting. (2004), (see p. 9).

[45] A. W. Strong, I. V. Moskalenko, and V. S. Ptuskin. **Cosmic-Ray Propagation and Interactions in the Galaxy**. *Annual Review of Nuclear and Particle Science* 57 (2007), eprint: `astro-ph/0701517` (see p. 9).

[46] V. S. Berezinskii et al. **Astrophysics of cosmic rays**. (1990) (see p. 9).

[47] A. H. Compton and I. A. Getting. **An Apparent Effect of Galactic Rotation on the Intensity of Cosmic Rays**. *Phys. Rev.* 47 (11 1935), (see p. 9).

[48] E. Lorenz and R. Wagner. **Very-high energy gamma-ray astronomy. A 23-year success story in high-energy astroparticle physics**. *European Physical Journal H* 37 (2012), arXiv: `1207.6003` (see p. 10).

[49] A. W. Strong, I. V. Moskalenko, and O. Reimer. **Diffuse galactic continuum gamma rays: a model compatible with EGRET data and cosmic-ray measurements**. *ApJ* 613.2 (2004), (see p. 10).

[50] G. R. BLUMENTHAL and R. J. GOULD. **Bremsstrahlung, Synchrotron Radiation, and Compton Scattering of High-Energy Electrons Traversing Dilute Gases**. *Rev. Mod. Phys.* 42 (2 1970), (see pp. 12–14).

[51] M. S. Longair. **High Energy Astrophysics**. Cambridge University Press, 1992 (see p. 12).

[52] M. Longair. **Radiation Processes in High-Energy Astrophysics**. Talk at Astrophysical Spring School, Cargèse. (2006) (see pp. 13, 14).

[53] F. W. Stecker. **Observations of galactic gamma-rays and their implications for galactic structure studies**. *ApJ* 212 (1977), (see p. 13).

[54] T. Stanev. **Talk on High energy neutrinos : sources and fluxes**. TeVPA, Venice. (2007) (see p. 15).

[55] S. R. Kelner, F. A. Aharonian, and V. V. Bugayov. **Energy spectra of gamma rays, electrons, and neutrinos produced at proton-proton interactions in the very high energy regime**. *Phys. Rev. D* 74.3, 034018 (2006), eprint: `astro-ph/0606058` (see pp. 15, 89).

[56] F. M. Rieger, E. de Oña-Wilhelmi, and F. A. Aharonian. **TeV astronomy**. *Frontiers of Physics* 8 (2013), arXiv: `1302.5603 [astro-ph.HE]` (see pp. 16, 23).

[57] http://cds.cern. ch/record/1249755/files/p533.pdf. (see pp. 17, 18).

[58] C. Blaksley. **Photodetection Aspects of JEM-EUSO and Studies of the Ultra-High Energy Cosmic Ray Sky**. PhD thesis. Université Paris Diderot, (2014). arXiv: `1406.5818 [astro-ph.IM]` (see p. 17).

[59] A. M. Hillas. **The Origin of Ultra-High-Energy Cosmic Rays**. *Annual Review of Astron. and Astrophys.* 22 (1984), (see p. 17).

[60] E. Fermi. **On the Origin of the Cosmic Radiation**. *Phys. Rev.* 75 (8 1949), (see p. 18).

[61] A. R. Bell. **The acceleration of cosmic rays in shock fronts. I**. *Monthly Notices of the RAS* 182 (1978), (see p. 19).

[62] P. O. Lagage and C. J. Cesarsky. **The maximum energy of cosmic rays accelerated by supernova shocks**. *Astron. Astrophys.* 125 (1983), (see p. 19).

[63] L. Sparke and J. Gallagher. **Galaxies in the Universe: An Introduction**. Cambridge University Press, 2000 (see p. 19).

[64] NASA, JPL-Caltech and R. Hurt (SSC/Caltec). **Annotated Roadmap to the Milky Way**. (2008) (see p. 20).

[65] B. Reipurth and N. Schneider. **Star Formation and Young Clusters in Cygnus**. *Handbook of Star Forming Regions, Volume I.* Astronomical Society of the Pacific, (2008), (see p. 21).

[66] J. Knödlseder. **Cygnus OB2 - a young globular cluster in the Milky Way**. *Astron. Astrophys.* 360 (2000), eprint: `astro-ph/0007442` (see p. 21).

[67] A. Abdo et al. **Discovery of TeV Gamma-Ray Emission from the Cygnus Region of the Galaxy**. *ApJLett* 658 (2007), eprint: `astro-ph/0611691` (see pp. 21, 88–90).

[68] A. Abdo et al. **Spectrum and Morphology of the Two Brightest Milagro Sources in the Cygnus Region: MGRO J2019+37 and MGRO J2031+41**. *ApJ* 753, 159 (2012), arXiv: `1202.0846 [astro-ph.GA]` (see pp. 21, 88, 90).

[69] E. Aliu et al. **Spatially Resolving the Very High Energy Emission from MGRO J2019+37 with VERITAS**. *ApJ* 788, 78 (2014), arXiv: `1404.1841 [astro-ph.HE]` (see p. 21).

[70] G. Sinnis. **Air shower detectors in gamma-ray astronomy**. *New Journal of Physics* 11.5 (2009), (see p. 22).

[71] R. A. Ong. **Highlights from VERITAS on VHE gamma-ray sources in our Galaxy**. *Advances in Space Research* 53 (2014), arXiv: `1304.4903 [astro-ph.HE]` (see p. 22).

[72] J. M. Blondin, R. A. Chevalier, and D. M. Frierson. **Pulsar Wind Nebulae in Evolved Supernova Remnants**. *ApJ* 563 (2001), eprint: `astro-ph/0107076` (see p. 23).

[73] NASA, ESA, J. Hester and A. Loll. **A Giant Hubble Mosaic of the Crab Nebula**. 2005. URL: `http://hubblesite.org/newscenter/archive/releases/2005/37/image/a/` (see p. 24).

[74] D. Kazanas. **High energy neutrinos from active galactic nuclei**. URL: `http://www.inp.demokritos.gr/nestor/articles/files/kazanas.pdf` (see p. 24).

[75] C. M. Urry and P. Padovani. **Unified Schemes for Radio-Loud Active Galactic Nuclei**. *Publications of the ASP* 107 (1995), eprint: `astro-ph/9506063` (see pp. 24, 25).

[76] P. Armitage. **Classification of AGNs**. (2004). URL: `http://jila.colorado.edu/~pja/astr3830/lecture27.pdf` (see p. 25).

[77] M. Polletta. **BeppoSAX Calendar**. 1999. URL: `http://www.asdc.asi.it/bepposax/calendar/` (see p. 25).

[78] P. Mészáros. **The fireball shock model of gamma ray bursts**. *arXiv preprint astro-ph/9912474* (1999) (see p. 26).

[79] G. J. Fishman and C. A. Meegan. **Gamma-Ray Bursts**. *Annual Review of Astron. and Astrophys.* 33 (1995), (see p. 26).

[80] E. Berger. **Short-Duration Gamma-Ray Bursts**. *Annual Review of Astron. and Astrophys.* 52 (2014), arXiv: `1311.2603 [astro-ph.HE]` (see p. 26).

[81] Telescope Array Project. **Extensive Air Shower Detection**. 2011. URL: `http://www.telescopearray.org/index.php/about/detecting-uhe-cosmic-rays` (see p. 28).

[82] S. Cecchini and M. Spurio. **Atmospheric muons: experimental aspects**. *Geoscientific Instrumentation, Methods and Data Systems Discussions* 2 (2012), arXiv: `1208.1171 [astro-ph.EP]` (see p. 29).

[83] T. K. Gaisser. **Atmospheric Neutrino Fluxes**. *Physica Scripta Volume T* 121 (2005), eprint: `astro-ph/0502380` (see p. 29).

[84] T. K. Gaisser. **Atmospheric Neutrinos**. *Next Generation Nucleon Decay and Neutrino Deterctors NNN06*. Ed. by J. R. Wilkes. Vol. 944. American Institute of Physics Conference Series. (2007), eprint: `astro-ph/0612274` (see p. 29).

[85] T. K. Gaisser and M. Honda. **Flux of atmospheric neutrinos**. *Annual Review of Nuclear and Particle Science* 52 (2002), eprint: `hep-ph/0203272` (see p. 30).

[86] M. Honda et al. **Calculation of atmospheric neutrino flux using the interaction model calibrated with atmospheric muon data**. *Phys. Rev. D* 75.4, 043006 (2007), eprint: `astro-ph/0611418` (see pp. 30, 31).

[87] K. Abazajian et al. **Light Sterile Neutrinos: A White Paper**. *ArXiv e-prints* (2012). arXiv: `1204.5379 [hep-ph]` (see p. 30).

[88] IceCube Collaboration. **Measurement of the atmospheric neutrino energy spectrum from 100 GeV to 400 TeV with IceCube**. *Phys. Rev. D* 83.1, 012001 (2011), arXiv: `1010.3980 [astro-ph.HE]` (see p. 31).

[89] T. Gaisser and T. Stanev. **Path length distributions of atmospheric neutrinos**. *Phys. Rev. D* D57 (1998), arXiv: `astro-ph/9708146 [astro-ph]` (see p. 31).

[90] p. Desiati for the IceCube Collaboration. **Seasonal variation of atmospheric neutrinos in IceCube**. *Conference Proceedings of the 33rd International Cosmic Ray Conference.* (2013) (see p. 31).

[91] A. Schukraft. **Search for a diffuse flux of extragalactic neutrinos with the IceCube Neutrino Observatory**. PhD thesis. RWTH Aachen, (2013) (see p. 31).

[92] R. Enberg, M. H. Reno, and I. Sarcevic. **Prompt neutrino fluxes from atmospheric charm**. *Phys. Rev. D* D78 (2008), arXiv: `0806.0418 [hep-ph]` (see p. 31).

[93] K.-C. Lai, G.-L. Lin, and T. C. Liu. **Determination of the neutrino flavor ratio at the astrophysical source**. *Phys. Rev. D* 80.10, 103005 (2009), arXiv: `0905.4003 [hep-ph]` (see p. 31).

[94] M. A. Markov. **Annual International Conference on High Energy Physics at Rochester**. *Annual International Conference on High Energy Physics at Rochester.* Ed. by A. M. E.C.G. Sudarshan J.H. Tinlot. (1960), (see p. 33).

[95] A. Roberts. **The birth of high-energy neutrino astronomy: A personal history of the DUMAND project**. *Rev. Mod. Phys.* 64 (1 1992), (see p. 33).

[96] C. Spiering. **Towards high-energy neutrino astronomy. A historical review**. *European Physical Journal H* 37 (2012), arXiv: `1207.4952 [astro-ph.IM]` (see p. 33).

[97] S. W. Barwick and AMANDA Collaboration. **The Status of the AMANDA High-Energy Neutrino Detector**. *International Cosmic Ray Conference* 7 (1997), (see p. 33).

[98] L. F. Thompson. **Recent results from the ANTARES deep-sea neutrino telescope**. *Nuclear Physics B - Proceedings Supplements* 91.1 - 3 (2001). Neutrino 2000, (see p. 33).

[99] R. Gandhi et al. **Neutrino interactions at ultrahigh energies**. *Phys. Rev. D* 58.9, 093009 (1998), eprint: `hep-ph/9807264` (see p. 34).

[100] S. L. Glashow. **Resonant Scattering of Antineutrinos**. *Phys. Rev.* 118 (1 1960), (see p. 35).

[101] K. Schatto. **Stacked searches for high-energy neutrinos from blazars with IceCube**. PhD thesis. Johannes Gutenberg Universität Mainz, (2014) (see pp. 35, 48, 54, 108).

[102] A. Franckowiak. **Searching for High-energy Neutrinos from Supernovae with IceCube and an Optical Follow-up Program**. PhD thesis. Rheinische Friedrich-Wilhelms-Universität Bonn, (2011) (see p. 35).

[103] P. A. Cherenkov. **Visible emission of clean liquids by action of gamma radiation**. *Doklady Akademii Nauk SSSR* 2 (1934), (see p. 35).

[104] J. V. Jelley. **Cerenkov radiation and its applications**. *British Journal of Applied Physics* 6.7 (1955), (see p. 35).

[105] IceCube Collaboration. **The design and performance of IceCube DeepCore**. *Astroparticle Physics* 35.10 (2012), (see p. 37).

[106] J. A. S. Cohen and K. Mase. **New background rejection methods for the cosmogenic neutrino search with IceCube**. *Proceedings of the 32th International Cosmic Ray Conference.* (2011) (see p. 37).

[107] S. R. Klein. **IceCube: A Cubic Kilometer Radiation Detector**. *IEEE Transactions on Nuclear Science* 56 (2009), arXiv: `0807.0034` (see pp. 38, 40).

[108] O. Schulz. **The design study of IceCube DeepCore : Characterization and veto studies**. PhD thesis. Max-Planck Institut für Kernphysik, Ruprecht-Karls-Universität Heidelberg, (2010) (see p. 39).

[109] AMANDA Collaboration. **Optical properties of deep glacial ice at the South Pole**. *Journal of Geophysical Research: Atmospheres* 111.D13 (2006) (see pp. 40–42).

[110] J. Lundberg et al. **Light tracking through ice and water - Scattering and absorption in heterogeneous media with PHOTONICS**. *Nuclear Instruments and Methods* (2007), eprint: `astro-ph/0702108` (see pp. 41, 47, 51).

[111] IceCube Collaboration. **Measurement of South Pole ice transparency with the IceCube LED calibration system**. *Nuclear Instruments and Methods* A711 (2013), (see pp. 41, 42).

[112] IceCube Collaboration. **South Pole glacial climate reconstruction from multi-borehole laser particulate stratigraphy**. *Journal of Glaciology* 59.218 (2013), (see p. 42).

[113] P. Askebjer et al. **On the age versus depth and optical clarity of deep ice at South Pole**. *Journal of Glaciology* 41 (1995), arXiv: `astro-ph/9501072 [astro-ph]` (see p. 42).

[114] P. B. Price et al. **Temperature profile for glacial ice at the South Pole: Implications for life in a nearby subglacial lake**. *Proceedings of the National Academy of Sciences* 99.12 (2002), eprint: `http://www.pnas.org/content/99/12/7844.full.pdf+html` (see p. 42).

[115] F. Halzen and S. R. Klein. **Invited Review Article: IceCube: An instrument for neutrino astronomy**. *Review of Scientific Instruments* 81.8 (2010), arXiv: `1007.1247 [astro-ph.HE]` (see p. 43).

[116] F. Halzen. **Astroparticle physics with high energy neutrinos: from amanda to icecube**. *Eur. Phys. J.* C46 (2006), arXiv: `astro-ph/0602132 [astro-ph]` (see p. 44).

[117] J. G. Learned and K. Mannheim. **High-energy neutrino astrophysics**. *Annual Review of Nuclear and Particle Science* 50.1 (2000), (see p. 45).

[118] J. Ahrens et al. **Muon track reconstruction and data selection techniques in AMANDA**. *Nuclear Instruments and Methods* A524 (2004), arXiv: `astro-ph/0407044 [astro-ph]` (see pp. 45, 46).

[119] D. Pandel. **Bestimmung von Wasser- und Detektorparametern und Rekonstruktion von Myonen bis 100 TeV mit dem Bajkal- Neutrinoteleskop NT-72**. MA thesis. Humboldt-Universität zu Berlin, (1996) (see p. 46).

[120] K. Schatto. **IceCube Wiki: Improved likelihood reconstruction**. (2013). URL: `https://wiki.icecube.wisc.edu/index.php/Improved%20likelihood%20reconstruction` (see p. 47).

[121] T. Neunhoffer. **Estimating the angular resolution of tracks in neutrino telescopes based on a likelihood analysis**. *Astroparticle Physics* 25 (2006), arXiv: `astro-ph/0403367 [astro-ph]` (see p. 47).

[122] IceCube Collaboration. **Energy reconstruction methods in the IceCube neutrino telescope**. *Journal of Instrumentation* 9.03 (2014), (see pp. 49, 58, 66, 104).

[123] D. Chirkin and W. Rhode. **Muon Monte Carlo: A High-precision tool for muon propagation through matter**. *arxiv:hep-ph/0407075* (2004). arXiv: `hep-ph/0407075 [hep-ph]` (see pp. 49, 51).

[124] D. C. Juan de Dios Zornoza. **Muon energy reconstruction and atmospheric neutrino spectrum unfolding with the IceCube detector**. *30th International Cosmic Ray Conference.* (2007) (see p. 49).

[125] S. Odrowski. **High-Energy Neutrino Scan of the Galactic Plane**. PhD thesis. Max-Planck-Institut für Kernphysik, Ruprecht-Karls-Universität Heidelberg, (2012) (see p. 49).

[126] D. Chirkin. **Private Communications**. (2014) (see p. 50).

[127] IceCube Collaboration. **An improved method for measuring muon energy using the truncated mean of dE/dx**. *Nuclear Instruments and Methods* A703 (2013), (see p. 50).

[128] A. Gazizov and M. Kowalski. **ANIS: High energy neutrino generator for neutrino telescopes**. *Computer Physics Communications* 172 (2005), eprint: `astro-ph/0406439` (see p. 50).

[129] D. Heck et al. **CORSIKA: a Monte Carlo code to simulate extensive air showers.** FZKA 6019, (1998) (see p. 50).

[130] T. Montaruli. **NeutrinoFlux**. (2009). url: `http://code.icecube.wisc.edu/svn/projects/neutrinoflux/` (see p. 51).

[131] J. R. Hörandel. **On the knee in the energy spectrum of cosmic rays**. *Astroparticle Physics* 19.2 (2003), (see p. 51).

[132] D. Chirkin. **Photon tracking with GPUs in IceCube**. *Nuclear Instrumments and Methods* A725 (2013), (see pp. 51, 104).

[133] IceCube Collaboration. **Extending the Search for Neutrino Point Sources with IceCube above the Horizon**. *Phys. Rev. Lett.* 103.22, 221102 (2009), arXiv: `0911.2338 [astro-ph.HE]` (see p. 51).

[134] F. Halzen and E. Zas. **Neutrino Fluxes from Active Galaxies: A Model-Independent Estimate**. *ApJ* 488.2 (1997), (see pp. 51, 67).

[135] IceCube Collaboration. **Time-integrated Searches for Point-like Sources of Neutrinos with the 40-string IceCube Detector**. *ApJ* 732.1 (2011), (see pp. 53, 105).

[136] S. S. Keerthi et al. **Improvements to Platt's SMO algorithm for SVM classifier design**. *Neural Computation* 13.3 (2001), (see p. 53).

[137] A. Hoecker et al. **TMVA: Toolkit for Multivariate Data Analysis**. *PoS* ACAT (2007), arXiv: `physics/0703039` (see p. 53).

[138] R. Brun and F. Rademakers. **ROOT - An Object Oriented Data Analysis Framework**. *AIHENP'96 Workshop, Lausane.* Vol. 389. 1996, (see p. 53).

[139] IceCube Collaboration. **Searches for Extended and Point-like Neutrino Sources with Four Years of IceCube Data**. *arxiv: 1406.6757* (2014). arXiv: `1406.6757 [astro-ph.HE]` (see pp. 54, 62, 87, 92, 108, 109).

[140] N. Metropolis and S. Ulam. **The monte carlo method**. *Journal of the American statistical association* 44.247 (1949), (see p. 55).

[141] J. Braun et al. **Time-dependent point source search methods in high energy neutrino astronomy**. *Astroparticle Physics* 33 (2010), arXiv: `0912.1572 [astro-ph.IM]` (see p. 57).

[142] P. J. Peebles. **The large-scale structure of the universe**. Princeton University Press, (1980) (see p. 58).

[143] J. N. Fry and P. J. Peebles. **Statistical analysis of catalogs of extragalactic objects. IX - The four-point galaxy correlation function**. *ApJ* 221 (1978), (see p. 58).

[144] P. J. Peebles and E. J. Groth. **Statistical analysis of catalogs of extragalactic objects. V - Three-point correlation function for the galaxy distribution in the Zwicky catalog**. *ApJ* 196 (1975), (see p. 58).

[145] C. B. Finley and S. Westerhoff. **On the evidence for clustering in the arrival directions of AGASA's ultrahigh energy cosmic rays**. *Astroparticle Physics* 21 (2004), arXiv: `astro-ph/0309159 [astro-ph]` (see pp. 58, 65).

[146] R. Abbasi et al. **A Search for arrival direction clustering in the HiRes-I monocular data above 10**19.5 eV**. *Astroparticle Physics* 22 (2004), arXiv: `astro-ph/0404366 [astro-ph]` (see p. 58).

[147] Amanda Collaboration. **Search for point sources of high energy neutrinos with final data from AMANDA-II**. *PRD* 79.6, 062001 (2009), arXiv: `0809.1646` (see p. 58).

[148] K. Abraham. **Neutrinos on Graphics Cards**. (2014) (see pp. 59, 60).

[149] Y. Sestayo and E. Resconi. **Uncovering neutrinos from cosmic ray factories: the Multi Point Source method**. *Astroparticle Physics* 44 (2013), arXiv: `1301.1529 [astro-ph]` (see pp. 60, 83).

[150] IceCube Collaboration. **Searches for High-energy Neutrino Emission in the Galaxy with the Combined ICECUBE-AMANDA Detector**. *ApJ* 763.1 (2013), (see pp. 60, 83).

[151] IceCube Collaboration. **The IceCube Neutrino Observatory Part I: Point Source Searches**. *ArXiv e-prints* (2013). arXiv: `1309.6979 [astro-ph.HE]` (see pp. 60, 83).

[152] J. Hammersley and D. Handscomb. **Monte Carlo Methods**. Methuen's monographs on applied probability and statistics. Methuen, (1964) (see p. 68).

[153] D. A. Green. **A revised Galactic supernova remnant catalogue**. *Bulletin of the Astronomical Society of India* 37 (2009), arXiv: `0905.3699 [astro-ph.HE]` (see p. 69).

[154] J. Neyman. **Outline of a Theory of Statistical Estimation Based on the Classical Theory of Probability**. *Phil. Trans. Royal Soc. London* A 236 (1937), (see pp. 72, 88).

[155] J. F. Beacom and M. D. Kistler. **Dissecting the Cygnus region with TeV gamma rays and neutrinos**. *Phys. Rev. D* 75 (8 2007), (see p. 84).

[156] Y. Sestayo. **Search for high energy neutrinos from our Galaxy with IceCube**. PhD thesis. Max-Planck-Institut fur Kernphysik, Heidelberg, (2010) (see p. 88).

[157] S. Casanova. **Private Communication**. (2014) (see p. 89).

[158] IceCube Collaboration. **Long Term Search for Flaring Neutrino Sources with the IceCube Detector**. *ApJ* in preparation (2014) (see p. 98).

[159] M. Leuermann. **Search for Diffuse Neutrino Point Sources Using a Multipole Analysis in IceCube**. MA thesis. RWTH Aachen, (2013) (see p. 107).

[160] A. Abdo et al. **The Large Scale Cosmic-Ray Anisotropy as Observed with Milagro**. *ApJ* 698 (2009), arXiv: `0806.2293 [astro-ph]` (see pp. 107, 108).

[161] W. Kraushaar et al. **Explorer XI Experiment on Cosmic Gamma Rays.** *ApJ* 141 (1965), (see p. 112).

List of Figures

List of Tables

Acknowledgements

This work would not have been possible without the help and support from other people and I am thankful to all of them.

First of all, I would like to thank my supervisor Elisa Resconi, who gave me the opportunity to work on such an interesting topic in joining IceCube. She always has an open door and words of motivation together with an inspiring enthusiasm for every new idea.

I would also like to thank Prof. Lothar Oberauer for being my second reviewer.

Another big thank you goes to Elisa's group, which was in always changing configurations a big source of knowledge and support in all different ways:

Sirin Odrowski for the help with the 2-pt and the MPS searches, which would not have been possible without her former work and her assistance and some encouraging words from wherever she was located at that time,

Andreas Gross for his profound knowledge and his opinion on almost everything in IceCube and the contributions to the self-triggered flare search,

Yolanda Sestayo for the discussions about the Cygnus region and their limit calculations and bringing in the astrophysical spirit,

Stefan Coenders for teaming up in the football office and his help with every stupid bug I produced,

and also Martin Jurkovic, Kai Krings and Kevin Abraham, who assisted at some point of this work.

Inside the IceCube Collaboration a lot of people commented and contributed to this work and I would like to thank especially Chad Finley and Martin Leuermann for the help and input on the paper.

Sabrina Casanova I want to thank for some useful discussions and calculations on the diffuse limit of the Cygnus region.

I would also like to thank the TUM Graduate School for their financial support in attending the ICRC 2013.

My parents I thank for always supporting me.

And finally, I want to thank Claudius for always finding a way to cheer me up and just for being there.